Numerical investigation of rotating and stratified turbulence

by

Enrico Deusebio

June 2012
Technical Reports
Royal Institute of Technology
Department of Mechanics
SE-100 44 Stockholm, Sweden

Akademisk avhandling som med tillstånd av Kungliga Tekniska Högskolan i Stockholm framlägges till offentlig granskning för avläggande av teknologie licentiatsexamen fredag den 15 juni 2012 kl 10.00 i sal Seminarsrummet, Kungliga Tekniska Högskolan, Brinellvägen 32, Stockholm.

Universitetsservice US–AB, Stockholm 2012

Numerical investigation of rotating and stratified turbulence

Enrico Deusebio
Linné Flow Centre, KTH Mechanics, Royal Institute of Technology
SE-100 44 Stockholm, Sweden

Abstract

Atmospheric and oceanic flows are strongly affected by rotation and stratification. Rotation is exerted through Coriolis forces which mainly act in horizontal planes whereas stratification largely affects the motion along the vertical direction through buoyancy forces, the latters related to the vertical variation of the fluid density. Aiming at a better understanding of atmospheric and oceanic processes, in this thesis the properties of turbulence in rotating and stably stratified flows are studied by means of numerical simulations, with and without the presence of solid walls.

A new code is developed in order to carry out high-resolution numerical simulations of geostrophic turbulence forced at large scales. The code was heavily parallelized with MPI (Message Passing Interface) in order to be run on massively parallel computers. The main problem which has been investigated is how the turbulent cascade is affected by the presence of strong but finite rotation and stratification. As opposed to the early theories in the field of geostrophic turbulence, we show that there is a forward energy cascade which is initiated at large scales. The contribution of this process to the general dynamic is secondary at large scales but becomes dominant at smaller scales where leads to a shallowing of the energy spectrum. Despite the idealized set-up of the simulations, two-point statistics show remarkable agreement with measurements in the atmosphere, suggesting that this process may be an important mechanism for energy transfer in the atmosphere.

The effect of stratification in wall-bounded turbulence is investigated by means of direct numerical simulations of open-channel flows. An existing full-channel code was modified in order to optimize the grid in the vertical direction and avoid the clustering of grid points at the upper boundary, where the solid wall is replaced by a free-shear condition. The stable stratification which results from a cooling applied at the solid wall largely affects the outer structures of the boundary layer, whereas the near-wall structures appear to be mostly unchanged. The effect of gravity waves is also studied, and a new decomposition is introduced in order to separate the gravity wave field from the turbulent field.

Descriptors: Geostrophic turbulence, stable stratification, rotation, wall-bounded turbulence, gravity waves, atmospherical dynamics, direct numerical simulations

Preface

This thesis deals with the numerical investigation of the property of stratified and rotating turbulence, both with and without the presence of walls. A brief introduction on the basic concepts and methods is presented in the first part. The second part contains three articles and one internal report. The papers are adjusted to comply with the present thesis format for consistency, but their contents have not been altered as compared with their original counterparts.

Paper 1. A. Vallgren, E. Deusebio & E. Lindborg, 2011
Possible Explanation of the Atmospheric Kinetic and Potential Energy Spectra. *Physical Review Letters, 107:26, 268501.*

Paper 2. E. Deusebio, A. Vallgren & E. Lindborg, 2012
The route to dissipation in strongly stratified and rotating flows. *Submitted - Journal of Fluid Mechanics*

Paper 3. E. Deusebio, P. Schlatter, G. Brethouwer & E. Lindborg, 2011
Direct numerical simulations of stratified open channel flows *J. Phys., Conf. Ser., 318, 022009.*

Paper 4. E. Deusebio, 2010
The open-channel version of SIMSON *Internal Report*

Division of work among authors

The main advisor for the project is Dr. Erik Lindborg (EL). Dr. Philipp Schlatter (PS) and Dr. Geert Brethouwer (GB) have acted as co-advisor.

Paper 1

The code was developed and implemented by Andreas Vallgren (AV) and Enrico Deusebio (ED). The numerical simulations were performed by AV. The paper was written by EL, with the help of AV and ED. ED was particularly active during the review process.

Paper 2

The solver code was developed and implemented by ED in collaboration with AV. The numerical simulations were performed by ED. The post-processing code for studying the triad interactions was developed by ED. The paper was written by ED, with the help of EL. AV provided comments on the article.

Paper 3

The modification of the existing code SIMSON was performed by ED, with the help of PS and GB. The simulations and the analysis of the results were done by ED, with the input of PS, GB and EL. The paper was written by ED, with feedback by EL, GB and PS.

Paper 4

The idea underlying the new discretization was suggested by EL. The implementation, code-optimization and validation were done by ED, under supervision of PS, GB and EL. The report was written by ED.

Part I

Introduction

CHAPTER 1

Turbulence and numerical simulations

"Observe the motion of the surface of the water which resembles that of hair, and has two motions, of which one goes on with the flow of the surface, the other forms the lines of the eddies; thus the water forms eddying whirlpools one part of which are due to the impetus of the principal current and the other to the incidental motion and return flow[1]." It was between the XV and the XVI century that the first attempt of a scientific study of turbulent motions was done by the Italian Leonardo da Vinci. More than five hundred years later, turbulence is still an object of vivid and active research. A subject yet not understood and in certain aspects mysterious. Richard Feynman describes turbulence as one of the most important unsolved problem of classical physics (Feynman 1964). The note left by Leonardo da Vinci already contains a description of some important characteristic features of turbulence: the presence of eddies and swirling motions which, in a rather chaotic manner, superimpose on the main motion of the fluid. It was the same observation which led Reynolds (1895), almost four hundred years later, to describe turbulent motions statistically by decomposing the velocity field into a mean and a fluctuating part. Indeed, the perhaps most important insight into the essentials of turbulence goes back to less than a hundred years ago, with the observations of Richardson (1922)

> Big whirls have little whirls
> that feed on their velocity,
> and little whirls have lesser whirls
> and so on to viscosity

Far from being trivial, Richardson's observation constitutes the ground on which all the following theories were based (*e.g.* Kolmogorov 1941*b*). Large eddies break down into smaller eddies in an inviscid process which continues until energy is converted into heat at the very smallest scales of motions where viscosity dominates. Thus, turbulent flows possess many scales, both in space and in time. Indeed, turbulent flows own their intrinsic complexity to the interplay among these scales.

From an historical perspective, most of the advances in the understanding of turbulent processes were made in the past 150 years, since the pioneer work

[1]see Richter, J. P. 1970. Plate 20 and Note 389. In The Notebooks of Leonardo Da Vinci. New York: Dover Publications.

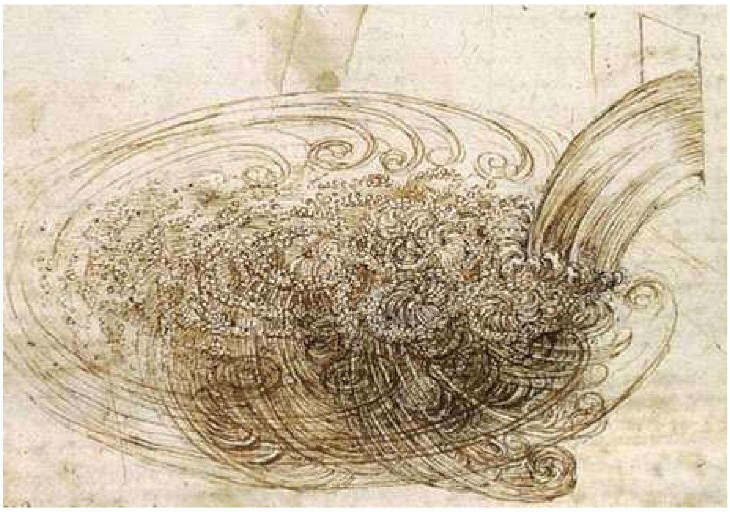

FIGURE 1.1. da Vinci sketch of a turbulent flow

of Reynolds. Besides the experimental investigations, a substantial amount of work has also been dedicated to theoretical investigations of turbulence. Several approaches were proposed and undertaken. Strongly influenced by the view of turbulent motions as chaotic and unpredictable, the early studies mainly aimed at a statistical characterization of the dynamics.

Perhaps the most important contribution to a quantitative statistical description of turbulent flows is the theory proposed by Kolmogorov (1941*b*). As eddies break down into smaller eddies, they lose any preferable orientation and the anisotropy of the large scales of the flow is progressively lost. Kolmogorov (1941*b*) suggested that statistical quantities in the cascade do not depend neither on the direction nor on spatial coordinates, but they attain an universal form which depends only on the energy flux, ε, through the cascade and, at small scales, on the viscosity ν. Despite its simplicity, Kolmogorov (1941*b*) theory has been able to make quantitatively accurate predictions.

The apparent chaotic and unpredictable nature of turbulent flows seems to be in contrast with the deterministic nature of the Navier-Stokes equations which govern the fluid motions. Besides the *statistical* approach, other approaches have also been proposed, postulating the presence of more organized patterns. The *structural* approach aims at identifying coherent structures which cyclically appears in the flow and sustain the turbulent motions. The *deterministic* approach, on the other hand, views a turbulent process as a nonlinear dynamic system which exhibits a high dependence on initial conditions and apparently chaotic solutions which, however, project onto particular objects in phase-space, called “strange attractors”.

In the last fifty years turbulence research has benefited from the powerful tool of digital computers, which complementary to experiments, can be used to study turbulence in detail. This thesis shows how such an approach could effectively be employed in order to shed light on turbulent dynamics. As opposed to experiments, numerical simulations allow us to obtain full information of the flow fields and to perfectly control the external conditions (*e.g.* boundary conditions). Moreover, they also allow us to study idealized and "non-physical" setups where different factors/phenomena influencing the turbulent dynamics can be separated.

The first attempt to a direct flow computation was made in the beginning of the XX century by Richardson (1922), who undertook the first historical weather forecast ever done. The measured atmospheric data were advanced in time by using a rather simple mathematical model able to capture the main features of the atmosphere, predicting the flow evolution in the next six hours. All the computations were done by hand. Unfortunately, because some smoothing techniques were not applied on the original data, Richardson's forecast failed dramatically. Nevertheless, it represents a mile-stone in the soon-to-appear era of numerical simulations.

It is only from the beginning of the 1960 that the technology of the digital computers were sufficiently developed to allow for the first numerical computations. Lorenz (1963), in his pioneer work, studied a simple version of the Navier-Stokes equations, based on machine computations. The system studied by Lorenz (1963) was nonlinear and deterministic, as the Navier-Stokes. Moreover, it also shares some common feature with turbulent motions, such as high sensitivity to initial conditions and chaotic solutions. The work of Lorenz resolved the apparent paradox that deterministic systems can behave chaotically, delineating the beginning of the modern view of turbulence as "deterministic chaos".

From a numerical perspective, the most challenging aspect of turbulence is its intrinsic feature of containing a large range of scales that interact with each other. If one aims at correctly simulating turbulent flows, all the scales, from the large energy-containing scales to the very smallest scales, must be represented, posing severe requirements on the computational demands. In the atmosphere, for instance, the largest scales at which energy is injected are of the order of thousand kilometres. On the other hand, viscosity acts only at centimetre scales. To represent such a vast span of scales in a simulation is, of course, impossible. Also numerical computations of turbulent flows in engineering applications, *e.g.* flows around airplanes or cars, are nowadays out of reach. The largest scale of turbulence is often referred to as the integral lengthscale L, whereas the smallest scale is the Kolmogorov scale, defined as $\eta = \nu^{3/4}/\varepsilon^{1/4}$. The Kolmogorov scale is usually interpreted as the scale at which viscosity acts and dissipates the downscale cascading energy. One fundamental parameter in fluid dynamic applications is the Reynolds number, $Re = UL/\nu$, which quantifies the relative importance between inertial and viscous forces.

Here, U is a characteristic large scale velocity. The ratio between the largest scale, L, and the smallest viscosity affected scale, η, can be related to the Reynolds number as $L/\eta \sim Re^{3/4}$. Values of Re in engineering applications are typically of the order of 10^6, making the computation of turbulent flows out of reach at the present point.

The first pioneer direct numerical simulations of a homogeneous and isotropic turbulent flow dates back to the beginning of the 70s, with the work of Orszag & Patterson (1972). The scale separation simulated was indeed very limited, with 64^3 grid points, very far from being of practical interest for real applications. The available computational resources at that time were not able to meet the large Reynolds number of practical interest and, therefore, the early attempts to numerically describe turbulent flows were deeply connected with the development of mathematical models of turbulent motions.

The idea of replacing the exact Navier-Stokes equations with its filtered/averaged counterparts goes back to the decomposition of Reynolds (1895). The filtered scale-independent Reynolds Averaged Navier-Stokes (RANS) equations, still exact, contain terms which are not closed and therefore need to be modelled, that is to say, a model for the turbulent fluctuations must be constructed. The first attempt to model turbulence was proposed by Boussinesq (1877), who suggested an analogy between turbulent motions and the Brownian motion of gas molecules. Similarly, he postulated that the effect of turbulent motions in the flow can be modelled by a fictitious eddy-viscosity. Despite its simplicity and its limitations, the general idea of Boussinesq is still widely used in many current turbulent models.

Starting from the 70s, the development of computational powers also led to an increased interest in new more accurate models, with the aim of bridging the gap between available computational resources and engineering applications. Beside the efforts on improving the models of RANS, new approaches, such as Large-Eddy Simulations (LES), were proposed (Smagorinsky 1963; Deardorff 1970). The underlying idea of these new approaches was to resolve the turbulent scales to a certain extent and model the remaining part, the so called sub-grid scales. As pointed out by Reynolds (1990), before the 90s computational power had not increased enough to make even LES feasible, and only RANS were used in engineering practical applications. However, since LES became feasible, it has been the subject of an increasing amount of studies and represents the perhaps most promising technique of modelling turbulent flows. Recent developments in the field of the LES includes the dynamic procedure proposed by Germano (1992) and Germano *et al.* (1991), varius forms of "synthetic-velocity" (Domaradzki & Saiki 1997), approximate deconvolution models (Stolz & Adams 1999) and explicit algebraic models (Gatski & Speziale 1993; Rasam *et al.* 2011).

In the 90s, computational resources had indeed reached a maturity which made DNS at reasonably high Reynolds numbers possible. Besides the study of homogeneous isotropic turbulence at high Reynolds numbers, turbulent flows in the presence of solid walls were also investigated. The first DNS of a fully turbulent channel flow was performed by Kim *et al.* (1987). Interestingly, such a study was shortly preceded by a DNS of the curved channel by Moser & Moin (1987). The turbulent flat-plate boundary layer was first investigated by Spalart (1988). The following years were extremely intense and a large number of studies were produced. The complexity of the flows gradually increased by considering compressible, even reacting, flows and several non-trivial geometries. The evolution of the geometries also led to the development of new numerical methods able to deal with curved and irregular walls.

Nevertheless, as noted by Moin & Mahesh (1998), Reynolds numbers at that time were still rather low. The development of massively parallel machines over the last decade has made it feasible to increase the Reynolds number by almost one order of magnitude. In the field of isotropic and homogeneous turbulence, DNS at resolutions of 4096^3 were performed by Kaneda *et al.* (2003). In the field of wall-bounded flows, channel flows at a friction Reynolds number[2] $Re_\tau = 2000$ were performed by Hoyas & Jiménez (2006), whereas its turbulent boundary layer counterparts were studied by Schlatter *et al.* (2009) at a Re_θ, defined with the momentum thickness[3] θ in place of L, of $Re_\theta = 2500$ and Sillero *et al.* (2010) at $Re_\theta = 6000$. Nowadays, the Reynolds number that can be reached in numerical simulations and in experiments are comparable, allowing for a comparison and a complementary analysis (Schlatter & Örlü 2010; Segalini *et al.* 2011). More importantly, the increase of the Reynolds number allows us to gain important insights in the turbulent dynamics, revealing important features, such as intermittency (Benzi *et al.* 1993; Frisch 1996; Biferale & Toschi 2001), the presence of coherent structures (Del Álamo *et al.* 2006) and interactions among the different scales of the flow (Hoyas & Jiménez 2006).

In the spirit of the discussion above, in this thesis we aim at studying the turbulent dynamics in the presence of rotation and stratification by means of high-resolution numerical simulations. Such conditions are very important, especially in a geophysical perspective. A thorough understanding of turbulent processes should mainly focus on how energy is exchanged among the different scales. This is important both from a scientific and a practical point of view. Critical evaluations as well as related improvements of large-scale atmospheric models cannot be achieved unless the physics and the main mechanisms of the atmospheric dynamics are understood. In chapter 2, a short survey of the background on turbulence strongly affected by rotation and stratification is given. Chapter 3 offers a short overview on wall-bounded turbulence and on the effect of a stable stratification. In chapter 4, the papers are presented. Finally, chapter 5 concludes with some general remarks and outlook.

[2]defined as $Re_\tau = u_\tau L/\nu$. $u_\tau = \sqrt{\tau_w/\rho}$ is the friction velocity with τ_w being the shear stress at the wall.

[3]defined as $\int_0^\infty \left(1 - \frac{u}{U_\infty}\right) \frac{u}{U_\infty}\, \mathrm{d}y$.

CHAPTER 2

Rotating and stratified turbulence: a geophysical perspective

Atmospheric and oceanic flows are highly affected by both rotation and stratification. Rotation is exerted through Coriolis forces which mainly act in horizontal planes whereas stratification largely affects the motion along the vertical direction through the Archimede's force. Depending on the mean density profile, stratification can either enhance or suppress vertical motions. Stratification in the atmosphere is usually stable above the boundary layer (Vallis 2006; Gill 1982), *i.e.* a fluid particle which is displaced in the vertical direction tends to return to its initial position.

Whereas highly rotating flows tend to form structures which are elongated in the vertical direction (Taylor 1923), highly stratified flows favour thin structures elongated in the horizontal direction. Such structures are usually referred to as pancake structures (Lindborg 2006; Brethouwer *et al.* 2007). It is the interplay between these two regimes that gives rise to the variety of dynamics seen in the atmosphere.

In the most general case, the governing equations for the flows in the atmosphere and in the oceans are the compressible Navier-Stokes equations. Fluid density may change from place to place, affected by other scalar quantities such as pressure, temperature, humidity and salinity. Nevertheless, great insight into the turbulent dynamics can be gained by reducing the complexity of the problem by making a few assumptions. Following the standard derivation, we restrict ourself to the incompressible Navier-Stokes equations under the Boussinesq approximation on a f-plane. These can be written as

$$\frac{D\mathbf{u}}{Dt} = -\frac{\nabla p}{\rho_0} - f\mathbf{e}_z \times \mathbf{u} + Nb\mathbf{e}_z, \tag{2.1a}$$

$$\frac{Db}{Dt} = -Nw, \tag{2.1b}$$

$$\nabla \cdot \mathbf{u} = 0\,, \tag{2.1c}$$

where $\mathbf{u}$ is the velocity vector, $f = 2\Omega$ is the Coriolis parameter with Ω being the rotation rate in the f-plane, $\mathbf{e}_z$ is the vertical unit vector and p is the pressure. $N = \sqrt{g/T_0 dT/dz}$ refers to the Brunt-Väisälä frequency, with being g the gravity acceleration, T_0 a reference temperature and dT/dz its vertical gradient. $b = g\rho/(N\rho_0)$ is the rescaled buoyancy, where ρ and ρ_0 are the fluctuating and background densities, respectively. With such a definition, b has the unit of measure of a velocity. D/Dt represents the material derivative. In (2.1) we have omitted diffusion terms which act only at very small scales. In the following sections, we simplify this system for the different atmospheric and oceanic regimes, shortly reviewing the main theories and the main open questions concerning turbulence in geophysical flows.

2.1. Geostrophic turbulence

Atmospheric and oceanic dynamics are forced at very large scales. In the atmosphere, the available potential energy related to the polewards temperature gradient is converted to kinetic energy by baroclinic instability which develops on scales of the order of thousand kilometres. The general circulation of the oceans is mainly driven by surface fluxes of momentum which also attain similar spatial scales. At such large scales, Earth rotation strongly affects the flow. Moreover, the stratification is generally quite strong, both in the atmosphere and in the oceans (Pedlosky 1987; Vallis 2006).

The relative importance of Coriolis forces and buoyancy forces compared to inertial forces are often quantified by the Rossby and the Froude numbers, defined as

$$Ro = \frac{U}{fL} \qquad \text{and} \qquad Fr = \frac{U}{NL}. \tag{2.2}$$

Here, L is a characteristic horizontal scale and U a characteristic velocity. These parameters are indeed small in large-scale geophysical applications. For instance, in the atmosphere, reasonable values of Ro and Fr are of the order of 0.1, for Ro, and 0.001, for Fr (Deusebio *et al.* 2012). Thus, in equations (2.1) the horizontal pressure gradient is mainly balanced by Coriolis forces (*geostrophic balance*), whereas the vertical pressure gradient is mainly balanced by buoyancy forces (*hydrostatic balance*).

For strong rotation rates, an asymptotic analysis in Ro as a small parameter is possible. For the details of such a derivation, we refer the reader to any geophysical fluid dynamic textbook, such as Vallis (2006) or Pedlosky (1987). At zero order, a horizontal divergence-free flow $\mathbf{u}_0$ which perfectly satisfies geostrophic balance is recovered. At first order in Ro, the material conservation of the Charney potential vorticity q_0 (Charney 1971),

$$q_0 = -\frac{\partial u_0}{\partial y} + \frac{\partial v_0}{\partial x} + \frac{f}{N}\frac{\partial b_0}{\partial z}, \tag{2.3}$$

is satisfied, *i.e.*

$$\frac{Dq_0}{Dt} = 0, \tag{2.4}$$

where the material derivative retains only the horizontal advection contributions. In the following the subscript "0" will be dropped, for simplicity. Assuming hydrostatic balance and rescaling the vertical coordinates with f/N,

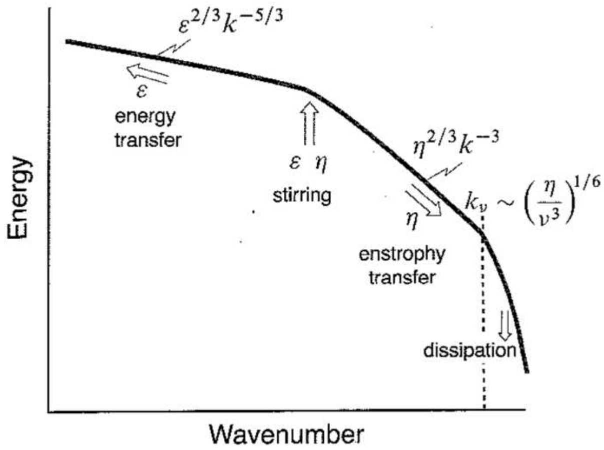

FIGURE 2.1. Sketch of the energy spectrum in two-dimensional and in QG turbulence (figure taken from Vallis 2006).

it is possible to rewrite q in terms of the stream function[1] ψ as $q = \nabla^2\psi$. In literature, equation (2.4) is often referred to as the quasi-geostrophic (QG) equation. The zero order expansion also conserves energy, that is

$$\frac{D}{Dt}\frac{u^2+v^2+b^2}{2} = -\frac{\partial}{\partial x}pu - \frac{\partial}{\partial y}pv - \frac{\partial}{\partial z}pw\,, \tag{2.5}$$

if appropriate boundary conditions are chosen. Therefore, the QG equation conserves independently two quadratic invariants, energy and potential enstrophy, where the latter is defined as half of the square of potential vorticity, $q^2/2$.

Moreover, the spectral counterparts of these two quantities, energy and enstrophy, are related by

$$E(\mathbf{k}) = k^2 \cdot Z(\mathbf{k}). \tag{2.6}$$

Here, k is the modulus of the three dimensional wave-vector $\mathbf{k}$, whereas $E(\mathbf{k})$ and $Z(\mathbf{k})$ are the energy and enstrophy content in mode $\mathbf{k}$, respectively. This distinctive property of the QG equation, also shared with strictly two-dimensional flows, is indeed the basis of its most interesting feature: the presence of an inverse cascade of energy. As shown in a visionary paper of Kraichnan (1967), the presence of two related quadratic invariants in two-dimensional flows leads to a global energy transfer towards large scales, as opposed to three-dimensional flows. Enstrophy, on the other hand, is transferred towards small scales in a forward cascade.

[1]being the zero order divergence free, the stream function $\mathbf{u}_h = \nabla \times \psi\mathbf{e}_z$ completely define the horizontal velocity.

As shown in fig. 2.1, if energy and enstrophy are injected at a scale k_f, energy cascades up-scale in the *energy inertial range* whereas enstrophy is transferred downscale in the *enstrophy inertial range*. Following similar arguments as Kolmogorov (1941*b*), Kraichnan (1967) argued that inertial range statistics at a particular scale $l = 2\pi/k$ are universal and do not depend on the viscosity ν. In the energy inertial range they only depend on the energy injection rate, which is equal to the up-scale flux of energy, ε. Simple dimensional considerations suggests a scaling for the energy spectrum as

$$E(k) = \mathcal{K}\varepsilon^{2/3}k^{-5/3}. \tag{2.7}$$

Note that such an expression is similar to the one derived by Kolmogorov (1941*b*). In a similar way, assuming that the statistics in the enstrophy range have a universal form which only depends on the enstrophy small-scale dissipation leads to an energy spectrum of the form

$$E(k) = \mathcal{C}\eta^{2/3}k^{-3}. \tag{2.8}$$

The dimensionless constants, $\mathcal{K}$ and $\mathcal{C}$, are assumed to be universal and are often referred as Kraichnan and Kraichnan-Batchelor constant, respectively. The theory of Kraichnan (1967) has been tested numerically in a number of studies. Early investigations (Legras *et al.* 1988; Ohkitani 1990; Maltrud & Vallis 1993; Ohkitani & Kida 1992) indicated a steeper energy spectrum in the enstrophy range as compared to Kraichnan's prediction. However, as computational resourses allowed larger resolutions, (2.7) was recovered (Boffetta 2007; Vallgren & Lindborg 2011). As for the energy inertial range, recent high-resolution numerical simulations have confirmed the existence of an inverse energy cascade, even though a somewhat steeper spectrum than (2.8) has been obtained by some investigators. This steeper spectrum is likely to be a result of formation of large scale coherent vortices (Scott 2007; Vallgren 2011).

Can QG dynamics alone explain the large scale atmospheric and oceanic dynamics? Indeed, the inverse energy cascade of strongly rotating flows leaves an empty gap on how energy can be dissipated in rotating systems such as the Earth. Dissipation of kinetic and potential energy can only be achieved by means of molecular viscosity and diffusion which act at very small scales. In the atmosphere, for instance, these scales can be estimated to be of the order of few centimetres or even millimetres. How to reconcile the picture of a large-scale inverse energy cascade dynamics with the presence of small scale dissipation is a problem that has become increasingly important as the resolution of numerical models has increased. Since QG dynamics is not able to support a forward energy cascade, non-balanced motions must be taken into account. How energy can be transferred from balanced quasi-geostrophic motions to ageostrophic motions is a fundamental question that, in the following, we attempt to answer by means of high-resolution numerical simulations.

2.2. Stratified turbulence

As the flow scales decrease, the effects of rotation and stratification are reduced. In the atmosphere rotation becomes of secondary importance at scales of the order of tens of kilometres. However, at such scales stratification is still very important and typical Froude numbers are very small.

In the last decade there has been important advances in understanding of turbulence in the presence of strong stratification. Thanks to novel numerical experiments it has been possible to resolve the issue regarding the direction of the energy cascade in the strongly stratified regime. In the early works it was suggested that strong stratification favours an inverse energy cascade. By rescaling the equations of motions as done by Riley *et al.* (1981), Lilly (1983) argued that strong stratification leads to the suppression of vertical motions and a two-dimensionalisation of the flow. In this limit, an inverse cascade would therefore be achieved, as predicted by Kraichnan (1967). Lilly (1983) suggested that in the atmosphere energy in decaying three-dimensional convective turbulent patches would, by effect of the stable stratification, be transferred up-scale and feed the growth of two-dimensional structures.

Despite the appeal of such a theory, the advances in the understanding of strongly stratified turbulence in the last decade have proved Lilly's view to be wrong. In the limit of zero Fr, Billant & Chomaz (2001) showed that the Navier-Stokes equations allow for self-similar solutions with a vertical lengthscale $l_z \sim U/N$, proposing an alternative scaling of the equations than the one used by Lilly (1983) and Riley *et al.* (1981). Introducing different vertical and horizontal lengthscales, l_z and l_h respectively, we find from the hydrostatic condition an estimate for $b \sim U^2/Nl_z$ and from (2.1b) an estimate for $w \sim bU/Nl_h \sim Ul_hFr^2/l_z$. Thus, the following scalings for the convective terms hold

$$u\frac{\partial}{\partial x} \sim \frac{U}{l_h}, \qquad w\frac{\partial}{\partial z} \sim Fr^2\frac{U\,l_h}{l_z^2} \sim \frac{U}{l_h}\frac{Fr^2}{\delta^2}, \tag{2.9}$$

where $\delta = l_z/l_h$. Thus, if the estimate of Billant & Chomaz (2001) is used for l_z, it follows that $Fr \sim \delta$ and the vertical component of the convective term is of leading order and cannot be neglected as done in the analysis of Lilly (1983) and Riley *et al.* (1981). Billant & Chomaz (2001) introduced two different Froude numbers in their analysis, F_h and F_v, based on the horizontal and vertical lengthscales. Whereas F_h is a small quantity in strongly stratified flows, F_v stays on the order of unity.

Thus, a stratified system retains its intrinsic three-dimensionality and never approaches the two-dimensional manifold. Moreover, Billant & Chomaz (2000) showed that in stratified flows two-dimensional solutions are unstable with respect to a new type of instability, called zig-zag instability (Billant & Chomaz 2000), and therefore tend to become three-dimensional. The theoretical findings of Billant & Chomaz (2001) have recently been confirmed in a number of numerical studies (Riley & deBruynKops 2003; Lindborg 2006; Waite & Bartello 2006; Brethouwer *et al.* 2007). Riley & deBruynKops (2003) studied the decaying of Taylor-Green vortices numerically in strongly stratified mediums. The authors found that the suppression of vertical motions induced by the stable stratification provides a decoupling of layers, leading to large vertical gradients. Consequently, F_v increases and becomes of the order of unity, allowing for Kelvin-Helmotz instabilities (KH) to develop. Indeed, KH provides a physical mechanism which allows for a transfer of energy downscale. Also box simulations of forced strongly stratified turbulence have confirmed that stratification favors a direct cascade (Lindborg 2006; Waite & Bartello 2006; Brethouwer *et al.* 2007). In agreement with the prediction of Lindborg (2006), the two-dimensional horizontal kinetic and potential energy spectra in the inertial range are found to scale as

$$E_K(k_h) = C_1 \varepsilon_K^{2/3} k_h^{-5/3}, \qquad E_P(k_h) = C_2 \varepsilon_P k_h^{-5/3} / \varepsilon_K^{1/3}, \tag{2.10}$$

where ε_K and ε_P represent the kinetic and potential small-scales energy dissipation. C_1 and C_2 are found to be of the order of unity and have similar values, *i.e.* $C_1 \approx C_2 = 0.51 \pm 0.02$ (Lindborg 2006). Using dimensional arguments, Billant & Chomaz (2001) suggested a scaling for the vertical energy spectrum

$$E(k_z) = C\, N^3\, k_z^{-3}, \tag{2.11}$$

with the dimensionless constant C being of the order of unity. As noted by Brethouwer *et al.* (2007), numerical and also experimental investigations of stratified turbulence are very demanding in terms of Reynolds numbers. Attempts to recover the vertical energy spectrum have more or less failed, possibly due to the insufficient scale separations. In the inertial range of the turbulent cascade, the effect of viscosity is supposedly negligible. However, at moderate Reynolds numbers, the constraint on the vertical lengthscale due to stratification leads to severe limitations. The viscous term related to the second order vertical derivative can be estimated as

$$\nu \frac{\partial^2}{\partial z^2} u_i \sim \nu \frac{U}{l_z^2} \sim \nu \frac{U^2}{l_h} \frac{Re}{\delta} = \frac{U^2}{l_h} \frac{1}{Re\, Fr^2}\,, \tag{2.12}$$

which shows that the effective Reynolds number in stratified flows is reduced by a factor Fr^2. Thus, even though Re is large, viscosity may nevertheless affect the dynamics if stratification is very strong.

2.3. Three dimensional turbulence

As the scales of the flow reduce even further, also stratification becomes of less importance and classical three-dimensional Kolmogorov turbulence is recovered. The transition between these two regimes is usually assumed to be the so-called Ozmidov lengthscale, defined as (Ozmidov 1965)

$$l_O = \frac{\varepsilon^{1/2}}{N^{3/2}}, \tag{2.13}$$

where ε is the energy flux towards small scales. The Ozmidov lengthscale is usually interpreted as the largest scale at which overturning motions are possible. Using the estimates of Billant & Chomaz (2001) and the estimate

$l_h \sim u^3/\varepsilon$ (Lindborg 2006), the following scaling can be found

$$\frac{l_h}{l_O} \sim Fr^{-3/2} \qquad \text{and} \qquad \frac{l_z}{l_O} \sim Fr^{-1/2}. \tag{2.14}$$

The Ozmidoz lengthscale in the oceans has been estimated to be of the order of metres (Gargett *et al.* 1981), whereas in the atmosphere, typical values may range between one metre, in strongly stratified atmospheric boundary layers (Frehlich *et al.* 2008), and ten metres, in the upper troposphere (Lindborg 2006). At smaller scales, classical three dimensional turbulence develops and the Kolmogorov (1941*b*) theory is valid. Vertical and horizontal energy spectra scale as

$$E(k) = C\varepsilon^{2/3}k^{-5/3} \tag{2.15}$$

with a direct energy cascade from large to small scales. The Kolmogorov constant C is of the order of unity. Viscosity becomes important only at scales of the order of centimetres or even millimetres, where dissipation takes place.

2.4. Towards the atmosphere...

Even though the separate turbulent regimes (three-dimensional, stratified and geophysical turbulence) have been widely studied in the last decade, investigations of the transition from one dynamics to another are rather scarce. Indeed, within the context of numerical simulations, the available computational resources impose severe constraints on the scale separations, and simulating more than one regime has not been possible until very recently.

In order to shed light onto atmospheric and oceanic dynamics, such investigations are fundamental and crucial. One issue which is still an object of a vivid debate is the so-called *Nastom-Gage spectrum*. By using sensors mounted in commercial aircrafts, Nastrom *et al.* (1984) were able to measure the kinetic and potential energy spectra in the atmosphere from scales of the order of few kilometres up to scales of the order of thousand kilometres. The striking outcome of their work was the observation that the atmospheric energy spectrum clearly divides into two separate regimes (see fig. 2.2): at synoptic scales ($\sim$ 1000 km) a spectrum of the form $\sim k^{-3}$ is found, whereas at mesoscales ($\sim$ 100 km) much shallower spectra are observed, $\sim k^{-5/3}$, with a smooth transition around 500 km. More than twenty years later, it is still debated which dynamics are producing these spectra.

While the k^{-3} range can be described by a quasi-geostrophic turbulent dynamics, the $k^{-5/3}$ range is more mysterious and intriguing. In particular, such a spectrum may arise from both stratified and geostrophic turbulence. However, the underlying dynamics is completely different with a direct cascade of energy in the former case and an inverse cascade of energy in the latter case. Early studies, *e.g.* Lilly (1983), interpreted the $k^{-5/3}$ range as a stratified inverse energy cascade. Nevertheless, the recent progress in stratified turbulence rather suggests that the $k^{-5/3}$ range is a result of a direct energy cascade. In spite of this, Lilly's interpretation have recently been revived by some experiments in electromagnetically forced thick layers, suggesting that the presence

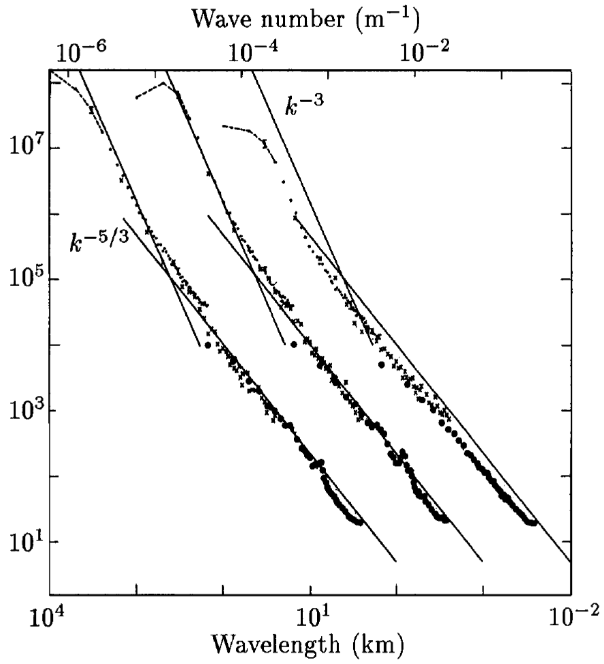

FIGURE 2.2. Atmospheric spectra of kinetic energy of the zonal and meridional wind components and potential energy measured by means of the potential temperature. The spectra of meridional wind and potential temperature are shifted one and two decades to the right, respectively. Reproduced from Nastrom & Gage (1985).

of large-scale coherent vortices might suppress vertical motion and allow for an inverse cascade (Xia *et al.* 2011).

In order to determine the direction of the cascade in the $k^{-5/3}$ range, other statistical quantities can be used in place of the energy spectrum. One such a quantity is the third order structure function D_{LLL}

$$\langle \delta u_L \delta u_L \delta u_L \rangle = \langle \left(u_L \left(\mathbf{x} + \mathbf{r} \right) - u_L \left(\mathbf{x} \right) \right)^3 \rangle \tag{2.16}$$

where u_L stands for the velocity component parallel to $\mathbf{r}$, and $\langle \cdot \rangle$ denotes the ensemble average. As opposed to the energy spectrum, the sign of D_{LLL} differs depending on the direction of the cascade, and therefore has been used to study the atmospheric dynamics (Lindborg 1999; Cho & Lindborg 2001). In three-dimensional turbulence, an exact relation can be derived (Kolmogorov 1941*a*)

$$D_{LLL} = -\frac{4}{5} \varepsilon_K r. \tag{2.17}$$

Its counterpart in two-dimensional turbulence was derived by Lindborg (1999) who found that D_{LLL} is always positive and has a cubic dependence in the

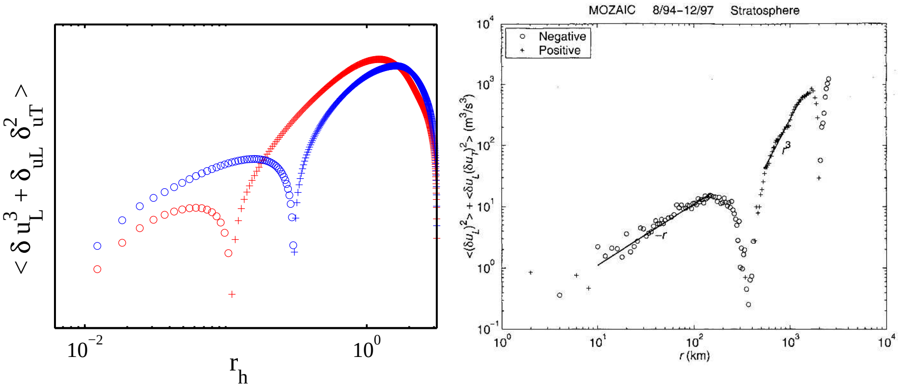

FIGURE 2.3. Comparison of the longitudial third order structure function D_{LLL} (*left*) from idealized geostrophic turbulence simulations (Vallgren *et al.* 2011) and (*right*) from measurements in the lower stratosphere (reproduced from Cho & Lindborg 2001).

enstrophy range

$$D_{LLL} = \frac{1}{8}\eta r^3, \tag{2.18}$$

and a linear dependence in the energy range

$$D_{LLL} = \frac{3}{2}Pr, \tag{2.19}$$

with η being the enstrophy dissipation and P being the energy injection rate. Analyses of the third order structure functions calculated from measurements in the lower stratosphere (Cho & Lindborg 2001) have shown a positive nearly-cubic behaviour at large scales, and a negative linear dependence at small scales, supporting the idea of a direct cascade of energy.

That the $k^{-5/3}$ range can be explained by a direct energy cascade poses the question where the energy feeding such a cascade could come from. As noted in the previous section, purely geostrophic dynamics is not consistent with a downscale energy transfer. In order to investigate such a process, high-resolution numerical simulations are needed, able to resolve both geostrophic and stratified turbulent dynamics. In the last decade, several numerical studies have been devoted to shed some lights into the dynamics, both using idealized box simulations (Kitamura & Matsuda 2006; Vallgren *et al.* 2011) and atmospheric models (Skamarock 2004; Takahashi *et al.* 2006; Hamilton *et al.* 2008; Waite & Snyder 2009).

In the following, we attempt to propose a possible interpretation of the large-scale turbulent dynamics in the atmosphere. Motivated by the robustness of the transition of the energy spectrum, somewhat independent of the location and altitude, we hypothesize that it must be generated by a strong physical mechanism. Thus, in order to investigate the underlying dynamics, we carry out idealized box-simulations of rotating and stratified turbulence forced only at large scales. As opposed to quasi-geostrophic dynamics, finite rotation rates lead to a finite downscale cascade of energy. The small scales dissipation is found to increase with increasing *Ro*. The energy cascade starts from the largest scales of the system and becomes evident only at small-scales, where it leads to a shallowing of the energy spectra to a $k^{-5/3}$ dependence, consistent with observations (Nastrom & Gage 1985). Third order structure function (in fig. 2.3), in agreement with Cho & Lindborg (2001), switches sign at the transition wavenumber. Negative signs with a linear dependence are attained at small scales, confirming the presence of a direct cascade of energy.

CHAPTER 3

Stratified turbulence in the presence of walls

Most of the flows in engineering applications and in nature develop over surfaces. From a practical point of view, the study of turbulence in the vicinity of a solid wall is crucial. Indeed, early experimental investigations (*e.g.* Reynolds 1886) were mainly devoted to wall-bounded turbulence. The presence of - at least - one inhomogeneous direction (normal to the wall, hereafter denoted by y) substantially increases the complexity of the problem, as compared to the homogeneous case. From a numerical point of view, more complex numerical schemes and discretizations are needed in order to deal with solid boundaries. It was as late as in the end of the 80s that computational resources had reached a level able to allow for wall-bounded turbulence simulations.

As in the isotropic homogeneous case, also turbulent flows over solid walls possess many scales. The largest scales (eddies) are usually set by the geometrical dimension of the flow, δ_{out}. In channel flows, for instance, they are proportional to the channel-height h whereas in boundary layers they are proportional to the boundary layer displacement thickness δ^*. On the other hand, close to the solid wall, very small structures develop which rather scale with the local shear stress τ_w. The lengthscale which can be formed by using τ_w and the kinematic viscosity ν,

$$l^+ = \nu\sqrt{\frac{\rho}{\tau_w}} = \frac{\nu}{u_\tau} \tag{3.1}$$

is often referred to as the viscous unit. Here, $u_\tau = \sqrt{\frac{\tau_w}{\rho}}$ represents the friction velocity. The ratio between the viscous unit and the geometrical dimension of the flow is referred to as the friction Reynolds number

$$Re_\tau = \frac{\delta_{out}}{l^+} = \frac{\delta_{out} u_\tau}{\nu}. \tag{3.2}$$

The presence of two different scales in the flow is indeed the idea underlying the hypothesis of the existence of the inner and outer scaling. Turbulence statistics at wall distances comparable to δ_{out} are universal and scale with δ_{out} and the outer velocity U_∞. On the other hand, close to the wall, at distances comparable to the viscous unit l^+, statistics scale in inner units, l^+ and u_τ. In the lower part of the inner region, $y < 5\,l^+$, velocity increases linearly with height, $u/u_\tau = y/l^+$. Such layer is usually referred to as viscous sub-layer. The two scalings match in an intermediate region. In such a layer, the velocity

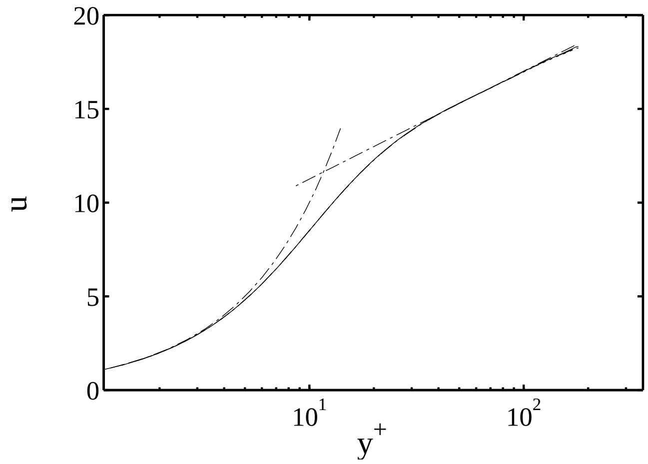

FIGURE 3.1. Typical mean streamwise velocity profile in the wall-normal direction for a turbulent wall-bounded flow (figure taken from Deusebio 2010).

gradient $\partial u/\partial y$ must become independent of ν and δ_{out}, and scale only with u_τ and the distance from the wall y. This suggests the presence of a logarithmic profile for the velocity, as seen in fig. 3.1.

In wall-bounded flows, turbulent motions are naturally forced by the wall-normal mean shear which extracts kinetic energy from the mean flow and transfers it to turbulent kinetic energy. Indeed, one of the most interesting feature of wall-bounded turbulence is that most of turbulent energy is produced very close to the wall, at $y^+ \approx 12$, where the velocity gradient is large. Thus, energy is injected at very small-scales, as opposed to homogeneous isotropic turbulence. How energy diffuses to larger scales, how outer structures interact with the near-wall structures and vice versa are issues not fully understood and whose understanding is crucial in order to improve turbulence modeling for wall-bounded flows (Jiménez 2012).

3.1. Numerical grids in wall-bounded flows

Since the first simulations in the 80s, numerical simulations of turbulent flows have heavily relied on the use of spectral methods (Canuto *et al.* 1988). As opposed to finite difference methods (FD) where the solution is approximated on a finite grid, in spectral methods (SM) the solution is approximated by an expansion of known globally-defined *ansatz* functions. Instead of solving for the values at the grid points, spectral methods solve for the expansion coefficients. The only approximation which is introduced is the truncation of the spectral expansion, whereas differential operators acting on the solution are exact. Due to the fact that *a priori* known functions are chosen, SM are not very flexible and only flows in fairly simple geometries can be studied. However, as compared to the *algebraic* convergence of the solution provided by finite difference methods, spectral methods allow for an *exponential* converge which had made them particularly useful, especially for turbulence simulations.

Several different bases can be used for the spectral expansion. The early studies of homogeneous isotropic turbulence (*e.g.* Orszag & Patterson 1972) widely employed Fourier modes. Apart from the existence of fast transform algorithms (Fast Fourier Transforms, hereafter FFTs), Fourier modes allow for very simple formulations of Partial Differential Equations (PDE) since they are the eigenfunctions of the differential operator. However, for wall-bounded flows, the inhomogeneity as well as the need for a non-equispaced grid (since wall structures are much finer as compared to the outer ones) make Fourier modes not suitable for wall-bounded turbulent simulations, at least in the wall-normal direction. In the early numerical studies of wall-bounded turbulence, Chebyshev polynomials were instead used and applied to Gauss-Lobatto grids

$$x_j/L = \cos\left(\pi\frac{j-1}{N-1}\right) \qquad\qquad j = 1, \cdots, N, \tag{3.3}$$

which allowed both to retain the use of FFTs and to provided a non-uniform distribution, with a clustering of points at the upper and lower boundaries, $y = \pm 1$. Such a grid is particularly suitable for flows confined by two solid walls, *e.g.* channel flows. However, if one aims at studying open flows which are bounded by only one solid wall, the clustering of points at the free-boundary is a waste.

One way to overcome this problem would be to use the method of Spalart *et al.* (2008) who employed Jacobi polynomials in the variable $\zeta = \exp(-y/Y)$, *i.e.* in an vertical grid exponentially stretched by a factor Y. Hoyas & Jiménez (2006) employed seven-point compact finite differences in place of the Chebyshev polynomials. In such a way, they were able to adapt the grid spacing to the local viscous lengthscale η. Nevertheless, the employed solution algorithm still imposes a clustering of points at the upper boundary. In paper 4, we propose an alternative method in order to study open-flows which satisfy the upper boundary condition

$$\frac{\partial u}{\partial y} = \frac{\partial w}{\partial y} = v = 0, \tag{3.4}$$

with u and w being the streamwise and spanwise velocities, respectively. We retain the use of Chebyshev polynomials. However, by noting that (3.4) can be viewed as a symmetric condition around the centreline (*i.e.* $y = 0$), we restrict ourself to flows which have symmetric u, w and antisymmetric v. Thus, we only consider even Chebyshev polynomials for u, w and odd polynomials for v. If a vertical stratification is present, the parity of the equation for v requires that the scalar field is odd.

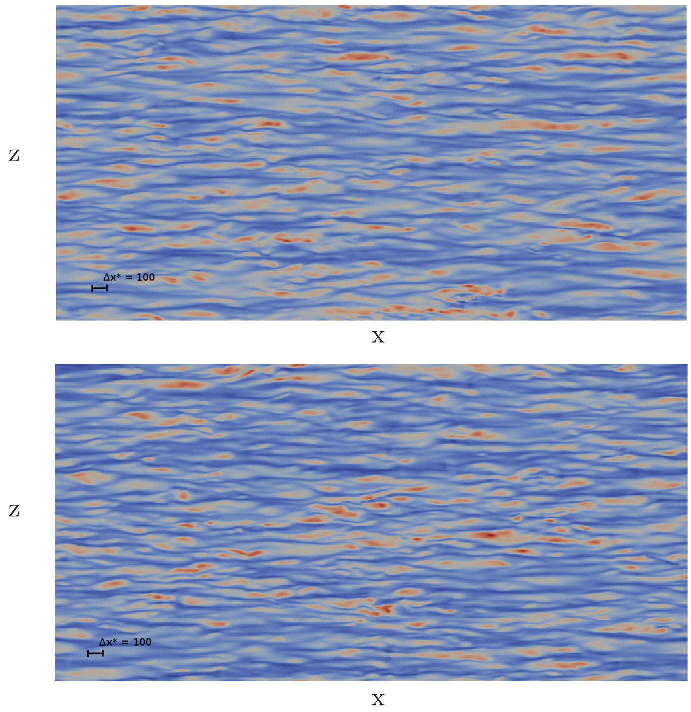

FIGURE 3.2. Streamwise velocity fluctuation close to the wall, at $y^+ = 10$ for unstratified case (*top*) and stratified case (*bottom*) with $h/L = 1.2$. The color ranges from 0.44 (*blue*) to 0.62 (*red*).

3.2. Stratified wall-bounded flows

The study of how stable stratification affects near-wall turbulence is crucial in order to understand how the atmospheric boundary layer dynamics changes during nights with clear sky and/or in polar regions, where the ground is cooled and the flow is subjected to a stable stratification. Turbulent dynamics influence how heat, momentum, moisture and pollution are exchanged and mixed close to the Earth surface. Atmospheric models need to be improved in order to take into account phenomena that arise in highly stably stratified flows, such as suppression of vertical motions, re-laminarization and appearance of gravity waves.

The effect of a stable stratification on wall-bounded turbulence have recently been addressed by a number of numerical experiments. Nieuwstadt (2005) and Flores & Riley (2010) focus on the turbulence collapse due to a strong cooling at the lower wall. Armenio & Sarkar (2002) and García-Villalba & del Álamo (2011) studied the property of statistically steady continuously turbulent flows strongly affected by stratification. Despite the fact that the temperature/density gradients are larger at the wall, near-wall structures are little affected by stable stratification. Figure 3.2 shows the instantaneous streamwise velocity in a plane very close to the wall for both an unstratified case and a stratified case. Streaky structures dominate both flows, in agreement with previous studies in wall-bounded turbulence. Moreover, such structures preserve their spacing of about 120 l^+ in both cases. Indeed, the wall dynamics of stratified flows is a competition between the production of turbulent kinetic energy due to shear and turbulent destruction, or rather, conversion to potential energy. At the wall, shear is indeed very high and dominates the dynamics. A measure of the relative importance of these two mechanisms is given by the ratio of the wall-normal distance and the so-called Monin-Obukhov lengthscale

$$y/L = y \frac{g\overline{v'\rho'}}{u_\tau^3 \rho_0}. \tag{3.5}$$

Assuming that the mean velocity is logarithmically increasing with height, the Monin-Obukhov lengthscale can in fact be interpreted as the distance at which the production

$$\overline{u'v'}\frac{\partial U}{\partial y} \tag{3.6}$$

and the turbulent destruction

$$\frac{g}{\rho_0}\overline{v'\rho'} \tag{3.7}$$

are in balance. Here, g stands for the gravitational acceleration, U for the mean velocity and the primes $\cdot'$ for the turbulent fluctuations. The overline $\bar{\cdot}$ denotes an ensemble average.

As we move further away from the wall, shear decreases and the role of stratification becomes more important. Due to the inhibition of the vertical motion, the transfer of momentum in the vertical direction due to turbulent motions is reduced. However, in steady conditions, the total streamwise momentum vertical flux,

$$-\overline{u'v'} + \nu\frac{\partial U}{\partial y}, \tag{3.8}$$

must stay constant. Thus, if $\overline{u'v'}$ reduces because of stratification, the flow must accelerate in such a way that shear increases. Figure 3.3 shows a cross-flow cut of the instantaneous streamwise velocity for an unstratified and a stratified case. The structures which populate the outer region of the flow become more confined in the vertical direction as stratification is increased. Indeed, structures well-correlated in the vertical direction can be seen to a less extent in the stratified case as compared to the unstratified case. Moreover, they also become narrower, supporting the idea of the existence of self-similar structures which grow both in the vertical and in the spanwise direction.

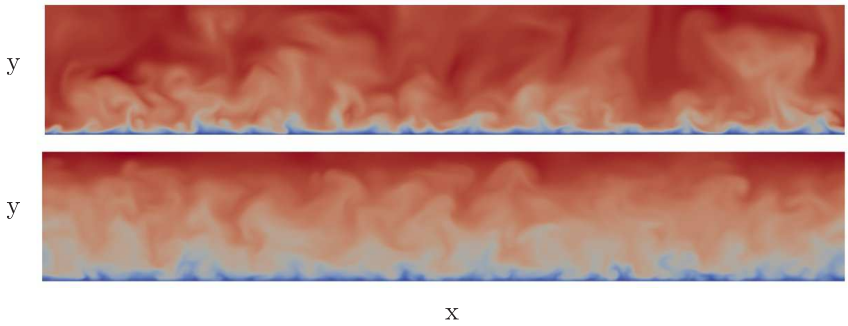

FIGURE 3.3. u_{rms}-field in a cross-flow plane, *i.e.* $y - z$, for an unstratified case (*top*) and a stratified case (*bottom*) with $h/L = 1.2$. The color ranges from 0 (*blue*) to 0.85 (*red*). Figure taken from Deusebio *et al.* (2011)

CHAPTER 4

Summary of the papers

Paper 1

Possible Explanation of the Atmospheric Kinetic and Potential Energy Spectra

In three dimensions (3D) there is a downscale energy cascade while there is an up-scale cascade in two dimensions (2D). In the Earth atmosphere where strong rotation and stratification are predominant, the 2D type of dynamics are important and a large fraction of the energy which is released at thousand kilometre scales goes into an up-scale cascade. However, a fraction of the energy may go downscale. As an idealized model for the atmospheric dynamics, we consider the primitive equations with strong system rotation. By carrying out a set of box simulations of turbulence forced only at large scales, we show that this fraction may not be negligible although it decreases with increased rotation rates. We also show that such a downscale energy cascade generates a transition in the wavenumber energy spectrum, from $\sim k^{-3}$ to $\sim k^{-5/3}$, consistent with observations. Also the third-order structure function agrees qualitatively with the observation in the atmosphere and presents a switch of sign at the transition scale. The negative sign and the linear dependence suggest a direct cascade as the mechanism underlying the $k^{-5/3}$ range in the atmosphere.

Paper 2

The route to dissipation in strongly stratified and rotating flows

We investigate the energy transfer in strongly stratified and rotating turbulent flows forced at large scales by means of box simulations of the primitive equations and the Boussinesq system. As opposed to QG-dynamics, a downscale energy cascade develops for finite rotation rates. The simulations of the Boussinesq system allow us to study the influence of a finite Froude number in the dynamics as well as the role of inertia-gravity wave motions. At large scales quasi-geostrophic dynamics is observed with both filamentation and large scale coherent vortices. However, also small scale turbulent patches appear in the dynamics. In these regions, the local vertical Froude number is of the order of unity, consistent with recent results in stratified turbulence. At large scales, potential and kinetic energy spectra attain scaling in agreement with QG-dynamics, $\sim k^{-3}$, with a transition to $k^{-5/3}$ at smaller scales resulting from the downscale cascade of energy. The small scale dissipation increases with decreasing rotation rates. On the other hand, stratification favours a downscale energy cascade, even though its effect is weaker as compared to the effect of rotation. At small but finite Rossby number, an energy and an enstrophy inertial cascade coexist in the same range of scales. The cascade of enstrophy is supported by interactions among geostrophic modes, whereas the cascade of energy is supported by interactions involving at least one ageostrophic mode. The effect on inertia-gravity waves in the cascade is studied. Frequency spectra of individual Fourier modes show clear signs of periodic motions only at large scales, while small-scale frequency spectra attain rather flat behaviour. The possible role of resonant triad interactions within the turbulent cascade is investigated. However, results show that such mechanism is of secondary importance and the downscale energy cascade is rather supported by turbulent-like interactions.

Paper 3

Direct numerical simulations of stratified open channel flows

We carry out direct numerical simulations (DNSs) of open-channel flows in order to study the influence of a stable stratification on wall-bounded turbulence at moderate Reynolds numbers, *i.e.* $Re_\tau = 360$. A negative heat-flux at the lower wall is forced in order to provide a positive vertical temperature gradient. The stable stratification is quantified by the ratio h/L, with h being the open-channel height and L being of the Moin-Obukhov lengthscale. At the Re_τ under consideration, values of h/L higher than 1.25 provides relaminarization of the flow, consistent with previous investigations. In this study, we focus on turbulent regimes, investigating how a stable stratification affects wall-bounded turbulent structures. Near-wall streaks are weakly affected and preserve the same spanwise spacing as in neutral cases, around $\lambda_z^+ \approx 120$. On the other hand, the largest structures in the outer region are damped and they become narrower as stratification increases. We also study the role of gravity waves in open-channel flows. Comparison with full channel flows are also presented. A new method able to highlight their presence is proposed. The method is based on the fact that gravity waves are able to carry energy but not heat-flux. Gravity waves develop mostly in the centre of the full channel where they account for almost 90% of the total vertical fluctuation. Such structures are very elongated in the spanwise direction with preferential streamwise wavelength of about $\lambda_x \approx 2 - 3$, in agreement with previous studies. On the other hand, open-channel flows show smaller signatures of wave activity in the outer layer, possibly due to the presence of the open-channel boundary condition which might inhibit their development. A wall-normal correlation analysis of the different Fourier modes is also performed. In neutral cases, the most well-correlated modes correspond to the outer streamwise elongated structures. For stratified cases, also gravity waves are expected to maintain high coherence in the vertical direction. This is confirmed by the results that, for stratified cases, show the presence of a new kind of modes beside the outer modes, with spatial extents matching the ones of the gravity waves.

Paper 4

The open-channel version of SIMSON

An existing pseudo-spectral code designed for numerical simulations of channel flows, called SIMSON, is modified in order to provide a better wall normal discretization for open-channel flows. The clustering of points at the free-shear boundary is avoided by using half Chebyshev polynomials: odd polynomials are used for the wall-normal velocity component while even polynomials are used for the other two components. The main code modifications are discussed. The performances and the validation of the code are presented. The improved grid allows the wall-normal resolution to be reduced leading to an overall speed-up of the code. In order for the code to be run on parallel machines, both one-dimensional and two-dimensional parallelization have been implemented. We also present some new features that have been implemented in order to meet the requirements of stratified flow simulations, such as a new CFL condition which accounts for an active scalar and damping regions for gravity waves.

CHAPTER 5

Conclusions and outlook

Since their maturity, digital computers have allowed for a number of advances in the understanding of turbulent processes. Their use have greatly increased over the years and is expected to increase even further in the future. Indeed, numerical simulation is a powerful tool, complementary to experiments, to be used in the context of turbulence research. In this thesis, we show how numerical simulations can effectively be used to study wall-bounded and homogeneous turbulence affected by stratification and rotation, allowing for some insights into the mechanisms of atmospheric turbulent dynamics.

5.1. Geostrophic turbulence

We have analysed the energy transfer in strongly stratified and rotating turbulence by means of box simulations of homogeneous turbulence, ranging from the QG limit to small but finite rotation rates and stratification. Forcing, necessary to obtain a steady turbulent cascade, was applied only at large scales. In QG turbulence, almost all the energy injected cascades up-scale. However, for finite rotations a forward energy cascade establishes. The amount of energy cascading downscale and up-scale is mainly controlled by the rotation rate. Stratification has a weaker effect as compared to rotation and favours a downscale cascade of energy. At small but finite rotation rates, the downscale energy cascade leads to a transition in the energy spectrum from k^{-3} to $k^{-5/3}$. The transition moves towards small scales as rotation rates are increased, as a result of the smaller amount of energy which cascades towards small scales. At small Ro, the geostrophic dynamics is little affected by the presence of an energy cascade, and a constant enstrophy flux range is observed, as expected in purely QG turbulence. The enstrophy cascade in supported by geostrophic interaction only. On the other hand, the downscale transfer of energy can only be achieved by interaction with at least one ageostrophic mode.

The use of an extremely idealized setup made it possible to study the backbone mechanism for the energy transfer underlying rotating and stratified turbulence dynamics, free of the additional multiple complexities present in measurements and global atmospheric models. Further studies using this rather simple setup may allow us to shed some light on other issues of practical interest, as, for instance, how predictability changes in highly rotating and stratified turbulent flows. Once the founding mechanism are understood, extensions to more complex cases are possible, but with a more critical perception of the physical dynamics and of possible spurious effects, as incorrect parametrization of the atmospheric processes. Indeed, analyses of more realistic data are needed in order to verify whether the hypothesis and the ideas proposed in this thesis can, to a larger extent, be applied to atmospheric dynamics.

5.2. Wall-bounded turbulence: towards the atmospheric boundary layer...

We have carried out direct numerical simulations of a turbulent open-channel flow and focused on the effect of an imposed external stable stratification on the structures of wall-bounded turbulence. Near-wall streaks are weakly affected and exhibit the same properties as the ones observed in the unstratified case. Larger differences are observed further away from the wall, where the shear diminishes and the effect of the stable stratification increases. Structures in the outer region become more confined in vertical direction, as expected by the suppression of the vertical motions, but also in the spanwise direction. Gravity waves mainly develop in the centre of the channel, thanks to the combined effect of the decrease of the shear and the reduction of the turbulence. However, the stress free upper boundary may prevent the development of gravity waves. Indeed, gravity wave activity is shown to be substantially stronger in full channels as compared to half channels.

Open-channel flows have been used as a model for the stably stratified atmospheric boundary layer dynamics in a number of recent numerical studies. Despite the similarities which connect open-channel flows and atmospheric boundary layers, one important difference has not been accounted for yet: the presence of a system rotation. Aiming at bridging simulations and reality, a rather natural follow-up of this study would be the investigation of the Ekman layer. Moreover, the increase of Re may also allow us to gain important insights on the wall-bounded turbulent dynamics and on the interactions between different scales. As the scale separations increases, footprints of outer structures on the near-wall cycle and vice-versa are expected to become more evident.

Acknowledgments

This work is - in my personal perspective - much more than a licentiate thesis. It is a leg in a journey, in an adventure which has filled and will still be filling my time. I am at the half, but reaching this point would not have been possible without the help of the people I met along the way.

In primis - my gratitude goes to my supervisor Erik Lindborg for supporting me and, most of all, for transmitting and sharing his great passion for turbulence. I also wish to thank my co-advisors Philipp Schlatter, for sharing his tremendous knowledge on numerics, and Geert Brethouwer, for many fruitful discussions and for his support at my very first conference in Rome. A special thank goes to Anders Dahlkild for kindly reading this manuscript and for providing many useful comments. I wish to thank Andreas Vallgren for being a great colleague and a good friend and for helping me to deal with successes and unsuccesses with the same good mood. A big thank also goes to Onofrio Semeraro for always offering his help, not only on work-related matters, without wishing anything back.

I wish to personally thank all those people, both within the university and outside of it, who have - in these years - accompanied my journey and have been beside me. I want to dedicate this work to all of them because without their presence and support - I'm sure - I would not have achieved it. Any success is not worth to be lived if there is no one to share the happiness with. And when some bad moments come, being a difficulty in our Phd or a broken elbow, it is important to have people that make you feel you are not alone. Thank you all for being there in both cases!

Finally, a special thanks goes to my family, Dada and Sara who has never given up on supporting me, even when my decisions led me far from them. *Vi voglio bene!*

Bibliography

ARMENIO, V. & SARKAR, S. 2002 An investigation of stably stratified turbulent channel flow using large-eddy simulation. *J. Fluid Mech.* **459**, 1–42.

BENZI, R., BIFERALE, L. & PARISI, G. 1993 On intermittency in a cascade model for turbulence. *Physica D: Nonlinear Phenomena* **65** (1-2), 163–171.

BIFERALE, L. & TOSCHI, F. 2001 Anisotropic Homogeneous Turbulence: Hierarchy and Intermittency of Scaling Exponents in the Anisotropic Sectors. *Physical Review Letters* **86**, 4831–4834.

BILLANT, P. & CHOMAZ, J.-M. 2000 Experimental evidence for a new instability of a vertical columnar vortex pair in a strongly stratified fluid. *Journal of Fluid Mechanics* **418**, 167–188.

BILLANT, P. & CHOMAZ, J.-M. 2001 Self-similarity of strongly stratified inviscid flows. *Physics of Fluids* **13** (6), 1645–1651.

BOFFETTA, G. 2007 Energy and enstrophy fluxes in the double cascade of two-dimensional turbulence. *Journal of Fluid Mechanics* **589**, 253–260.

BOUSSINESQ, J. 1877 Essai sur la the'orie des eaux courantes. *Imprimerie nationale - J. sav. 1'Acad. des Sci.* .

BRETHOUWER, G., BILLANT, P., LINDBORG, E. & CHOMAZ, J.-M. 2007 Scaling analysis and simulation of strongly stratified turbulent flows. *J. Fluid Mech.* **585**, 343–368.

CANUTO, C., HUSSAINI, M. Y., QUARTERONI, A. & ZANG, T. A. 1988 *Spectral methods in Fluid Dynamics*. Springer-Verlag.

CHARNEY, J. G. 1971 Geostrophic turbulence. *J. Atmos. Sci.* **28** (6), 1087–1094.

CHO, J. Y. N. & LINDBORG, E. 2001 Horizontal velocity structure functions in the upper troposphere and lower stratosphere 1. observations. *J. Geophys. Res.* **106** (D10), 10223–10232.

DEARDORFF, J. W. 1970 A numerical study of three-dimensional turbulent channel flow at large Reynolds numbers. *Journal of Fluid Mechanics* **41**, 453–480.

DEL ÁLAMO, J. C., JIMÉNEZ, J., ZANDONADE, P. & MOSER, R. D. 2006 Self-similar vortex clusters in the turbulent logarithmic region. *Journal of Fluid Mechanics* **561**, 329–358.

DEUSEBIO, E. 2010 An open channel version of SIMSON. *Tech. Rep.* KTH Mechanics, Stockholm, Sweden.

DEUSEBIO, E., SCHLATTER, P., BRETHOUWER, G. & LINDBORG, E. 2011 Direct numerical simulations of stratified open channel flows. *Journal of Physics: Conference Series* **318** (2), 022009.

Deusebio, E., Vallgren, A. & Lindborg, E. 2012 The route to dissipation in strongly stratified and rotating flows. *submitted to J. Fluid Mech.* .

Domaradzki, J. A. & Saiki, E. M. 1997 A subgrid-scale model based on the estimation of unresolved scales of turbulence. *Physics of Fluids* **9** (7), 2148–2164.

Feynman, R. P. 1964 *Feynman lectures on physics*.

Flores, O. & Riley, J. J. 2010 Analysis of turbulence collapse in stably stratified surface layers using direct numerical simulation. *Boundary-Layer Meteorology* **129** (2), 241–259.

Frehlich, R., Meillier, Y. & Jensen, M. L. 2008 Measurements of Boundary Layer Profiles with In Situ Sensors and Doppler Lidar. *Journal of Atmospheric and Oceanic Technology* **25**, 1328.

Frisch, U. 1996 *Turbulence*. Cambridge University Press.

García-Villalba, M. & del Álamo, J. C. 2011 Turbulence modification by stable stratification in channel flow. *Physics of Fluids* **23** (4), 045104.

Gargett, A. E., Hendricks, P. J., Sanford, T. B., Osborn, T. R. & Williams, A. J. 1981 A Composite Spectrum of Vertical Shear in the Upper Ocean. *Journal of Physical Oceanography* **11**, 1258–1271.

Gatski, T. B. & Speziale, C. G. 1993 On explicit algebraic stress models for complex turbulent flows. *Journal of Fluid Mechanics* **254**, 59–78.

Germano, M. 1992 Turbulence - The filtering approach. *Journal of Fluid Mechanics* **238**, 325–336.

Germano, M., Piomelli, U., Moin, P. & Cabot, W. H. 1991 A dynamic subgrid-scale eddy viscosity model. *Physics of Fluids* **3** (7), 1760–1765.

Gill, A. E. 1982 *Atmosphere-ocean dynamics*. Academic Press, New York.

Hamilton, K., Takahashi, Y. O. & Ohfuchi, W. 2008 Mesoscale spectrum of atmospheric motions investigated in a very fine resolution global general circulation model. *J. Geophys. Res.* **113** (18).

Hoyas, S. & Jiménez, J. 2006 Scaling of the velocity fluctuations in turbulent channels up to $re_\tau = 2003$. *Physics of Fluids* **18** (1), 011702.

Jiménez, J. 2012 Cascades in wall-bounded turbulence. *Annual Review of Fluid Mechanics* **44** (1), 27–45.

Kaneda, Y., Ishihara, T., Yokokawa, M., Itakura, K. & Uno, A. 2003 Energy dissipation rate and energy spectrum in high resolution direct numerical simulations of turbulence in a periodic box. *Physics of Fluids* **15** (2), L21–L24.

Kim, J., Moin, P. & Moser, R. 1987 Turbulence statistics in fully developed channel flow at low reynolds number. *J. Fluid Mech.* **177**, 133–166.

Kitamura, Y. & Matsuda, Y. 2006 The k_H^{-3} and $k_H^{-5/3}$ energy spectra in stratified turbulence. *Geophys. Res. Lett.* **33**, L05809.

Kolmogorov, A. N. 1941*a* Dissipation of energy in locally isotropic turbulence [In Russian]. *Dokl. Akad. Nauk SSSR* **32**, 19–21.

Kolmogorov, A. N. 1941*b* The local Structure of turbulence in incompressible viscous fluid for very large Reynolds numbers [In Russian]. *Dokl. Akad. Nauk SSSR* **30**, 299–303.

Kraichnan, R. H. 1967 Inertial ranges in two-dimensional turbulence. *Physics of Fluids* **10** (7), 1417–1423.

Legras, B., Santangelo, P. & Benzi, R. 1988 High-resolution numerical experiments for forced two-dimensional turbulence. *EPL (Europhysics Letters)* **5**, 37.

Lilly, D. K. 1983 Stratified turbulence and the mesoscale variability of the atmosphere. *J. Atmos. Sci.* **40** (3), 749–761.

Lindborg, E. 1999 Can the atmospheric kinetic energy spectrum be explained by two-dimensional turbulence? *J. Fluid Mech.* **388**, 259–288.

Lindborg, E. 2006 The energy cascade in a strongly stratified fluid. *J. Fluid Mech.* **550**, 207–242.

Lorenz, E. N. 1963 Deterministic Nonperiodic Flow. *Journal of Atmospheric Sciences* **20**, 130–148.

Maltrud, M. E. & Vallis, G. K. 1993 Energy and enstrophy transfer in numerical simulations of two-dimensional turbulence. *Physics of Fluids* **5**, 1760–1775.

Moin, P. & Mahesh, K. 1998 Direct Numerical Simulation: A Tool in Turbulence Research. *Annual Review of Fluid Mechanics* **30**, 539–578.

Moser, R. D. & Moin, P. 1987 The effects of curvature in wall-bounded turbulent flows. *Journal of Fluid Mechanics* **175**, 479–510.

Nastrom, G. D. & Gage, K. S. 1985 A climatology of atmospheric wavenumber spectra of wind and temperature observed by commercial aircraft. *J. Atmos. Sci.* **42**, 950–960.

Nastrom, G. D., Gage, K. S. & Jasperson, W. H. 1984 Kinetic energy spectrum of large-and mesoscale atmospheric processes. *Nature* .

Nieuwstadt, F. T. M. 2005 Direct numerical simulation of stable channel flow at large stability. *Boundary-Layer Meteorology* **116**, 277–299.

Ohkitani, K. 1990 Nonlocality in a forced two-dimensional turbulence. *Physics of Fluids A: Fluid Dynamics* **2** (9), 1529–1531.

Ohkitani, K. & Kida, S. 1992 Triad interactions in a forced turbulence. *Physics of Fluids A: Fluid Dynamics* **4** (4), 794–802.

Orszag, S. A. & Patterson, G. S. 1972 Numerical simulation of three-dimensional homogeneous isotropic turbulence. *Phys. Rev. Lett.* **28**, 76–79.

Ozmidov, R. V. 1965 On the turbulent exchange in a stably stratified ocean. *Izv. Acad. Sci. USSR, Atmos. Oceanic Phys.* **1**, 493–497.

Pedlosky, J. 1987 *Geophysical fluid dynamics*. Springer.

Rasam, A., Brethouwer, G., Schlatter, P., Li, Q. & Johansson, A. V. 2011 Effects of modelling, resolution and anisotropy of subgrid-scales on large eddy simulations of channel flow. *Journal of Turbulence* p. N10.

Reynolds, O. 1886 On the Theory of Lubrication and Its Application to Mr. Beauchamp Tower's Experiments, Including an Experimental Determination of the Viscosity of Olive Oil. *Royal Society of London Philosophical Transactions Series I* **177**, 157–234.

Reynolds, O. 1895 On the Dynamical Theory of Incompressible Viscous Fluids and the Determination of the Criterion. *Royal Society of London Philosophical Transactions Series A* **186**, 123–164.

Reynolds, W. C. 1990 The potential and limitations of direct and large eddy simulations. In *Whither Turbulence? Turbulence at the Crossroads* (ed. J. L. Lumley), *Lecture Notes in Physics, Berlin Springer Verlag*, vol. 357, pp. 313–343.

Richardson, L. F. 1922 *Weather Prediction by Numerical Process*. Dover Publications, Inc., New York.

Riley, J. J. & deBruynKops, S. M. 2003 Dynamics of turbulence strongly influenced by buoyancy. *Physics of Fluids* **15** (7), 2047–2059.

Riley, J. J., Metcalfe, R. W. & Weissman, M. A. 1981 Direct numerical simulations of homogeneous turbulence in density-stratified fluids. *AIP Conference Proceedings* **76** (1), 79–112.

Schlatter, P. & Örlü, R. 2010 Assessment of direct numerical simulation data of turbulent boundary layers. *Journal of Fluid Mechanics* **659**, 116–126.

Schlatter, P., Örlü, R., Li, Q., Brethouwer, G., Fransson, J. H. M., Johansson, A. V., Alfredsson, P. H. & Henningson, D. S. 2009 Turbulent boundary layers up to re[sub theta] = 2500 studied through simulation and experiment. *Physics of Fluids* **21** (5), 051702.

Scott, R. K. 2007 Nonrobustness of the two-dimensional turbulent inverse cascade. *Phys. Rev. E* **75**, 046301.

Segalini, A., Örlü, R., Schlatter, P., Alfredsson, H. P., Rüedi, J.-D. & Talamelli, A. 2011 A method to estimate turbulence intensity and transverse taylor microscale in turbulent flows from spatially averaged hot-wire data. *Experiments in Fluids* **51**, 693–700, 10.1007/s00348-011-1088-0.

Sillero, J. A., Borrell, G., Gungor, A. G., Jiménez, J., Moser, R. D. & Oliver, T. A. 2010 Direct simulation of the zero-pressure-gradient boundary layer up to Re¸=6000. In *APS Division of Fluid Dynamics Meeting Abstracts*.

Skamarock, W. C. 2004 Evaluating mesoscale nwp models using kinetic energy spectra. *Monthly Weather Review* **132** (12), 3019–3032.

Smagorinsky, J. 1963 General Circulation Experiments with the Primitive Equations. *Monthly Weather Review* **91**, 99.

Spalart, P. R. 1988 Direct simulation of a turbulent boundary layer up to R sub theta = 1410. *Journal of Fluid Mechanics* **187**, 61–98.

Spalart, P. R., Coleman, G. N. & Johnstone, R. 2008 Direct numerical simulation of the ekman layer: A step in reynolds number, and cautious support for a log law with a shifted origin. *Physics of Fluids* **20** (10), 101507.

Stolz, S. & Adams, N. A. 1999 An approximate deconvolution procedure for large-eddy simulation. *Physics of Fluids* **11** (7), 1699–1701.

Takahashi, Y. O., Hamilton, K. & Ohfuchi, W. 2006 Explicit global simulation of the mesoscale spectrum of atmospheric motions. *Geophys. Res. Lett.* **33**, L12812.

Taylor, G. I. 1923 Experiments on the Motion of Solid Bodies in Rotating Fluids. *Royal Society of London Proceedings Series A* **104**, 213–218.

Vallgren, A. 2011 Infrared reynolds number dependency of the two-dimensional inverse energy cascade. *J. Fluid Mech.* **667**, 463–473.

Vallgren, A., Deusebio, E. & Lindborg, E. 2011 A possible explanation of the atmospheric kinetic and potential energy spectra. *Phys. Rev. Lett.* **99**, 99–101.

Vallgren, A. & Lindborg, E. 2011 The enstrophy cascade in forced two-dimensional turbulence. *J. Fluid Mech.* **671**, 168–183.

Vallis, G. K. 2006 *Atmospheric and Oceanic Fluid Dynamics: Fundamentals and Large-scale Circulation; electronic version*. Leiden: Cambridge Univ. Press.

Waite, M. L. & Bartello, P. 2006 The transition from geostrophic to stratified turbulence. *J. Fluid Mech.* **568**, 89–108.

Waite, M. L. & Snyder, C. 2009 The Mesoscale Kinetic Energy Spectrum of a Baroclinic Life Cycle. *J. Atmos. Sci.* **66**, 883.

Xia, H., Byrne, D., Falkovich, G. & Shats, M. 2011 Upscale energy transfer in thick turbulent fluid layers. *Nat Phys* **7** (4), 321–324.

Part II

Papers

1

Paper 1

Possible Explanation of the Atmospheric Kinetic and Potential Energy Spectra

By Andreas Vallgren, Enrico Deusebio & Erik Lindborg

Linné Flow Centre, KTH Mechanics
SE-100 44 Stockholm, Sweden

Physical Review Letters, 107:26, 268501, 2011

We hypothesize that the observed wave number spectra of kinetic an potential energy in the atmosphere can be explained by assuming that there are two related cascade processes emanating from the same large scale energy source, a downscale cascade of potential enstrophy, giving rise to a k^{-3}-spectrum at synoptic scales and a downscale energy cascade giving rise to a $k^{-5/3}$-range at mesoscales. We also hypothesize that the amount of energy which is going into the downscale energy cascade is determined by the rate of system rotation, with zero energy going downscale in the limit of very fast rotation. To test these hypotheses we carry out a set of simulations of a system with strong rotation and stratification which is forced at a large scale. We find that the amount of energy which is going into the downscale energy cascade decreases monotonically with increased rate of rotation and show that the downscale energy cascade generates a transition in the wave number spectrum, from $\sim k^{-3}$ to $\sim k^{-4/3}$, consistent with observations. We also show that the transition between the two dynamic regimes is associated with a change of sign of the third order structure function of velocity differences, consistent with observations from the lower stratosphere.

The wavenumber spectra of horizontal wind and temperature in the atmosphere (Fig. 1) display a range at synoptic scales ($\sim 500 - 2000$ km) with an approximate k^{-3}-dependence and a range at mesoscales ($\sim 2 - 500$ km) with a $k^{-5/3}$-dependence, where k is the horizontal wavenumber (Nastrom *et al.* 1984; Nastrom & Gage 1985; Cho *et al.* 1999; Frehlich & Sharman 2010). The spectrum of horizontal wind can be taken to be equal to the kinetic energy spectrum while the spectrum of temperature can be translated into a potential energy spectrum, where the potential energy here is related to the restoring Archimedes force on a fluid element that is vertically displaced in a static stable atmosphere. A spectrum of the form $k^{-5/3}$ is found in 3D turbulence with a downscale energy cascade (Kolmogorov 1941*b*), but also in 2D turbulence with an up-scale energy cascade (Kraichnan 1967). Charney (1971) showed that strong rotation and stratification lead to a dynamics, which he named geostrophic turbulence, that is very similar to 2D turbulence in that there is a second quadratic invariant apart from energy. In 2D turbulence the second invariant is enstrophy (half the square of vorticity) while in geostrophic turbulence it is potential enstrophy, defined as half the square of potential vorticity, a quantity representing geostrophically balanced motions for which the velocity is tangential to the local isobar. In 2D/geostrophic turbulence enstrophy/potential enstrophy cascades downscale which gives rise to a k^{-3}-spectrum at higher wavenumbers than a characteristic forcing wavenumber while a $k^{-5/3}$-spectrum is found at lower wavenumbers.

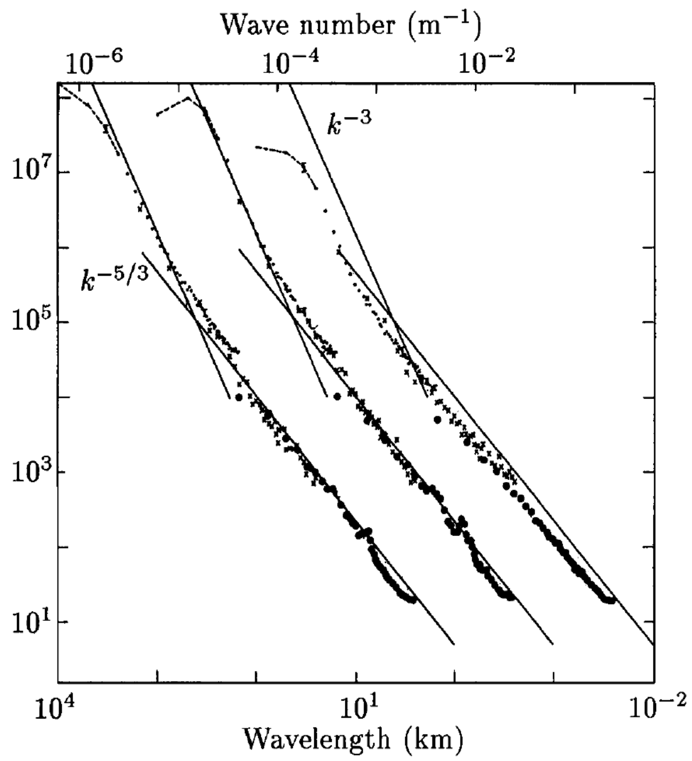

FIGURE 1. Atmospheric spectra of kinetic energy of the zonal and meridional wind components and potential energy measured by means of the potential temperature. The spectra of meridional wind and potential temperature are shifted one and two decades to the right, respectively. Reproduced from Nastrom & Gage (1985).

It has been hypothesized that the mesoscale $k^{-5/3}$-spectrum is produced by an upscale energy cascade (Gage 1979; Lilly 1983; Falkovich 1992). This hypothesis presumes that there is an important energy source at kilometer scales (Lilly 1989) in addition to baroclinic instability at thousand kilometre scales (Vallis 2006). Apart from the difficulty in identifying the nature of this energy source, there are several other difficulties associated with this hypothesis. Since the effect of the Earth's rotation is not very strong at such small scales, one has to assume that it is the effect of strong stratification that predominantly gives rise to the up-scale energy cascade (Lilly 1983). Numerical simulations of stratified turbulence have shown that strong stratification alone does not favour an up-scale cascade but rather a downscale cascade (Riley & deBruynKops 2003; Lindborg 2006; Brethouwer *et al.* 2007; Laval *et al.* 2003). Moreover, some success has been made in reproducing the transition from a k^{-3}-range to a $k^{-5/3}$-range in general circulation models (Takahashi *et al.* 2006; Hamilton *et al.* 2008), mesoscale models (Skamarock 2004; Skamarock & Klemp 2008) and idealized box simulations (Kitamura & Matsuda 2006; Molemaker & McWilliams 2010), without the introduction of any small-scale energy source. Despite this evidence pointing against the upscale cascade hypothesis, it was recently revived on the basis of the results of an experiment in a layer of fluid with electromagnetic small-scale forcing (Xia *et al.* 2011). The authors concluded that "it is possible that the suppression of 3D vertical eddies induces an inverse energy cascade through the mesoscales in the Earth atmosphere". It is remarkable that no scientific consensus yet has been reached on the important issue whether the energy cascade through the mesoscale range is up-scale or downscale.

We take a similar point of view as Tung & Orlando (2003), who argued that a weak downscale energy cascade is generated from the large-scale forcing, but is shadowed by the downscale cascade of potential enstrophy, which is producing a spectrum of the form $E(k) \sim \eta^{2/3} k^{-3}$ at synoptic scales, where η is the flux of potential enstrophy (Charney 1971). At a transition wave number $k_t \sim \sqrt{\eta/\epsilon}$, where ϵ is the downscale energy flux, the energy cascade will become visible and the spectrum will gradually change to $E(k) \sim \epsilon^{2/3} k^{-5/3}$. While Tung & Orlando (2003) assumed that the weak energy cascade is produced already in the limit of zero Rossby number (very strong rotation), we make the hypothesis that it is a finite Rossby number effect. To test this hypothesis, we consider the so called primitive equations

$$\frac{D\mathbf{u}_h}{Dt} = -\nabla_h p - f\mathbf{e}_z \times \mathbf{u}_h, \tag{1a}$$

$$0 = -\frac{\partial p}{\partial z} + Nb, \tag{1b}$$

$$\frac{Db}{Dt} = -Nw, \tag{1c}$$

$$\nabla \cdot \mathbf{u} = 0\,, \tag{1d}$$

where $\mathbf{u}$ is the velocity vector, $\mathbf{u}_h$ is the horizontal part of $\mathbf{u}$, w is the vertical velocity component, $\mathbf{e}_z$ is the vertical unit vector, p is the pressure, N is the Brunt-Väisälä frequency, $b = g\rho/(N\rho_0)$ is the buoyancy, where ρ and ρ_0 are the fluctuating and background densities, respectively, g is the acceleration due to gravity and f is the Coriolis parameter. We reformulate the system in terms of the potential vorticity and two ageostrophic components:

$$q = -\frac{\partial u}{\partial y} + \frac{\partial v}{\partial x} + \frac{f}{N}\frac{\partial b}{\partial z}, \tag{2a}$$

$$a_1 = -\frac{f}{N}\frac{\partial v}{\partial z} + \frac{\partial b}{\partial x}, \tag{2b}$$

$$a_2 = \frac{f}{N}\frac{\partial u}{\partial z} + \frac{\partial b}{\partial y}, \tag{2c}$$

where u and v are the velocity components in the x- and y-direction, respectively. The equations have been subject to nondimensionalization using geostrophic scaling (Charney 1971), *i.e.*

$$\begin{aligned} x \sim L, \quad y \sim L, \quad z \sim f/NL, \quad t \sim L/U, \\ u \sim U, \quad v \sim U, \quad w \sim Ro\,Uf/N, \quad b \sim U, \\ q \sim U/L, \quad a_1 \sim Ro\,U/L, \quad a_2 \sim Ro\,U/L, \end{aligned} \tag{3}$$

where $Ro = U/fL$ is the Rossby number.

Including small scale and large scale friction, the system can be rewritten as follows

$$\begin{aligned} \frac{\partial q}{\partial t} =& \frac{\partial}{\partial y}\left(\frac{\partial u^2}{\partial x} + \frac{\partial uv}{\partial y} + Ro\frac{\partial uw}{\partial z}\right) \\ &- \frac{\partial}{\partial x}\left(\frac{\partial uv}{\partial x} + \frac{\partial v^2}{\partial y} + Ro\frac{\partial vw}{\partial z}\right) \\ &- \frac{\partial}{\partial z}\left(\frac{\partial ub}{\partial x} + \frac{\partial vb}{\partial y} + Ro\frac{\partial wb}{\partial z}\right) \\ &+ \nu_S\nabla^8 q - \nu_L q, \end{aligned} \tag{4a}$$

$$\begin{aligned} Ro\frac{\partial a_1}{\partial t} =& a_2 - \frac{\partial w}{\partial x} + \frac{\partial}{\partial z}\left(\frac{\partial uv}{\partial x} + \frac{\partial v^2}{\partial y} + Ro\frac{\partial vw}{\partial z}\right) \\ &- \frac{\partial}{\partial x}\left(\frac{\partial ub}{\partial x} + \frac{\partial vb}{\partial y} + Ro\frac{\partial wb}{\partial z}\right) \\ &+ Ro\nu_S\nabla^8 a_1 - Ro\nu_L a_1, \end{aligned} \tag{4b}$$

$$\begin{aligned} Ro\frac{\partial a_2}{\partial t} =& -a_1 - \frac{\partial w}{\partial y} - \frac{\partial}{\partial z}\left(\frac{\partial u^2}{\partial x} + \frac{\partial uv}{\partial y} + Ro\frac{\partial uw}{\partial z}\right) \\ &- \frac{\partial}{\partial y}\left(\frac{\partial ub}{\partial x} + \frac{\partial vb}{\partial y} + Ro\frac{\partial wb}{\partial z}\right) \\ &+ Ro\nu_S\nabla^8 a_2 - Ro\nu_L a_2. \end{aligned} \tag{4c}$$

$$0 = \frac{\partial u}{\partial x} + \frac{\partial v}{\partial y} + Ro\frac{\partial w}{\partial z} \tag{4d}$$

Apart from the viscous parameters, the Rossby number constitutes the single adjustable parameter that enters the equations, whereas the Froude number, $Fr = U/LN$, is implicitly set to zero through the assumption (1b) of hydrostatic balance (Billant & Chomaz 2001). The inviscid, unforced system conserves total energy, $\left(u^2 + v^2 + b^2\right)/2$. In the limit $Ro = 0$, it reduces to Charney's equation which apart from energy also conserves potential enstrophy, $q^2/2$ (Charney 1971).

The system (4) is solved using a pseudo spectral method, with full dealiasing, in a triply-periodic ($2\pi \times 2\pi \times 2\pi$) domain with a resolution of 1024^3 grid points. Observe that the box is cubic in the space where the vertical coordinate is stretched by a factor of N/f. Translated to mid-latitude atmospheric dynamics this would correspond to a real space box aspect ratio of $f/N \sim 0.01$. The velocities are recovered by inverting the non-dimensional counterpart of (2) which contains the Rossby number but not the Froude number. A random forcing is introduced in the potential vorticity equation. The forcing is white noise in time and restricted to the wave number shell $k \in [3, 5]$, *i.e.* it is isotropic in the space where the vertical coordinate has been stretched. The potential enstrophy injection rate, η, is perfectly controlled and is set to unity. Consequently, the energy injection rate, P, is also a controlled parameter. We carry out six simulations for $Ro = [0, 0.025, 0.05, 0.075, 0.1, 0.2]$ and the corresponding values $\nu_S = [2.4,\ 1.9,\ 1.9,\ 1.9,\ 4.0,\ 6.2] \cdot 10^{-18}$ of the small scale viscous parameter, while the large scale viscous parameter has the same value $\nu_L = 0.12$ in all simulations. The Rossby number can also be interpreted as $Ro = \eta^{1/3}/f$. Cho & Lindborg (2001) made the estimate $\eta \sim 10^{-15}\mathrm{s}^{-3}$ from structure function analyses in lower stratosphere. If this value is representative for the atmosphere we would obtain $Ro \sim 0.1$ at midlatitude. The reason why we have increased ν_S in the two highest Rossby number simulations is that a larger amount of energy is going downscale in these simulations. To make sure that dissipation takes place at the resolution scale, Δx, we need a ν_S scaling as $\sim \epsilon^{1/3}(\Delta x)^{22/3}$, where ϵ is the downscale energy flux.

The total spectral energy flux can be calculated as

$$\begin{aligned}\Pi(k) = -\sum_{k'=0}^{k} \quad & Im\left[k_x\left(\widehat{u^2}\widehat{u}^* + \widehat{uv}\widehat{v}^* + \widehat{ub}\widehat{b}^*\right)\right. \\ & \quad +k_y\left(\widehat{v^2}\widehat{v}^* + \widehat{uv}\widehat{u}^* + \widehat{vb}\widehat{b}^*\right) \\ & \left. +Ro\, k_z\left(\widehat{uw}\widehat{u}^* + \widehat{vw}\widehat{v}^* + \widehat{wb}\widehat{b}^*\right)\right],\end{aligned} \tag{5}$$

where the hat denotes the Fourier transform and $k' = \sqrt{k_x^2 + k_y^2 + k_z^2}$. In Fig. 2a, we see $\Pi(k)$ normalized by the energy injection rate P. There is a monotonic decrease of Π/P with increased rate of rotation. For all Rossby numbers, there is a range of constant positive flux, ϵ, showing that there is a downscale energy cascade. In each constant energy flux range there is negligible dissipation. For $Ro = 0$ less than one thousandth of the injected energy is going downscale. For $Ro > 0$, we we find that $\epsilon \propto Ro^{1.5}P$, approximately. In Fig. 2b, we see the horizontal spectra of total energy. For both $Ro = 0.2$ and $Ro = 0.1$ we find a clear range where the total energy spectrum scales as $E(k) = C\epsilon^{2/3}k^{-5/3}$, with $C \approx 1.1$ for $Ro = 0.2$ and $C \approx 1.4$ for $Ro = 0.1$. We find that the ratio between the kinetic and potential energy is a little bit larger than two in this range, consistent with previous simulations of stratified turbulence (Lindborg 2006). For $Ro = 0$, the spectrum is slightly steeper than, but close to, $\mathcal{K}\eta^{2/3}k^{-3}$ with $\mathcal{K} \approx 2.2$, consistent with the prediction of Charney (1971) and previous simulations of geostrophic turbulence (Vallgren & Lindborg 2010). For $Ro = 0.025$, the spectrum is slightly more shallow than k^{-3}.

The sign and the magnitude of the kinetic energy flux, ϵ_K, can be estimated by measuring third order velocity structure functions, which are third-order statistical moments of differences between the velocity components measured

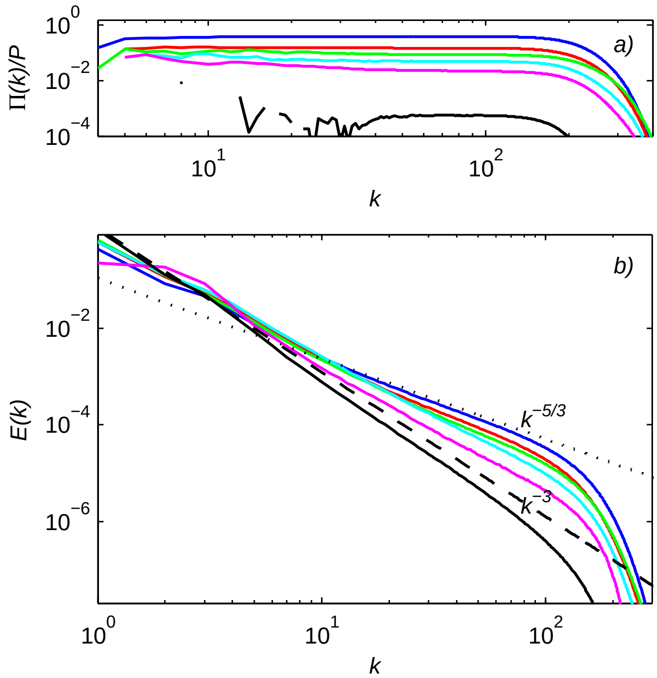

FIGURE 2. *a)* Energy flux as a function of wavenumber k normalized by the energy injection rate. The magnitude of the flux is increasing with increasing Rossby number. From bottom to top: $Ro = [0, 0.025, 0.05, 0.075, 0.1, 0.2]$, *b)* energy spectrum for different Rossby numbers with the same colours as in a. The k^{-3}- (dashed) and $k^{-5/3}$-slopes (dotted) are indicated.

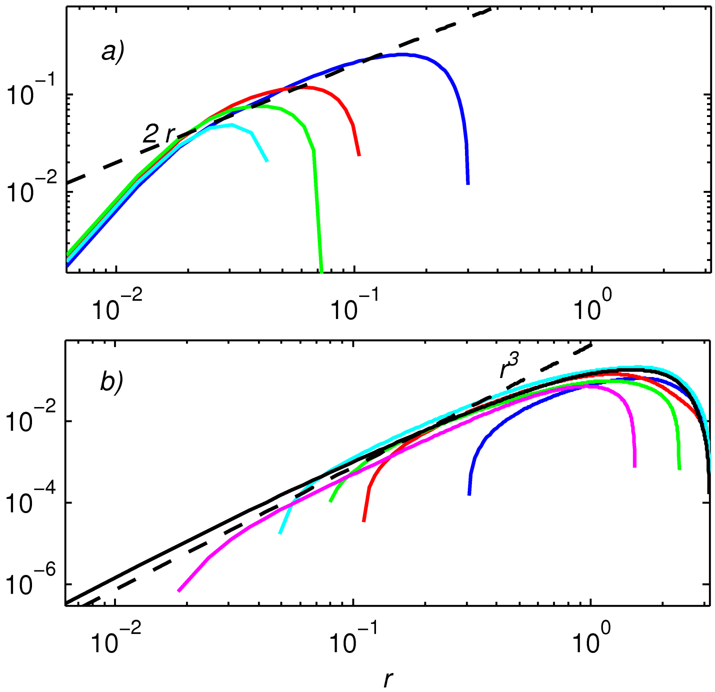

FIGURE 3. Third order structure function D, for different Rossby numbers, with the some colors as in figure 2. *a)* Negative range normalized by the kinetic energy dissipation rate, *b)* positive range normalized by the enstrophy injection rate. The theoretically predicted slopes are indicated.

at two points which are separated by a distance r. Kolmogorov (1941*a*) derived the relation $D_{LLL} = -4\epsilon_K r/5$, for the longitudinal third order structure function of isotropic 3D turbulence, where L refers to the direction of the separation vector $\mathbf{r}$. For 2D turbulence a similar derivation, Lindborg (1999) gives $D_{LLL} = -3\epsilon_K r/2$ where ϵ_K in this case is negative since the cascade is up-scale. In the enstrophy cascade range of 2D turbulence one finds that $D_{LLL} = \eta r^3/8$, where η here is the enstrophy flux (Lindborg 1999). Wind data from the lower stratosphere were used to calculate the sum $D = D_{LLL} + D_{LTT}$, where T refers to a velocity component perpendicular to $\mathbf{r}$ (Cho & Lindborg 2001). It was found that D has a negative linear dependence on r at mesoscales. At $r \approx 300$ km, D switches sign and at synoptic scales there is a narrow range where D approximately scales as $\sim r^3$. In Fig. 3a we see that D is preferentially negative in the higher Rossby number runs, with a change of sign moving towards larger scales with increasing Rossby number. In the highest Rossby number runs we find that $D \approx -2\epsilon_K r$, in the forward energy cascade range, which is the relation that was used to estimate ϵ_K (Cho & Lindborg 2001). In

Fig. 3b we see that D is preferentially positive for the lowest Rossby number runs for which $D \sim r^3$, with a particular good agreement for $Ro = 0$.

With a forcing acting at a particular wave number k_f the enstrophy and the energy injection rates are approximately related as $\eta = k_f^2 P$. With $\epsilon \sim Ro^{3/2} P$ we can thus estimate the transition wave number as $k_t \sim \sqrt{\eta/\epsilon} \sim Ro^{-3/4} k_f$. In the atmosphere, the most unstable wave number of baroclinic instability can be estimated as $k_f \sim 2\pi/(4L_R)$, where L_R is the Rossby deformation radius. If the relation $\epsilon \sim Ro^{3/2} P$ also would hold in the atmosphere, we would thus obtain a transition wave number $k_t \sim \pi Ro^{-3/4}/(2L_R)$ and a corresponding transition scale $L_t \sim 4 L_R Ro^{3/4}$. With $L_R = 1000$ km and $Ro = 0.1$, we obtain $L_t \sim 700$ km, in reasonable agreement with observation (Figure 1).

In agreement with previous simulations (Molemaker & McWilliams 2010; Hamilton *et al.* 2008; Skamarock & Klemp 2008; Koshyk & Hamilton 2001) and data analysis (Lindborg 2007), our simulations show that the kinetic energy content in horizontally divergent modes is of the same order of magnitude as the content in rotational modes, in the mesoscale range. Koshyk & Hamilton (2001) interpreted the energy content in the divergent modes as a signal of gravity waves. In a future study, we will address the issue of the possible importance of gravity waves by carrying out frequency analyses.

In conclusion, our numerical experiment shows that the same type of spectrum as found in the atmosphere can be generated from a single energy source in a system with strong stratification and strong but finite rotation. The experiment suggests that the atmospheric $k^{-5/3}$ mesoscale spectrum can be explained by the existence of a downscale energy cascade whose strength is regulated by the Rossby number. Moreover, the simulations show a third-order structure function, D, which is consistent with observations from the lower stratosphere.

Computer time provided by SNIC (Swedish National Infrastructure for Computing) is gratefully acknowledged.

References

Billant, P. & Chomaz, J.-M. 2001 Self-similarity of strongly stratified inviscid flows. *Physics of Fluids* **13** (6), 1645–1651.

Brethouwer, G., Billant, P., Lindborg, E. & Chomaz, J.-M. 2007 Scaling analysis and simulation of strongly stratified turbulent flows. *J. Fluid Mech.* **585**, 343–368.

Charney, J. G. 1971 Geostrophic turbulence. *J. Atmos. Sci.* **28** (6), 1087–1094.

Cho, J. Y. N. & Lindborg, E. 2001 Horizontal velocity structure functions in the upper troposphere and lower stratosphere 1. observations. *J. Geophys. Res.* **106** (D10), 10223–10232.

Cho, J. Y. N., Newell, R. E. & Barrick, J. D. 1999 Horizontal wavenumber spectra of winds, temperature, and trace gases during the Pacific exploratory missions: 2. Gravity waves, quasi-two-dimensional turbulence, and vortical modes. *J. Geophys. Res.* **104**, 16297–16308.

Falkovich, G. 1992 Inverse cascade and wave condensate in mesoscale atmospheric turbulence. *Phys. Rev. Lett.* **69** (22), 3173–3176.

Frehlich, R. & Sharman, R. 2010 Climatology of Velocity and Temperature Turbulence Statistics Determined from Rawinsonde and ACARS/AMDAR Data. *Journal of Applied Meteorology and Climatology* **49**, 1149–1169.

Gage, K. S. 1979 Evidence for a k to the -5/3 law inertial range in mesoscale two-dimensional turbulence. *J. Atmos. Sci.* **36**, 1950–1954.

Hamilton, K., Takahashi, Y. O. & Ohfuchi, W. 2008 Mesoscale spectrum of atmospheric motions investigated in a very fine resolution global general circulation model. *J. Geophys. Res.* **113** (18).

Kitamura, Y. & Matsuda, Y. 2006 The k_H^{-3} and $k_H^{-5/3}$ energy spectra in stratified turbulence. *Geophys. Res. Lett.* **33**, L05809.

Kolmogorov, A. N. 1941*a* Dissipation of energy in locally isotropic turbulence [In Russian]. *Dokl. Akad. Nauk SSSR* **32**, 19–21.

Kolmogorov, A. N. 1941*b* The local Structure of turbulence in incompressible viscous fluid for very large Reynolds numbers [In Russian]. *Dokl. Akad. Nauk SSSR* **30**, 299–303.

Koshyk, J. N. & Hamilton, K. 2001 The Horizontal Kinetic Energy Spectrum and Spectral Budget Simulated by a High-Resolution Troposphere-Stratosphere-Mesosphere GCM. *J. Atmos. Sci.* **58**, 329–348.

Kraichnan, R. H. 1967 Inertial ranges in two-dimensional turbulence. *Physics of Fluids* **10** (7), 1417–1423.

Laval, J. P., McWilliams, J. C. & Dubrulle, B. 2003 Forced stratified turbulence: Successive transitions with reynolds number. *Phys. Rev. E* **68** (3), 036308.

Lilly, D. K. 1983 Stratified turbulence and the mesoscale variability of the atmosphere. *J. Atmos. Sci.* **40** (3), 749–761.

Lilly, D. K. 1989 Two-Dimensional Turbulence Generated by Energy Sources at Two Scales. *J. Atmos. Sci.* **46**, 2026–2030.

Lindborg, E. 1999 Can the atmospheric kinetic energy spectrum be explained by two-dimensional turbulence? *J. Fluid Mech.* **388**, 259–288.

LINDBORG, E. 2006 The energy cascade in a strongly stratified fluid. *J. Fluid Mech.* **550**, 207–242.

LINDBORG, E. 2007 Horizontal wavenumber spectra of vertical vorticity and horizontal divergence in the upper troposphere and lower stratosphere. *J. Atmos. Sci.* **64**, 1017–1025.

MOLEMAKER, M. J. & MCWILLIAMS, J. C. 2010 Local balance and cross-scale flux of available potential energy. *J. Fluid Mech.* **645**, 295–314.

NASTROM, G. D. & GAGE, K. S. 1985 A climatology of atmospheric wavenumber spectra of wind and temperature observed by commercial aircraft. *J. Atmos. Sci.* **42**, 950–960.

NASTROM, G. D., GAGE, K. S. & JASPERSON, W. H. 1984 Kinetic energy spectrum of large-and mesoscale atmospheric processes. *Nature* **310**, 36–38.

RILEY, J. J. & DEBRUYNKOPS, S. M. 2003 Dynamics of turbulence strongly influenced by buoyancy. *Physics of Fluids* **15** (7), 2047–2059.

SKAMAROCK, W. C. 2004 Evaluating mesoscale nwp models using kinetic energy spectra. *Monthly Weather Review* **132** (12), 3019–3032.

SKAMAROCK, W. C. & KLEMP, J. B. 2008 A time-split nonhydrostatic atmospheric model for weather research and forecasting applications. *J. Comput. Phys.* **227**, 3465–3485.

TAKAHASHI, Y. O., HAMILTON, K. & OHFUCHI, W. 2006 Explicit global simulation of the mesoscale spectrum of atmospheric motions. *Geophys. Res. Lett.* **33**, L12812.

TUNG, K. K. & ORLANDO, W. W. 2003 The k^{-3} and $k^{-5/3}$ energy spectrum of atmospheric turbulence: Quasigeostrophic two-level model simulation. *J. Atmos. Sci.* **60** (6), 824–835.

VALLGREN, A. & LINDBORG, E. 2010 Charney isotropy and equipartition in quasi-geostrophic turbulence. *J. Fluid Mech.* **656**, 448–457.

VALLIS, G. K. 2006 *Atmospheric and Oceanic Fluid Dynamics: Fundamentals and Large-scale Circulation; electronic version*. Leiden: Cambridge Univ. Press.

XIA, H., BYRNE, D., FALKOVICH, G. & SHATS, M. 2011 Upscale energy transfer in thick turbulent fluid layers. *Nat Phys* **7** (4), 321–324.

Paper 2

2

The route to dissipation in strongly stratified and rotating flows

By Enrico Deusebio, Andreas Vallgren & Erik Lindborg

Linné Flow Centre, KTH Mechanics
SE-100 44 Stockholm, Sweden

Submitted - Journal of Fluid Mechanics

We investigate the route to dissipation in strongly stratified and rotating systems through high resolution numerical simulations of homogeneous turbulence in a triply periodic domain forced at large scales. For large rotation rates, quasi-geostrophic dynamics are recovered with a forward enstrophy cascade and an inverse energy cascade. As the rotation rate is reduced, a fraction of the energy starts to cascade towards smaller scales, leading to a shallowing of the horizontal spectra from k_h^{-3} to $k_h^{-5/3}$ at the small scale end. The high resolutions employed allow us to capture both ranges within the same simulation. At the transition scale, kinetic energy in the rotational and in the horizontally divergent modes attain comparable values. The divergent energy is several orders of magnitude larger than the quasi-geostrophic divergent energy given by the Ω-equation. The amount of energy cascading downscale is mainly controlled by the rotation rate, with a weaker dependence on the stratification. A larger degree of stratification favours a downscale energy cascade. For intermediate degrees of rotation and stratification, a constant energy flux and a constant enstrophy flux coexist within the same range of scales. In this range, the enstrophy flux is a result of triad interactions involving three geostrophic modes, while the energy flux is a result of triad interactions involving at least one ageostrophic mode, with a dominant contribution from interactions involving two ageostrophic and one geostrophic mode. Dividing the ageostrophic motions into two classes depending on the sign of the linear wave frequency, we show that the energy transfer is for the largest part supported by interactions within the same class, ruling out the wave-wave-vortex resonant triad interaction as a mean of the downscale energy transfer. The role of inertia-gravity waves is studied through analyses of time-frequency spectra of single Fourier modes. At large scales, distinct peaks at frequencies predicted for linear waves are observed, whereas at small scales no clear wave activity is observed. Triad interactions show a behaviour which is consistent with turbulent dynamics, with a large exchange of energy in triads with one small and two large comparable wavenumbers. The exchange of energy is mainly between the modes with two comparable wavenumbers.

1. Introduction

Flows in the atmosphere and in the oceans develop over an extremely wide range of scales, both in time and space. The atmosphere is largely forced at scales of the order of thousand kilometres, where baroclinic instability converts available potential energy, related to the meridional temperature gradient, to kinetic energy. Similarly, the general circulation of the oceans is mainly driven by surface fluxes of momentum at scales as large as 1000 km. On the other hand, the dissipation of energy can only be achieved by molecular friction and diffusion. As opposed to the large-scale forcing, viscosity and diffusivity act at very small scales, which can be estimated to be of the order of centimetres. How energy can cascade from the largest to the smallest scales, over a range of about eight orders of magnitude, is not fully understood (Muller *et al.* 2005). Even though the nonlinearities in the Navier-Stokes equations provide a mechanism for energy transfer between scales, the routes to dissipation are presently not clear. The general problem of how energy can be transferred from the very largest to the very smallest scales in geophysical flows has recently been the subject of several studies (Muller *et al.* 2005; Waite & Bartello 2006; Molemaker *et al.* 2010).

At synoptic scales, on the order of thousand kilometres, atmospheric dynamics are highly affected by both rotation and stratification. The relative importance of Coriolis forces and buoyancy forces as compared to inertial forces are often quantified by the Rossby and the Froude numbers, defined as

$$Ro = \frac{U}{fL}, \qquad Fr = \frac{U}{NL}. \tag{1}$$

Here, U is a characteristic velocity, L a characteristic length, $f = 2\Omega \sin\theta$ is the Coriolis parameter, with Ω being the rotation rate and θ the latitude, and N is the Brunt-Väisälä frequency. In the limit of very strong rotation and stratification, the Navier-Stokes (NS) equations can be reduced to the so-called quasi-geostrophic (QG) equation, stating that the potential vorticity, q, is materially conserved (Charney 1971). Therefore, QG conserves independently two quadratic invariants: total energy, which is the sum of potential and kinetic energy, and potential enstrophy, defined as $q^2/2$. In this limit there is an inverse cascade of energy dominating the large scales and a forward cascade of enstrophy dominating the small scales, just as in two-dimensional turbulent flows (Kraichnan 1967). The energy spectrum scales as $k^{-5/3}$ in the energy inertial range and as k^{-3} in the enstrophy inertial range. Recent high-resolution numerical simulations (Scott 2007; Boffetta & Musacchio 2010; Vallgren & Lindborg 2011) have mainly confirmed this picture, although some anomalous effects due to large scale vortices have also been reported (Scott 2007; Vallgren 2011).

Cambon *et al.* (1997) studied the effect of system rotation on the downscale energy transfer. As the rotation rate is increased, the energy cascade is inhibited and the forward energy transfer terms are damped, leading to a reduction of the small scales dissipation. Indeed, the inverse-cascade dynamics of strongly rotating and stratified systems seem to be inconsistent with small-scale energy dissipation, posing the intriguing question on how and where the energy transfer to small scales takes place (Muller *et al.* 2005). An interesting perspective is offered by the hypothesis that finite rotation rates lead to a transfer of energy from balanced, geostrophic motions to unbalanced motions (Bartello 1995; Waite & Bartello 2006; Molemaker *et al.* 2010). The QG equation is not able to capture this process. Therefore, Boussinesq system should rather be considered. When hydrostasy is assumed in the vertical direction, the Boussinesq system is often referred to as Primitive Equations. Stability analysis of a non-geostrophic and non-hydrostatic Eady problem shows the appearance of new kind of instabilities apart from the classical baroclinic instability. Such instabilities may lead to a transfer of energy from geostrophic to ageostrophic motions (Molemaker *et al.* 2005). Viúdez & Dritschel (2006) studied the breakdown of a baroclinic geostrophic jet, finding the emission of unbalanced wave motions with frequencies close to the inertial frequency. Moreover, it has recently been shown that forced Eady flows can relax to statistically stationary states only if ageostrophic motions are taken into account (Molemaker & McWilliams 2010). That is to say, QG flows cannot establish efficient and steady routes to dissipation.

Numerical simulations of strongly stratified flows (Riley & deBruynKops 2003; Waite & Bartello 2004; Lindborg 2006; Brethouwer *et al.* 2007) have shown that a forward energy cascade can develop and that a steady route to dissipations can be maintained, also in weakly rotating systems (Lindborg 2006; Waite & Bartello 2006). Using an eddy-damped quasinormal Markovian (EDQNM) closure, Godeferd & Cambon (1994) argued that a stable stratification may create a strongly anisotropic structure which prevents the development of an inverse cascade of energy. As already noted by Lilly (1983), stratification results in a decoupling of the dynamics into layers, leading to large gradients in the vertical direction. The resulting Kelvin-Helmholtz instabilities (KM) provide a mechanism for a downscale energy cascade. Whereas the horizontal Froude number, $Fr_h = U/Nl_h$, is very small, KH instabilities keep the vertical Froude number, $Fr_v = U/Nl_v$, of the order of unity (Billant & Chomaz 2001; Riley & deBruynKops 2003), naturally setting the flow layers thickness. Here, l_h and l_v are the characteristic horizontal and vertical length scale, respectively. The ratio $\alpha = l_v/l_h = Fr_h/Fr_v$ is a very small quantity in strongly stratified flows, which means that flow structures are highly elongated in the horizontal direction and very confined in the vertical. Such structures are often referred to as pancake structures. Waite & Bartello (2006) studied the vertical length scales for stratified and rotating geostrophic turbulence. For small Ro, they found that the scaling suggested by Charney (1971), $l_v \sim l_h\, f/N$, applies. On the other hand, for $Ro > 0.1$, Fr_v became of the order of unity and independent of Ro and Fr, in agreement with the prediction of Billant & Chomaz (2001) for stratified turbulence. As in three-dimensional turbulence, both kinetic and potential horizontal wavenumber energy spectra of strongly stratified flows scale as $k_h^{-5/3}$. Lindborg & Brethouwer (2007) showed that in this range, rotational and divergent modes, often referred to as wave and vortical modes, have comparable magnitude. In contrast to what has been suggested in many studies (*e.g.* Lelong & Riley 1991), they showed that there is no strict dynamic decoupling between these two types of modes. The reason for this is that they develop on comparable time scales, as suggested by the analysis of Billant & Chomaz (2001).

Observations in the oceans and in the atmosphere support the hypothesis that there is a downscale energy cascade over a wide range of scales. In the oceans, Ménesguen *et al.* (2009) studied the structure of long-lived anticyclonic lens-shaped vortices known as Meddies through fine resolution geoseismic sections and high-resolution numerical simulations. They were able to demonstrate the presence of a downscale energy cascade over roughly one decade, extending up to scales on the order of 3 km. In the atmosphere, wind and potential temperature spectra calculated from aircraft measurements (Nastrom & Gage 1985; Cho & Lindborg 2001) show two distinct range of scales. At synoptic scales, between 500 and 1000 km, a k_h^{-3} spectrum is found, consistent with a 2D-like turbulent dynamics within the enstrophy range. In the mesoscale range, below 500 km, the spectra shallow significantly, attaining scaling exponents close to $-5/3$. Third-order structure function analysis has revealed that there is a downscale energy flux in this range (Cho & Lindborg 2001).

The transition from a k_h^{-3} to a $k_h^{-5/3}$ spectrum have been simulated both in idealized numerical simulations (Kitamura & Matsuda 2006; Vallgren *et al.* 2011) and atmospheric models (Skamarock 2004; Takahashi *et al.* 2006; Hamilton *et al.* 2008; Waite & Snyder 2009). Vallgren *et al.* (2011) simulated the primitive equations in a triply periodic domain forced only at large scales. The ratio between the energy going down- and up-scale was found to increase with Ro and the small-scale dissipation was found to scale as $Ro^{3/2}$. The increasing amount of energy going downscale as Ro was increased led to a shallowing of the energy spectra to $k_h^{-5/3}$, consistent with observations.

At the present point, it is not entirely clear whether the forward energy cascade is a result of stratified turbulence or resonant interacting waves. Several theories based on the assumption that waves play a central role in the route to dissipation have been proposed. In the atmosphere, Waite & Snyder (2009) simulated an idealized baroclinic wave life cycle, finding a shallowing of the kinetic energy spectra due to the divergent contributions. The authors argued that waves spontaneously emitted in the dynamics propagate vertically and lead to the shallowing of the energy spectra. In the ocean, spectra show remarkable similarities from place to place, as described by Garrett & Munk (1979), who proposed a model (later improved by Munk 1981) for describing the frequency and vertical wavenumber spectra (hereafter referred to as GM spectra). A k_z^{-2} spectrum down to scales of roughly 10 m is predicted, followed by a steepening to k_z^{-3} for wavelengths smaller than 1 m. The GM spectrum is usually interpreted as the results of the superposition of saturated waves: the transition to k_z^{-3} is assumed to be set by the onset of wave instabilities, *i.e.*

waves reaching the critical steepness $u_{rms}/c_x > 1$, where u_{rms} is the velocity fluctuation and c_x is the phase velocity of the wave. Nevertheless, it must be noted that vertical spectra of the form $N^2 k_z^{-3}$ is also predicted by theories of stratified turbulence (Billant & Chomaz 2001). Such a prediction has recently been confirmed by direct numerical simulations (Augier *et al.* 2012) of strongly stratified flows at scales larger than the Ozmidov length scale without the presence of any clear strong wave signals. That stratified turbulence may also be an important dynamical process in the oceans is supported by the observations and the simulations of Ménesguen *et al.* (2009).

The nonlinear terms in the Navier-Stokes equations allow energy to be transferred among the different modes, involving triads in spectral space. Through resonant interaction waves can support an energy transfer towards small scales without involving any turbulent-like motions (Bellet *et al.* 2006). Phillips (1981) and Staquet & Sommeria (2002) reviewed the condition and the mechanism for sub-harmonic parametric instability (SPI) for which a long wave (k_0) resonantly interact with two high wavenumber secondary waves ($k_1, k_2 >> k_0$) which have half the frequency with respect to the primary wave ($\omega_1 = \omega_2 = -\omega_0/2$). The transfer of energy is mainly directed from the long wave to the short ones, feeding their growth. Resonance could possibly occur also between two waves with similar frequency and a vortical mode with zero frequency (Lelong & Riley 1991; Bartello 1995). As predicted by statistical equilibrium analysis, energy is expected to flow from large-scale to small-scale inertia-gravity waves. According to the analysis of Bartello (1995), resonance interactions between three waves are of secondary importance. Ageostrophic energy can instead cascade downscale thanks to the wave-wave-vortex interactions.

Within the context of turbulence theory, triad interactions have historically been the objects of a great deal of modelling efforts (see for instance Leith & Kraichnan 1972). Ohkitani & Kida (1992) carried out the first detailed numerical study of triad interactions in forced isotropic turbulence. Similar analyses were also carried out in the context of two-dimensional turbulence, covering both the enstrophy and the energy ranges (Ohkitani 1990; Maltrud & Vallis 1993; Vallgren 2011). The main question addressed in these studies is whether the transfer of energy is local in wavenumber space. Somewhat surprisingly, all the aforementioned studies showed that turbulence is an intimately non-local process, involving large exchange of energy in triads with two large comparable wavenumbers and one small wavenumber. Despite the high non-locality, energy exchange is mainly between the two large wavenumbers, whereas the small one only acts as a catalyser.

In this paper, we will mainly address two issues. First, we aim at extending some recent results by Vallgren *et al.* (2011), obtained within the framework of the primitive equations, by considering the full Boussinesq system with finite stratification, *i.e.* where there is no hydrostatic balance. The main focus is to understand whether and how the route to dissipation is modified by a finite horizontal Froude number. Comparisons with the primitive equation are made, mainly focusing on energy and enstrophy spectra and fluxes. The simulations we have carried out give a good picture of the dynamics which take place for several Ro and Fr, spanning reasonable values for large scale atmospheric flows. Secondly, we study the possible influence of wave motions in the forward energy cascade. To do this, the full Boussinesq system is the appropriate set of equations. In fact, the primitive equations do not correctly represent wave modes that have a long vertical and a short horizontal wavelength, which have fast frequencies and for which the hydrostatic approximation holds to a smaller degree. Nevertheless, as we will show in the following, the dynamics appear to be very similar in the two cases, indicating that these modes may be of minor importance in the overall dynamics. Frequency analyses of time series from both geostrophically balanced modes and ageostrophic modes are carried out in order to find signatures of wave motions. We also study triad interactions in order to understand which modes contribute the most to the energy transfer towards small scales and whether resonant wave interactions or turbulent-like process are dominant.

The paper is organized as follows: section 2 gives the theoretical background and the formulation of the problem; in section 3 the numerical details and parameters are summarized; in section 4 we present some flow fields in physical space; in section 5, energy spectra and fluxes are presented with comparisons between the primitive equations and the Boussinesq systems; section 6 focuses on analysing wave motions and frequency spectra; in section 7 the transfer of energy among wavenumbers through triad interactions is studied. Conclusions are finally given in Section 8.

2. Theoretical formulation

We start from the inviscid three dimensional Navier-Stokes equations within the Boussinesq approximation in a rotating frame for an incompressible flow,

$$\frac{D\mathbf{u}}{Dt} = -\frac{\nabla p}{\rho_0} - f\mathbf{e}_z \times \mathbf{u} + Nb\mathbf{e}_z, \tag{2a}$$

$$\frac{Db}{Dt} = -Nw, \tag{2b}$$

$$\nabla \cdot \mathbf{u} = 0\,, \tag{2c}$$

where δ_{i3} is the Kronecker's delta, $\mathbf{u}$ is the velocity vector, w is the vertical velocity component, $\mathbf{e}_z$ is the vertical unit vector, p is the pressure, $b = g\rho/(N\rho_0)$ is the rescaled buoyancy, where ρ and ρ_0 are the fluctuating and background densities, respectively. In atmospheric applications, potential density is used in place of ρ (Vallis 2006). The buoyancy is here rescaled in such a way that it has the same dimension as velocity rather than acceleration.

The system (2) is made dimensionless using geostrophic scaling. For geostrophic flows, the horizontal pressure gradient is mainly balanced by the Coriolis force, whereas the vertical pressure gradient is mainly balanced by buoyancy force. Following Charney (1971), the vertical scale is rescaled by

N/f. The following estimates apply:

$$\begin{aligned} &x \sim L, \quad y \sim L, \quad z \sim f/NL, \quad t \sim L/U, \\ &u \sim U, \quad v \sim U, \quad w \sim Ro\, Uf/N, \quad b \sim U. \end{aligned} \tag{3}$$

The system (2) can be rewritten introducing the Charney potential vorticity q and the two ageostrophic components, a_1 and a_2:

$$q = -\frac{\partial u}{\partial y} + \frac{\partial v}{\partial x} + \frac{\partial b}{\partial z}, \tag{4a}$$

$$a_1 = -\frac{\partial v}{\partial z} + \frac{\partial b}{\partial x}, \tag{4b}$$

$$a_2 = \frac{\partial u}{\partial z} + \frac{\partial b}{\partial y}, \tag{4c}$$

where a_1 and a_2 measure the departure from the thermal wind balance (Vallis 2006). The geostrophic scaling for q, a_1 and a_2 reads

$$q \sim U/L, \quad a_1 \sim Ro\, U/L, \quad a_2 \sim Ro\, U/L. \tag{5}$$

Using the definitions (4), we recast (2) into the three prognostic equations

$$\begin{aligned} \frac{\partial q}{\partial t} = &\frac{\partial}{\partial y}\left(\frac{\partial u^2}{\partial x} + \frac{\partial uv}{\partial y} + Ro\frac{\partial uw}{\partial z}\right) - \frac{\partial}{\partial x}\left(\frac{\partial uv}{\partial x} + \frac{\partial v^2}{\partial y} + Ro\frac{\partial vw}{\partial z}\right) \\ &- \frac{\partial}{\partial z}\left(\frac{\partial ub}{\partial x} + \frac{\partial vb}{\partial y} + Ro\frac{\partial wb}{\partial z}\right) + \nu_S \nabla^8 q - \nu_L q, \end{aligned} \tag{6a}$$

$$\begin{aligned} Ro\frac{\partial}{\partial t}\left(a_1 + \frac{Fr^2}{Ro^2}\frac{\partial w}{\partial y}\right) = &\, a_2 - \frac{\partial w}{\partial x} + \frac{\partial}{\partial z}\left(\frac{\partial uv}{\partial x} + \frac{\partial v^2}{\partial y} + Ro\frac{\partial vw}{\partial z}\right) \\ &- \frac{\partial}{\partial x}\left(\frac{\partial ub}{\partial x} + \frac{\partial vb}{\partial y} + Ro\frac{\partial wb}{\partial z}\right) \\ &- \frac{Fr^2}{Ro}\frac{\partial}{\partial y}\left(\frac{\partial uw}{\partial x} + \frac{\partial vw}{\partial y} + Ro\frac{\partial ww}{\partial z}\right) \\ &+ Ro\nu_S \nabla^8 a_1 - Ro\nu_L a_1, \end{aligned} \tag{6b}$$

$$\begin{aligned} Ro\frac{\partial}{\partial t}\left(a_2 - \frac{Fr^2}{Ro^2}\frac{\partial w}{\partial x}\right) = &- a_1 - \frac{\partial w}{\partial y} - \frac{\partial}{\partial z}\left(\frac{\partial u^2}{\partial x} + \frac{\partial uv}{\partial y} + Ro\frac{\partial uw}{\partial z}\right) \\ &- \frac{\partial}{\partial y}\left(\frac{\partial ub}{\partial x} + \frac{\partial vb}{\partial y} + Ro\frac{\partial wb}{\partial z}\right) \\ &+ \frac{Fr^2}{Ro}\frac{\partial}{\partial x}\left(\frac{\partial uw}{\partial x} + \frac{\partial vw}{\partial y} + Ro\frac{\partial ww}{\partial z}\right) \\ &+ Ro\nu_S \nabla^8 a_2 - Ro\nu_L a_2, \end{aligned} \tag{6c}$$

$$0 = \frac{\partial u}{\partial x} + \frac{\partial v}{\partial y} + Ro\frac{\partial w}{\partial z}, \tag{6d}$$

where both a small scale hyperviscosity, associated with a fourth-order Laplacian, and large scale linear drag have been employed in order to provide a mean to dissipate energy at small and large scales. The use of hyperviscosity allows us to reduce the range of small scales at which viscosity plays a dominant role. Large scale friction is needed in order to avoid that an energy condensate develops at large scales as a result of the inverse energy cascade. Note that for simplicity, the set of equations (6) has been derived assuming that there is a large scale and a small scale diffusivity associated with the buoyancy which is equal to the corresponding large scale and small scale viscosity ν_L and ν_S, respectively.

Taking the scalar product of (2a) and $\mathbf{u}$, multiplying (2b) by b, and summing the resulting equations, we can derive the total energy equation in a periodic frame

$$\frac{d}{dt}\int \frac{u^2+v^2+Fr^2w^2+b^2}{2}\,\mathrm{d}x\mathrm{d}y\mathrm{d}z = -\varepsilon, \tag{7}$$

where ε is the sum of the small scale and large scale energy dissipation, ε_S and ε_L, respectively. The total energy of the system is the sum of kinetic energy, $(u^2+v^2+Fr^2w^2)/2$, and potential energy, $b^2/2$.

Equations (6a-6c) constitute a geostrophically scaled version of the Boussinesq system (BQ). In the limit of zero Fr, the primitive equation system (PE) solved by Vallgren *et al.* (2011) is recovered. Applying the geostrophic scaling (3) at the vertical momentum balance (2a) gives

$$Fr^2\frac{Dw}{Dt} = -\frac{\partial p}{\partial z} + b, \tag{8}$$

where

$$\frac{D}{Dt} = \frac{\partial}{\partial t} + u\frac{\partial}{\partial x} + v\frac{\partial}{\partial y} + Ro\, w\frac{\partial}{\partial z}. \tag{9}$$

From equation (8), it is clear that setting Fr to zero is equivalent to applying the hydrostatic assumption (Billant & Chomaz 2001). Interestingly, the potential vorticity equation (6a) does not depend on Fr and therefore has the same expression both in the PE and in the BQ. Neglecting the viscous terms and using the definitions (4), (6a) can be rewritten as

$$\begin{aligned}\frac{Dq}{Dt} =& Ro\left(a_1\frac{\partial b}{\partial y} - a_2\frac{\partial b}{\partial x} + q\frac{\partial w}{\partial z} - \frac{\partial b}{\partial y}\frac{\partial w}{\partial y} - \frac{\partial b}{\partial x}\frac{\partial w}{\partial x} - 2\frac{\partial b}{\partial z}\frac{\partial w}{\partial z}\right)\\ &+Ro^2\left(a_1\frac{\partial w}{\partial x} + a_2\frac{\partial w}{\partial y}\right).\end{aligned} \tag{10}$$

Note that whereas the Ertel potential vorticity (*e.g.* Pedlosky 1987) is a conserved quantity also in PE and BQ, the same does not apply to the Charney potential vorticity which we consider here. However, in the limit $Ro \to 0$, the above expression reduces to

$$\frac{Dq}{Dt} = 0, \tag{11}$$

stating that q is a materially conserved quantity (Charney 1971). In the limit $Ro \to 0$ and $Fr^2/Ro \to 0$, the equations (6b) and (6c) lose their time derivative and reduce to algebraic equations from which the ageostrophic wind may be directly computed from geostrophically balanced fields (see *e.g.* Gill 1982).

Retaining only the linear terms in (6b) and (6c) and using (2c), we can derive the well known wave equation for inertia-gravity waves (Gill 1982; Pedlosky 1987; Vallis 2006). The corresponding dispersion relation reads

$$\omega_d^2 = \frac{k_x^2 + k_y^2 + k_z^2}{Fr^2\left(k_x^2 + k_y^2\right) + Ro^2 k_z^2}. \tag{12}$$

Note that the dimensional counterpart of (12) would read

$$\tilde{\omega}_d^2 = \frac{N^2\left(\tilde{k}_x^2 + \tilde{k}_y^2\right) + f^2\tilde{k}_z^2}{\tilde{k}_x^2 + \tilde{k}_y^2 + \tilde{k}_z^2}, \tag{13}$$

which is the common expression which may be found in any geophysical fluid dynamic book (Gill 1982; Pedlosky 1987; Vallis 2006). The tilde, $\tilde{\cdot}$, now refers to dimensional quantities.

In the limit of zero Fr, the dispersion relation (12) becomes singular for small k_z, *i.e.* for vertically long, barotropic waves. Infinitely fast wave motions may therefore appear in the primitive equations. On the other hand, in the Boussinesq system wave frequencies are bounded between Ro^{-1} and Fr^{-1}, as is clear from equation (12).

The total energy spectrum

$$E(\mathbf{k}) = \frac{\hat{u}(\mathbf{k})\hat{u}^*(\mathbf{k}) + \hat{v}(\mathbf{k})\hat{v}^*(\mathbf{k}) + Fr^2\hat{w}(\mathbf{k})\hat{w}^*(\mathbf{k}) + \hat{b}(\mathbf{k})\hat{b}^*(\mathbf{k})}{2}, \tag{14}$$

decouples into a geostrophic part associated with q and an ageostrophic part associated with a_1 and a_2. We find that

$$E(\mathbf{k}) = \sum_{\mathbf{k}} \frac{\hat{q}(\mathbf{k})\hat{q}^*(\mathbf{k})}{2k^2} + \left\{ \begin{array}{c} \hat{a}_1(\mathbf{k}) \\ \hat{a}_2(\mathbf{k}) \end{array} \right\} \left[\begin{array}{cc} E_{22} & E_{23} \\ E_{23} & E_{33} \end{array} \right] \left\{ \begin{array}{c} \hat{a}_1(\mathbf{k}) \\ \hat{a}_2(\mathbf{k}) \end{array} \right\}^*, \tag{15}$$

where $k = \sqrt{k_x^2 + k_y^2 + k_z^2}$. The energy can therefore be divided into a geostrophic and an ageostrophic part, E_G and E_A, respectively. In Appendix A, the explicit form of the matrix $\mathbf{E}$ is given. Following Bartello (1995), we will now classify the nonlinear interactions involving geostrophic and ageostrophic modes. According to (15), the rate of change of the geostrophic energy, E_G, can be rewritten as

$$\frac{\partial E_G}{\partial t} = \sum_{\mathbf{k}} \frac{1}{2k^2}\left(\frac{\partial \hat{q}(\mathbf{k})}{\partial t}\hat{q}^*(\mathbf{k}) + \frac{\partial \hat{q}^*(\mathbf{k})}{\partial t}\hat{q}(\mathbf{k})\right), \tag{16}$$

where the rate of change of q due to non-linear terms can be separated into three contributions

$$\frac{\partial \hat{q}(\mathbf{k})}{\partial t} = NL_{GG}(\mathbf{k}) + NL_{GA}(\mathbf{k}) + NL_{AA}(\mathbf{k}), \tag{17}$$

with the subscripts standing for the nonlinear terms arising from the interaction of the two classes of motions: geostrophic (G) and ageostrophic (A). Explicitly,

$$NL_{GG}(\mathbf{k}) = \sum_{\substack{\mathbf{p},\mathbf{q} \\ \mathbf{k}=\mathbf{p}+\mathbf{q}}} \Gamma_{GG}(\mathbf{k},\mathbf{p},\mathbf{q})\hat{q}(\mathbf{p})\hat{q}(\mathbf{q}), \tag{18a}$$

$$NL_{GA}(\mathbf{k}) = \sum_{\substack{\mathbf{p},\mathbf{q} \\ \mathbf{k}=\mathbf{p}+\mathbf{q}}} \sum_{i} \Gamma_{GA_i}(\mathbf{k},\mathbf{p},\mathbf{q}) \left[\hat{q}(\mathbf{p})\hat{a}_i(\mathbf{q}) + \hat{a}_i(\mathbf{p})\hat{q}(\mathbf{q})\right], \tag{18b}$$

$$NL_{AA}(\mathbf{k}) = \sum_{\substack{\mathbf{p},\mathbf{q} \\ \mathbf{k}=\mathbf{p}+\mathbf{q}}} \sum_{i,j} \Gamma_{A_jA_i}(\mathbf{k},\mathbf{p},\mathbf{q}) \left[\hat{a}_i(\mathbf{p})\hat{a}_j(\mathbf{q}) + \hat{a}_j(\mathbf{p})\hat{a}_i(\mathbf{q})\right], \tag{18c}$$

where the explicit expression of the coefficients $\Gamma_{i,j}(\mathbf{k},\mathbf{p},\mathbf{q})$ can be found from the nonlinear terms in (6). Multiplying (17) by $\hat{q}^*(\mathbf{k})/2k^2$, we obtain the geostrophic energy budget

$$\frac{\partial E_G(\mathbf{k})}{\partial t} = T_{GGG}(\mathbf{k}) + T_{GGA}(\mathbf{k}) + T_{GAA}(\mathbf{k}), \tag{19}$$

where T_{GGG}, T_{GGA} and T_{GAA} represent the transfers into geostrophic energy due to nonlinear interactions involving two geostrophic, one geostrophic and one ageostrophic and two ageostrophic modes, respectively. In a similar way we arrive at an expression for E_A,

$$\frac{\partial E_A(\mathbf{k})}{\partial t} = T_{AGG}(\mathbf{k}) + T_{AGA}(\mathbf{k}) + T_{AAA}(\mathbf{k}). \tag{20}$$

The transfer functions satisfy the following conservation relations

$$\begin{aligned} \sum_{\mathbf{k}} T_{GGG}(\mathbf{k}) &= 0, \\ \sum_{\mathbf{k}} T_{GGA}(\mathbf{k}) + T_{AGG}(\mathbf{k}) &= 0, \\ \sum_{\mathbf{k}} T_{AGA}(\mathbf{k}) + T_{GAA}(\mathbf{k}) &= 0, \\ \sum_{\mathbf{k}} T_{AAA}(\mathbf{k}) &= 0, \\ \sum_{\mathbf{k}} k^2 T_{GGG}(\mathbf{k}) &= 0, \end{aligned} \tag{21}$$

where the last relation is an expression of the fact that potential enstrophy is conserved by interaction involving only geostrophic modes. From the energy transfer functions, it is also straightforward to define the enstrophy transfer functions. Since the enstrophy spectrum is given by

$$Q(\mathbf{k}) = \frac{\hat{q}(\mathbf{k})\hat{q}^*(\mathbf{k})}{2}, \tag{22}$$

the enstrophy transfer functions can easily be found from (19) as

$$T^{\eta}_{GGG}(\mathbf{k}) = k^2 T_{GGG}(\mathbf{k}), \qquad T^{\eta}_{GGA}(\mathbf{k}) = k^2 T_{GGA}, (\mathbf{k})$$

$$T^{\eta}_{GAA}(\mathbf{k}) = k^2 T_{GAA}(\mathbf{k}). \tag{23}$$

The transfer functions give information about the amount of energy/enstrophy flowing into or out of a certain mode. Nevertheless, they do not preserve the information about where such energy comes from and which wavenumbers are involved in the exchange. In order to shed some lights on the dynamics physical process, such kind of information is however crucial. Therefore we will also consider the triad interaction terms as functions of $k = |\mathbf{k}|$, $p = |\mathbf{p}|$ and $q = |\mathbf{q}|$. For example, we denote by $T_{GGG}(k,p,q)$ the transfer function which is calculated by averaging the relevant triad interactions over k, p and q. Note that according to the definitions, such transfer functions are symmetric with respect to p and q.

The energy/enstrophy flux

$$\Pi(k) = -\sum_{|\mathbf{k}|=0}^{|\mathbf{k}|=k} T(\mathbf{k}) \qquad \text{and} \qquad \Pi^{\eta}(k) = -\sum_{|\mathbf{k}|=0}^{|\mathbf{k}|=k} T^{\eta}(\mathbf{k}) \tag{24}$$

are often used in place of their generic transfer function $T(\mathbf{k})$ and $T^{\eta}(\mathbf{k})$. It is therefore quite natural to classify the fluxes in a similar manner as done for the transfer terms. In particular, a special attention will be paid to the energy and enstrophy fluxes due to the geostrophic interactions only,

$$\Pi_G(k) = -\sum_{|\mathbf{k}|=0}^{|\mathbf{k}|=k} T_{GGG}(\mathbf{k}) \quad \text{and} \quad \Pi^{\eta}_G(k) = -\sum_{|\mathbf{k}|=0}^{|\mathbf{k}|=k} T^{\eta}_{GGG}(\mathbf{k}). \tag{25}$$

3. Simulations

3.1. *Numerical methodology*

The system (6) is discretized in a triply-periodic isotropic domain, allowing for Fourier representation of the variables in all the three spatial directions. Observe that the box is cubic in a space where the vertical coordinate is stretched by a factor of N/f. A pseudo-spectral method is used, providing an exponential convergence of the numerical solution. Nonlinear terms in the equations (6) are advanced in time using a low-storage fourth-order Runge-Kutta scheme. Linear terms are instead separately solved using an exact implicit procedure (Canuto *et al.* 1988). In order to prevent aliasing errors, the 2/3-dealiasing rule was applied to nonlinear terms (6).

Velocities and buoyancy are recovered from q, a_1 and a_2, using the following inversion relations:

$$\nabla^2 b = \frac{\partial q}{\partial z} + Ro\left(\frac{\partial a_1}{\partial x} + \frac{\partial a_2}{\partial y}\right), \tag{26a}$$

$$\frac{\partial u}{\partial z} = -\frac{\partial b}{\partial y} + Ro a_2, \tag{26b}$$

$$\frac{\partial v}{\partial z} = \frac{\partial b}{\partial x} - Ro a_1, \tag{26c}$$

$$\frac{\partial^2 w}{\partial^2 z} = \frac{\partial a_1}{\partial y} - \frac{\partial a_2}{\partial x}. \tag{26d}$$

However, for $k_z = 0$, the inversion relations (26) becomes singular and, as shown by (4b) and (4c), a_1 and a_2 are not independent, *i.e.* $a_{1,y} = a_{2,x}$. For the mode $k_z = 0$ we instead solve for q, w and b, using the equations (6a), (8) and (2b), respectively. The horizontal velocity components can then be recovered from the potential vorticity inversion

$$\nabla^2 \mathbf{u}_h = -\nabla \times q\mathbf{e}_z, \tag{27}$$

whereas a_1 and a_2 are calculated from their definitions, (4b) and (4c), respectively.

A random forcing is introduced in the potential vorticity equation only, *i.e.* no ageostrophic motions are directly forced. The forcing scheme is the same as used by Vallgren & Lindborg (2011). The scheme is white noise in time, so that no particular time scale is forced. The forcing is perfectly decorrelated to the velocity field, allowing us to exactly control the enstrophy and the energy injection rates into the system. The enstrophy injection rate, η, is set to unity in all the simulations, which means that we can regard time as non-dimensionalised using $\eta^{1/3}$. The forcing is isotropic in the vertically-stretched space and is applied to large scales only, corresponding to the wavenumber band $k \in [3\,,\,5]$. The forcing has a Gaussian distribution over this range. The simulations are initialized with random flow fields and they are run long enough for a steady energy cascade to develop.

To allow for very high resolution simulations, the numerical code was parallelized with the use of Message Passing Interface (MPI) and run on up to 4096 processors, resulting in a linear scalability. Inviscid energy conservation tests, equation (7), have been carried out without applying any forcing and providing an increasing conservation of energy up to machine precision as time step was progressively reduced. In the limit of zero *Ro*, results in agreement with quasi-geostrophic numerical simulations (Vallgren & Lindborg 2011) were obtained.

3.2. *Choice of the numerical parameters*

The numerical and physical parameters used in the simulations are listed in table 1. The box is chosen as $(L_x \times L_y \times L_z) = (2\pi \times 2\pi \times 2\pi)$, using 1024 modes in each direction. The physical parameters in table 1 were extracted from the simulations after that a steady direct energy cascade was obtained. The values of *Ro* and *Fr* were chosen to span a realistic range representative for atmospheric applications. Boer & Shepherd (1983) estimated the enstrophy flux from global FGGE data, giving a value on the order of $10^{-15}\,s^{-3}$. Cho & Lindborg (2001) made a similar estimate using the third order structure functions measured in the lower stratosphere. Such a value gives a Rossby number, $Ro = \eta^{1/3}/f$, on the order of 0.1 for mid-latitude dynamics. A realistic value of N is on the order of $10^{-2}s^{-2}$ (Vallis 2006), corresponding to a ratio, f/N, of about 0.01. With the aim of reproducing dynamics representative of

run	Ro	Fr	ν_L	$\nu_S \cdot 10^{18}$	ε_L/P	ε_S/P	Δt^{TS}	T^{TS}
PE2	0.2	0	0.012	6.2	0.30	0.36	-	-
PE1	0.1	0	0.012	4.0	0.43	0.14	-	-
PE05	0.05	0	0.012	4.0	0.46	0.05	-	-
PE025	0.025	0	0.012	4.0	0.25	$7.5 \cdot 10^{-3}$	-	-
PE0	0	0	0.012	4.0	0.43	$5.4 \cdot 10^{-4}$	-	-
aBQ2	0.2	0.01	0.012	6.2	0.43	0.27	-	-
aBQ1	0.1	0.01	0.012	4.0	0.76	0.08	-	-
aBQ05	0.05	0.01	0.012	4.0	0.70	$5.9 \cdot 10^{-3}$	-	-
bBQ001	0.1	0.001	0.012	6.2	0.72	0.086	$1.4 \cdot 10^{-3}$	3.20
bBQ01	0.1	0.01	0.012	4.0	0.76	0.08	$1.9 \cdot 10^{-2}$	18.3
bBQ1	0.1	0.1	0.012	4.0	0.86	0.064	$1.8 \cdot 10^{-2}$	20.3
ST	-	-	0.012	20	0.06	0.90	-	-

TABLE 1. Summary of the simulations. The physical parameters have been calculated after a steady direct cascade was established. Large and small scale dissipation have been made dimensionless with respect to the energy injection rate P. Note that for most of the runs, energy was still growing due to the inverse cascade.

the atmosphere, we have carried out simulations with $f/N = Fr/Ro \in [0\,,\,1]$. As shown by Vallgren *et al.* (2011), in the limit of zero Fr, an increasing amount of energy cascades towards small scales as Ro is increased. Therefore, in order to keep the dissipation range well-resolved, the small-scale viscosity has to be somewhat increased with increasing Ro.

We divide the simulations into four sets called PE, aBQ, bBQ and dBQ. Each run is named accordingly, followed by a number x. In the PE simulations, Fr is set to zero and x refers to the Rossby number which is varied between 0 and 0.2. In the aBQ runs, Fr is set to 0.01 and the Rossby number, indicated by the suffix x, is varied in the same way as in the PE set. In the bBQ, Ro is instead kept fixed to 0.1, whereas the Froude number, indicated by x, is varied from 0.001 to 0.1. Finally, a non-rotating simulation of the primitive equations has also been run and named ST in order to investigate the vertical spectrum, as discussed in the section 5. In order to investigate the role of gravity waves and inertial waves, time series of individual Fourier modes are collected for the bBQ set after that a forward cascade is established. The sampling time step Δt^{TS} and the covered time interval T^{TS} are given in table 1.

4. Flow fields

We start by presenting some snapshots from the simulations in order to give a feeling of the physical process that we investigate. In figure 1 (*left*), a horizontal cut of the potential vorticity flow field is shown for the aBQ1 run, *i.e.* $Ro = 0.1$ and $Fr = 0.01$. The overall dynamics at large scales resemble the QG dynamics (see for instance fig. 9 of Vallgren & Lindborg 2010) with a large scale vortex surrounded by small-scale filaments. Figure 1 (*middle*) displays a vertical cut of the large-scale vortex. Interestingly, this structure shows a large degree of coherence in the vertical direction, displaying similarities with the large scales vortices found by Vallgren & Lindborg (2010) and the related barotropization of the flow. Nevertheless, some differences can also be observed. Unlike the QG simulation results, the core of the vortex is dominated by small scale structures which can be observed both in the horizontal and in the vertical cuts. Moreover, patches of small scale turbulence can also be observed all over the flow. A particularly intense small-scale chaotic region is found in the top right corner of the horizontal potential vorticity cut in figure 1 (*left*). As shown by the horizontal cut of a_2 in figure 1 (*right*), in such a region the ageostrophic motions become more intense than in other regions, increasing of about one order of magnitude.

Molemaker *et al.* (2010) reported snapshots of their non-hydrostatic non-geostrophic forced Eady flow, where characteristic structures of QG dynamics as filaments and small scales three-dimensional turbulence were both observed. They argued that a forward energy cascade is needed for the system to reach a balanced state when a constant energy input is introduced into the flow. They showed that dissipative turbulent patches arise as the result of instabilities developing along potential vorticity fronts. The horizontal and vertical structures of the turbulent patches in figure 1 (*left*) and 1 (*middle*) are illustrated in the close-up shown in figure 2, where both the potential vorticity field and the local vertical Froude number, defined as

$$Fr_L = \frac{\sqrt{\omega_x^2 + \omega_y^2}}{2N}, \tag{28}$$

are shown in an horizontal (parallel to the x-direction) and vertical plane. In (28), ω_x and ω_y represent the dimensional horizontal vorticities. In the horizontal plane, the potential vorticity and Fr_L, show small-scale structures which follow very similar patterns. More importantly, Fr_L attains values of the order of unity, which is required for KH instabilities to develop (Billant & Chomaz 2001). Also in the vertical plane, very similar observations can be made. It is also worth noticing how confined are the structures in the vertical direction as compared to the horizontal direction (bottom panels in figure 2).

5. Energy spectra and spectral fluxes

5.1. *Horizontal spectra*

Simulations were run long enough to allow for the formation of a steady down-scale energy cascade with a nearly constant small scale dissipation. Figure 3 (*left*) shows the time evolution of both kinetic and potential energy in the run PE1. Qualitatively, the same picture were obtained in all the other runs. To start with, the kinetic energy grows twice as fast as the potential energy, as an effect of the Charney isotropic forcing (Vallgren & Lindborg 2010). However,

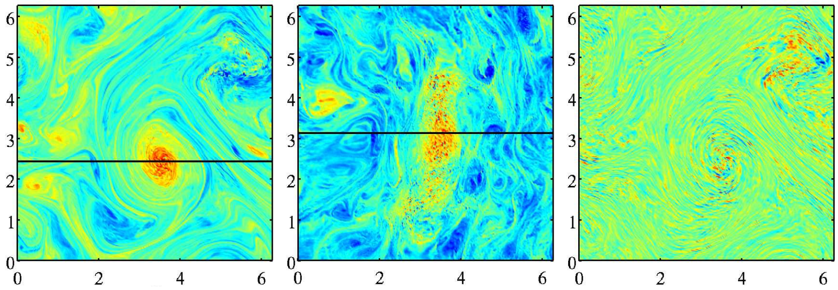

FIGURE 1. Potential vorticity q (*left* and *middle*) and the second ageostrophic component a_2 (*right*) cuts. (*left*) and (*right*) horizontal cuts at $z = 3.14$; (*middle*) vertical cut at $y = 2.4$, corresponding to the location of the large scale vortex. Dark helping lines show the position of the vertical and horizontal cut planes.

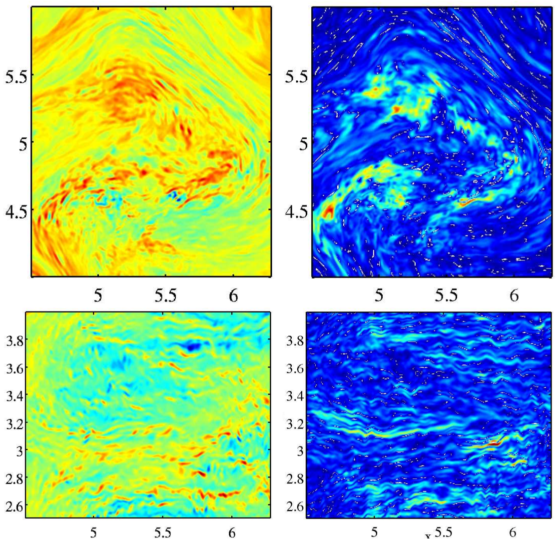

FIGURE 2. Close-up of the turbulent patch in the top right corner of figure 1. (*left*) potential vorticity and (*right*) local Froude number Fr_L. Both the horizontal (*top*) and the vertical (*bottom*) cuts are shown. The colourmap of the local Froude number ranges from 0 (blue) to 1.8 (red).

whereas potential energy saturates quickly at very early stages, kinetic energy continues to increase and levels off only at a later stage. In the quasi-steady state, there is considerably more kinetic energy than potential energy. Similar results were also obtained by Vallgren & Lindborg (2011) in quasi-geostrophic

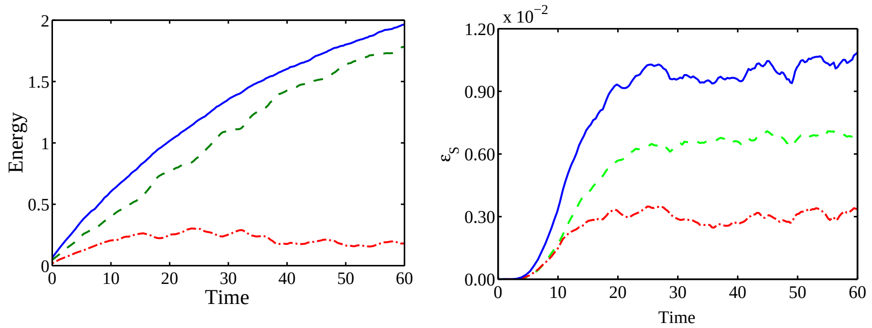

FIGURE 3. Time evolution for the energy (*left*) and the energy dissipation (*right*) for the PE1 run. ——— total; - - - kinetic; −·− potential. Time is made dimensionless with the enstrophy injection rate η. Energy is made dimensionless with $\eta^{2/3}/k_0^2$.

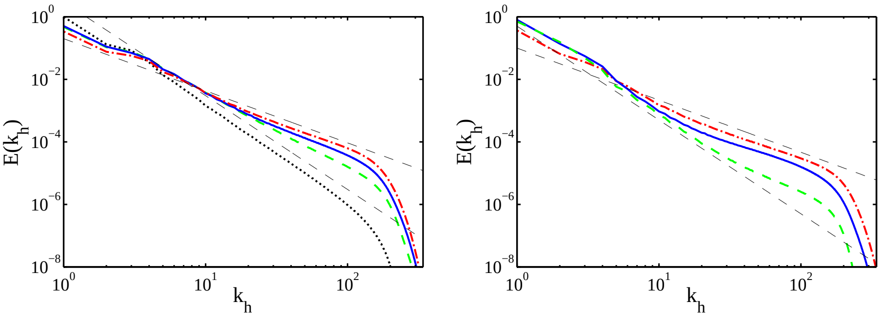

FIGURE 4. Comparison of the two-dimensional horizontal total energy spectra for PE (*left*) and aBQ (*right*) runs for several *Ro* numbers. −·− $Ro = 0.2$;——— $Ro = 0.1$;- - - $Ro = 0.05$;········ $Ro = 0.0$ (only PE runs). In ——— (thin) helping lines with $k_h^{-5/3}$ and k_h^{-3}.

simulations. However, kinetic energy tends to level off at earlier times as *Ro* is increased. In spite of the fact that the kinetic energy is still growing, small-scale dissipation attains nearly constant values rather soon, at times comparable to the time required by the potential energy to saturate. The kinetic energy dissipation is observed to be larger than potential energy dissipation.

We begin by examining the horizontal two-dimensional energy spectra, shown in figure 4, both for the PE (*left*) and aBQ (*right*) sets. The spectra were calculated by averaging over circles with constant $k_h = \sqrt{k_x^2 + k_y^2}$. The curves in figure 4 (*left*) compare well with the results of Vallgren *et al.* (2011), who studied the one-dimensional horizontal spectra. Consistent with the results of Vallgren *et al.* (2011), the spectra at low *Ro* scale as k_h^{-3} for a large

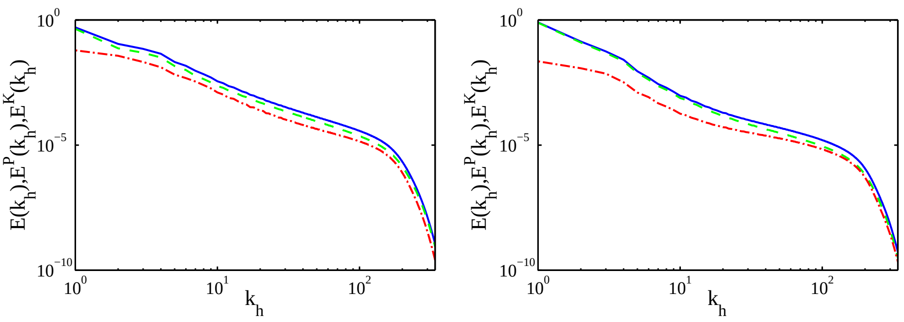

FIGURE 5. Kinetic and potential energy spectra for the PE (*left*) and aBQ (*right*) runs with $Ro = 0.1$. ——— total energy; - - - kinetic energy; —·— potential energy.

span of wavenumbers. As Ro is increased, departures from the k_h^{-3} dependence are observed, and the slopes are close to $-5/3$ at small scales. This is a direct consequence of the increasing amount of energy which cascades downscale. Even though a qualitatively similar behaviour can be observed in the left and right panels, it should be noted that there are smaller departures from the quasi-geostrophic curves in the BQ runs as compared to the PE runs at the same Rossby number.

As shown by figure 5, at large scales kinetic energy dominates over the potential energy and it accounts almost completely for the total energy content. Similar results were also found in numerical simulations of the QG equation (Vallgren & Lindborg 2011). However, it should also be noted that the gap between kinetic and potential energy tends to increase in the BQ runs as compared to the PE runs and equipartition occurs only at small scales.

Since the results of the PE and BQ simulations are qualitatively very similar as Ro is changed, henceforth in this section we focus only on PE runs. Results from BQx runs do not differ qualitatively, and analogous conclusions would therefore apply. A question yet to be answered regarding the atmospheric energy spectrum and its transition from k_h^{-3} to $k_h^{-5/3}$ at scales of about 500 km concerns the importance of geostrophic (rotational) and ageostrophic (divergent) motions. Following Lelong & Riley (1991), we rewrite the velocity as

$$\mathbf{u} = \mathbf{e}_z \times \nabla_h \psi + \{\nabla_h \phi + w\mathbf{e}_z\}, \tag{29}$$

where the first term is horizontally non-divergent whereas the second carries all the horizontal divergence of the field. The first term in (29) is associated with the potential vorticity whereas the second term is associated with the ageostrophic components a_1 and a_2. In the QG limit, the divergent part vanishes due to the incompressibility condition (2c). At large scales, where QG is a good approximation, the rotational part should therefore be dominant. Lindborg (2007) calculated the rotational and divergent energy spectra from measurements in the upper troposphere and lower stratosphere and found that rotational modes are totally dominant at synoptic scales but the contributions from the two types of modes are of the same order of magnitude at mesoscales. Lindborg & Brethouwer (2007) found that energy is equipartitioned between rotational and divergent modes in the turbulent cascade of strongly stratified flows. In figure 6 (*left*), the kinetic energy spectrum is shown together with the rotational and divergent contributions. At large scales, the rotational part dominates, whereas the divergent part is several orders of magnitude smaller. The rotational spectrum scales as k_h^{-3} in this range. On the other hand, the divergent energy spectrum is rather flat, a little shallower than $k_h^{-5/3}$. Owing to the different slopes, rotational and divergent energy spectra are doomed to meet at a transition wavenumber k_{tr}. As this scale is approached, the rotational spectrum shallows whereas the divergent spectrum steepens slightly and both tend to $\sim k_h^{-5/3}$. For higher wavenumbers, the energy content in rotational and divergent modes is of the same order of magnitude, consistent with the results on stratified turbulence of Lindborg & Brethouwer (2007) and Lindborg (2007).

Setting $Ro = 0$ and $Fr = 0$ in equations (6b) and (6c), one may derive the so called Ω-equation for the vertical velocity (*e.g.* Gill 1982),

$$\nabla^2 w = -\frac{\partial^2}{\partial y \partial z}\left(\frac{\partial u^2}{\partial x} + \frac{\partial uv}{\partial y}\right) + \frac{\partial^2}{\partial x \partial z}\left(\frac{\partial uv}{\partial x} + \frac{\partial v^2}{\partial y}\right) - \left(\frac{\partial^2}{\partial x^2} + \frac{\partial^2}{\partial y^2}\right)\left(\frac{\partial ub}{\partial x} + \frac{\partial vb}{\partial y}\right). \tag{30}$$

An interesting question is whether the divergent spectrum which is obtained by solving the Ω-equation is comparable to the total divergent spectrum. In figure 6 (*left*) we investigate this. The divergent spectrum which is obtained from (30) is several orders of magnitude smaller than the total divergent spectrum. This clearly shows that the transition from $\sim k_h^{-3}$ to $\sim k_h^{-5/3}$ cannot be explained within a higher order QG model.

The Rossby number dependence of the divergent energy spectrum is investigated in figure 6 (*right*). As is clear from the plot, an increase of Ro leads to a larger amount of divergent energy. It can be argued that this energy is directly linked to the forward energy cascade whose strength increases with Ro. Note that for small Ro the slopes are somewhat shallower than $-5/3$ at small wavenumbers but tend to steepen with increasing wave number.

5.2. *Vertical spectra*

We now turn to the vertical spectra, shown in fig 7. In a similar way as the horizontal spectra, the vertical spectra display many similarities between PE and BQ runs as Ro is increased. In QG dynamics, the vertical spectrum has a similar form, $\sim \eta^{2/3} k_z^{-3}$, as the horizontal spectrum. In the current simulations, the slopes are found to increase with Ro from -3 to $-5/3$. We find it somewhat surprising that the vertical spectra also show such a transition. In contrast to this result, the vertical spectra of strongly stratified turbulence

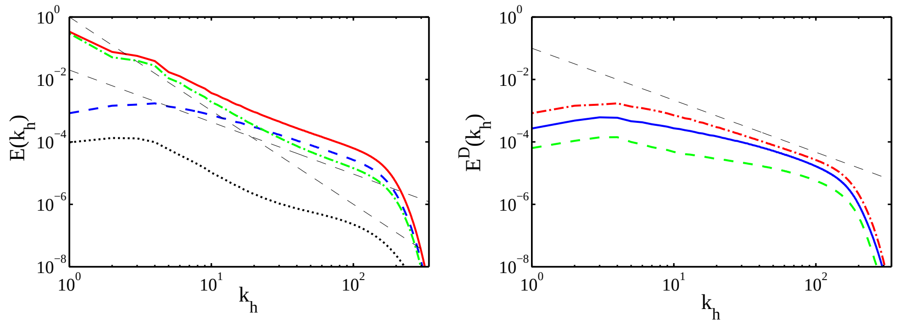

FIGURE 6. (*left*) Divergent (– – –) and rotational (–·–) part of the kinetic energy (——) for the PE02 run. The QG divergent energy, given by (30), is shown as well for reference (········). In – – –(thin) helping lines with $k_h^{-5/3}$ and k_h^{-3}. (*right*) Divergent energy for several *Ro* for the PE runs. –·– $Ro = 0.2$;—— $Ro = 0.1$;– – – $Ro = 0.05$. In – – –(thin) helping lines with $k_h^{-5/3}$.

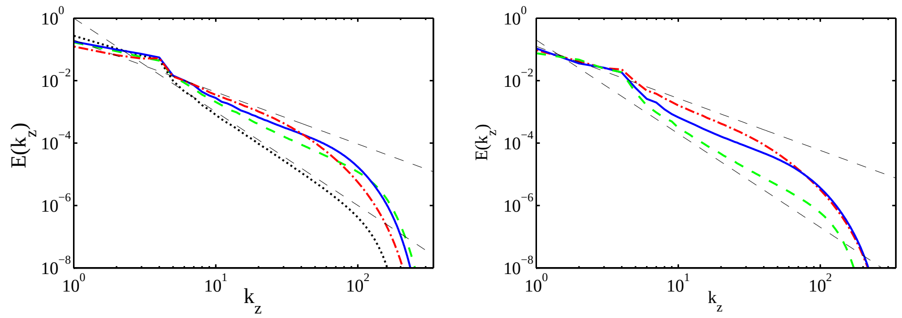

FIGURE 7. Comparison of the one-dimensional vertical total energy spectra for PE (*left*) and aBQ (*right*) runs for several *Ro* numbers. –·– $Ro = 0.2$;—— $Ro = 0.1$;– – – $Ro = 0.05$;········ $Ro = 0.0$ (only PE runs). In – – –(thin) helping lines with $k_h^{-5/3}$ and k_h^{-3}.

which is not affected by system rotation is expected to scale as k_z^{-3} (Billant & Chomaz 2001). In order to investigate if this is the case, we carried out an additional simulation where the linear terms pertaining to the Coriolis forces in equation (2) are set to zero. Setting *Ro* to unity in (3) allows us to retrieve the scaling for strongly stratified flows suggested by Billant & Chomaz (2001). Hydrostasy was assumed in the vertical by imposing Fr equal to zero. In figure 8 (*left*) the vertical spectrum for this simulation is shown together with the vertical spectrum pertaining to the PE01 run. In agreement with previous

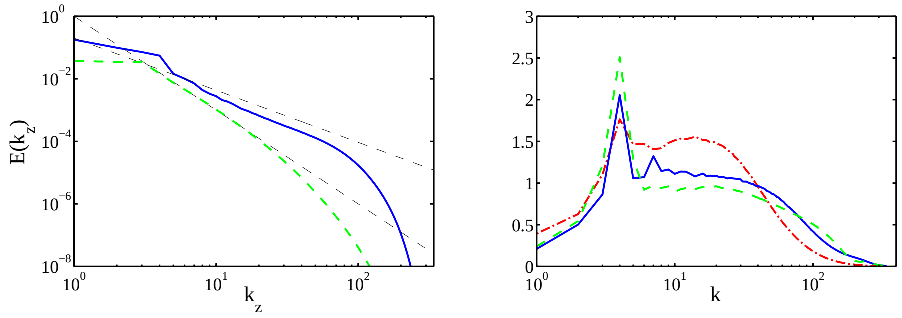

FIGURE 8. (*left*) Comparison of vertical spectra for primitive equations with rotation $Ro = 0.1$ (——) and without rotation (- - -). (*right*) Measure of the Charney isotropy according to (32) for several Ro for the aBQ runs. $-\cdot-$ $Ro = 0.2$;—— $Ro = 0.1$;- - - $Ro = 0.05$.

studies in the field of stratified turbulence, a spectrum of the form

$$E(\tilde{k}_z) = CN^2\tilde{k}_z^{-3} \tag{31}$$

is recovered, with $C \approx 1$. Here $\tilde{k}_z$ is the dimensional vertical wavenumber. This result suggests that the shallowing of the vertical spectrum is an effect of the system rotation.

Vallgren & Lindborg (2011) tested the validity of Charney isotropy (Charney 1971) in high-resolution numerical simulations of QG turbulence. They found that the ratio between the one-dimensional vertical spectrum and the corresponding horizontal spectrum

$$R(k) = \frac{E_z(k)}{E_h(k)}, \tag{32}$$

is approximately equal to unity, except at the forcing and dissipating scales. In equation (32), $E_h(k)$ is the one-dimensional horizontal spectrum and $E_z(k)$ is the one-dimensional vertical spectrum, where k in the vertical spectrum is the vertical wavenumber stretched by a factor of f/N. As Ro is increased, Charney isotropy is expected to apply to a smaller degree. In figure 8 (*right*), $R(k)$ is plotted for several Ro. In all the cases, a plateau is observed at relatively large scales. Its width however reduces with Ro, whereas its amplitude increase approximately linearly with Ro.

5.3. *Energy and enstrophy fluxes*

Vallgren *et al.* (2011) showed that within the primitive equations framework, the amount of energy cascading towards small scales is a function of Ro. In particular, they found that the small scale dissipation scaled as $\varepsilon_S \sim Ro^{3/2}\,P$, where P is the energy injection. Here, we extend their analysis and investigate the influence of a finite Fr. The total energy flux (24) is plotted in figure 9

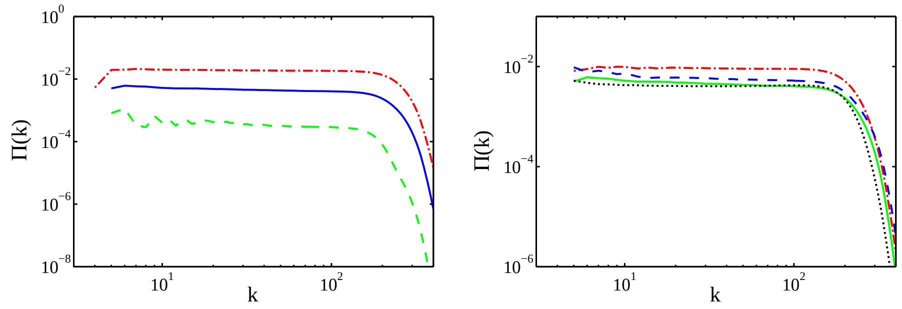

FIGURE 9. Total energy flux function of the wavenumber k for aBQ (*left*) and bBQ (*right*) runs. (*left*) $-\cdot-$ $Ro = 0.2$; —— $Ro = 0.1$; $---$ $Ro = 0.05$. (*right*) $-\cdot-$ $Fr = 0$; $---$ $Fr = 0.001$; —— $Fr = 0.01$; ······· $Fr = 0.1$.

(*left*) for the aBQx runs. In agreement with the observations of Vallgren *et al.* (2011), the amount of energy cascading towards small scales increases with Ro. Notwithstanding, the quantitative magnitude and the Ro-dependence are different. In figure 10 the small-scale dissipation ε_S is shown both for PE and BQ, spanning values of Ro between 0.025 and 0.2. The QG energy flux is found to be several order of magnitude smaller (Vallgren *et al.* 2011). As can be clearly seen, finite stratification and the departure from the hydrostatic approximation lead to somewhat smaller energy fluxes towards small scales. This is also confirmed in figure 5, where a larger amount of kinetic energy is found at large scales. For large Ro, the difference between PE and BQ is relatively small. In particular, at $Ro = 0.2$, the hydrostatic approximation leads to an increase of dissipation of roughly 30%. On the other hand, larger differences, of about one order of magnitude, are found at smaller Ro. However, it is worth pointing out that Fr was kept constant to 0.01 in the aBQ runs. When $Ro \sim Fr$, the primitive equations are not expected to be a good approximation of the dynamics, as seen from equations (6b) and (6c).

The convergence of the BQ to the PE for Fr approaching zero is illustrated in figure 9 (*right*) where the energy flux for the bBQ runs is shown. The Rossby number is kept fix to 0.1, whereas Fr is varied from 0.001 to 0.1. The PE limit is plotted as well, for reference. The fact that an increased degree of stratification leads to a larger energy flux towards small scales seems inconsistent with the idea that stratification suppresses the vertical velocity and increases the two-dimensionality of the system, which according to several studies, *e.g.* Lilly (1983), should lead to an inverse cascade of energy. However, this result is in agreement with a number of recent studies on stratified turbulence (Riley & deBruynKops 2003; Lindborg 2006; Brethouwer *et al.* 2007), showing that stratification favours a downscale energy cascade. It should be noted, however, that the Froude number dependence of the energy flux is weak as compared to the Rossby number dependence, as seen in figure 9.

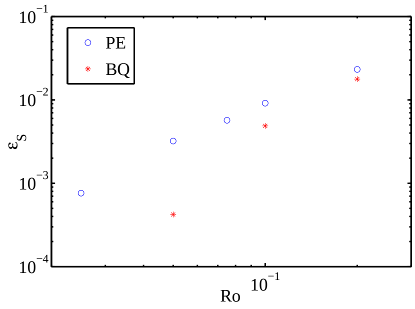

FIGURE 10. Small scale dissipation function of the Ro, both for PE (○) and aBQ (●) runs. For the aBQ runs the Fr number has been kept constant and equal to 0.01.

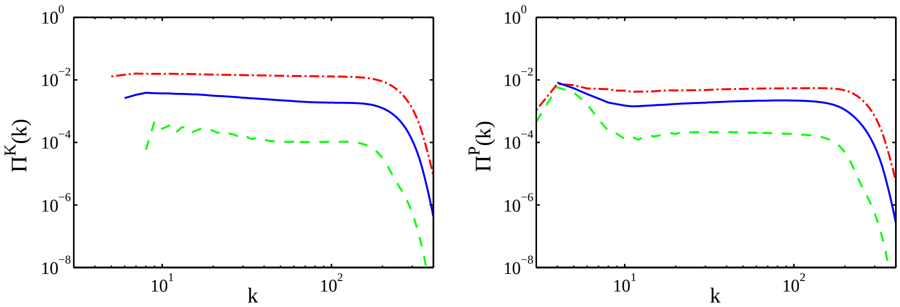

FIGURE 11. Kinetic (*left*) and potential (*right*) energy flux function of the wavenumber k for aBQ runs. –·– Ro = 0.2;—— $Ro = 0.1$;- - - $Ro = 0.05$.

Figure 11 shows the spectral flux of potential and kinetic energy, respectively, for the aBQx runs. Note that separate fluxes do not attain constant values to the same degree as the total flux shown in figure 9. This implies that there is a kinetic to potential energy transfer. In figure 12, the transfer of energy from kinetic to potential energy

$$T^{KP}(k) = -\sum_{|\mathbf{k}|=k} Re\left(\widehat{w}\widehat{b}^*\right) \tag{33}$$

is shown. At large scales there is a net transfer from potential to kinetic energy (dotted lines being the negative part), as is also seen in figure 11. This is consistent with atmospheric dynamics where energy at large scales is fed by the baroclinic instability which converts potential energy to kinetic energy. Interestingly, this transfer do not depend on Ro. However, at smaller scales, the transfer changes sign which means that there is a net transfer from kinetic energy to potential energy. This is also seen in figure 11 (*right*), where, within

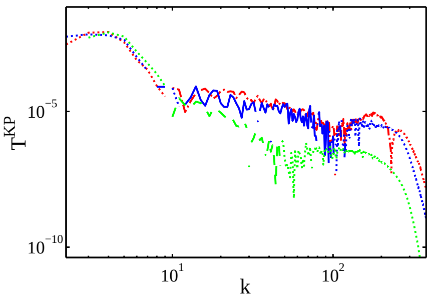

FIGURE 12. Kinetic to potential buoyancy energy transfer given by (33). For the positive part: $-\cdot-$ $Ro = 0.2$;—— $Ro = 0.1$;- - - $Ro = 0.05$. Negative part in dotted lines for all the curves.

the turbulent forward cascade, Π^P is seen to slightly increase. This result is in agreement with the numerical simulations of Molemaker *et al.* (2010).

In order to better understand the role of ageostrophic motions, we separate the contribution of purely geostrophic motions from the total energy flux. In figure 13 (*left*), the geostrophic energy flux is shown together with its complement to the total flux, $\Pi - \Pi_G$. The geostrophic energy flux attains negative values over the whole range, with large contributions only at large scales. Here, it accounts for almost the entire flux, with its complement being one order of magnitude smaller and positive. Clearly, geostrophic interactions support the inverse cascade, whereas ageostrophic motions allow for a drain of energy downscale. At wavenumbers larger than 10, the geostrophic flux becomes negligible and its complement $\Pi - \Pi_G$ accounts for the entire downscale energy transfer. A further decomposition of the complement energy flux to the geostrophic energy flux, $\Pi - \Pi_G$, shows that its dominant contribution is from the interactions between two ageostrophic modes and one geostrophic mode.

Similar conclusions apply also to the potential enstrophy fluxes which are shown in figure 13 (*right*). In QG turbulence, potential enstrophy is a conserved quantity. Unlike energy, it cascades downscale and is finally dissipated at small scales where viscosity dominates. However, within the framework of the primitive equations and the Boussinesq system it is not a conserved quantity and therefore its flux, Π^η, does not generally go to zero as $k \to \infty$. Nevertheless, the geostrophic counterpart of the potential enstrophy flux, Π^η_G, goes to zero, as shown by the conservation relations (21). At large scales, the geostrophic potential enstrophy flux is the dominant contribution and attains a value of the order of unity, showing that the injected enstrophy cascades downscale. The complement to the total potential enstrophy flux is two orders of magnitude smaller in this range, but increases with wavenumbers. At the transition wavenumber, it attains values as large as the geostrophic part. At these scales, departures from the QG prediction can be observed also for the geostrophic

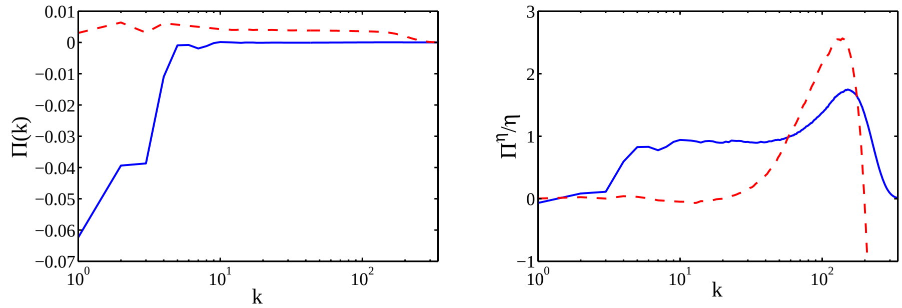

FIGURE 13. (*left*) Geostrophic energy flux Π_G (———) and its complement to the total energy flux $\Pi - \Pi_G$ (- - -) for the bBQ1 run. (*right*) Geostrophic enstrophy flux Π_G^η (———) and its complement to the total enstrophy flux $\Pi^\eta - \Pi_G^\eta$ (- - -) for the bBQ1 run.

counterpart which shows a small bump located at large wavenumbers. Nevertheless, its magnitude stays on the order of unity.

A major finding of this study is that at finite but small Ro and Fr the forward enstrophy cascade and the forward energy cascade may coexist in the same range of scales. This is clearly shown in figure 14 where the total potential enstrophy flux (dashed lines) and the total energy flux (solid lines) are shown together for the aBQ05 and aBQ1 runs. This is remarkably true for the lower Ro where both fluxes attain constant values for the whole span of scales. Nevertheless, whereas all the enstrophy cascades downscale, only a small portion of energy cascades towards small scales, the rest being transferred up-scale in the inverse energy cascade. It is worth noticing that despite the fact that there is a reasonably clean enstrophy downscale cascade, energy spectra deviates from the QG limit, as shown by figure 4.

6. Wave motions

We now investigate the role of inertia-gravity waves in the dynamics. Due to the singularity which is present for barotropic modes in the PE, only runs from the BQ will be considered in the following. It should be pointed out that the random forcing we introduce in the flow excites gravity waves, since all the frequencies are forced. The waves are, however, not directly forced since the forcing is only applied to the potential vorticity equation. The excitement of gravity waves at the forcing scale is crucial in order to be able to investigate the possible role of gravity waves in the downscale energy cascade.

The wave motions are studied through frequency analyses. Due to storage limitations together with the high resolutions employed, time series of only a limited number of spectral components were collected. A logarithmically spaced span of 40 wavenumbers between 1 and 330 were considered both in the

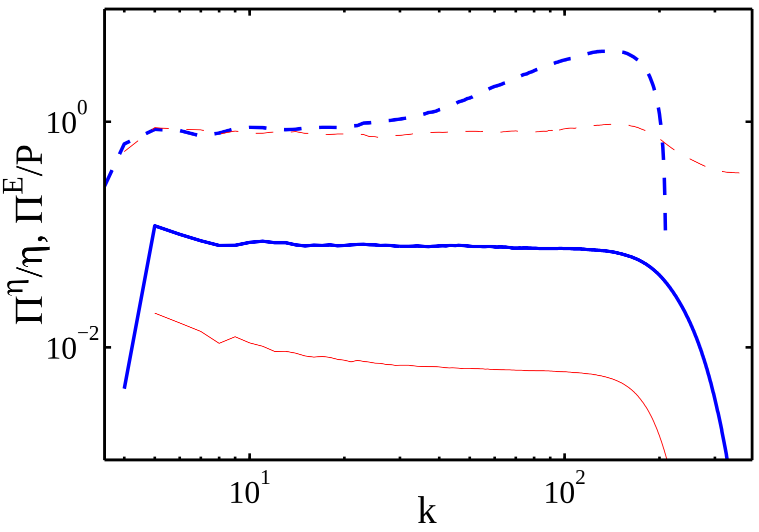

FIGURE 14. Energy (———) and enstrophy (- - -) fluxes scaled with the enstrophy and energy injection rates as a function of the wavenumber k for the aBQ runs with $Ro = 0.1$ (thick lines) and $Ro = 0.05$ (thin lines). Constant enstrophy and energy fluxes can be observed over the same range of wavenumbers.

horizontal and in the vertical direction. In each horizontal circle, 15 equally-spaced wavenumbers were collected. Frequency spectra were computed from time series collected from each individual mode and the spectra were averaged over the horizontal circles. From (12), it is easy to see that wave frequencies can just lie between Ro^{-1} and Fr^{-1}. Therefore, if one aims at resolving all the possible waves, time resolutions of at least $\pi\, Fr$ as well as time spans of $4\,\pi\, Ro$ are required. As the separation between Ro and Fr increases, this poses severe requirements on storage capabilities.

From (16), it is evident that the contributions from the geostrophic and ageostrophic motions are decoupled and the total energy can be divided in the two components E_G and E_A. Waves pertain just to ageostrophic motions and therefore their signatures are expected to be observed only in E_A. Wave activity is particularly intense in two regions: barotropic modes and shear modes, corresponding to pure gravity waves and pure inertial waves, respectively. As Fr is increased from 0.001 to 0.1, the importance of gravity waves on the overall ageostrophic spectrum becomes smaller. Moreover, also the range of wavenumbers largely affected decreases as Fr becomes comparable to Ro. On the other hand, the extent of the region pertaining to inertial waves is not very affected

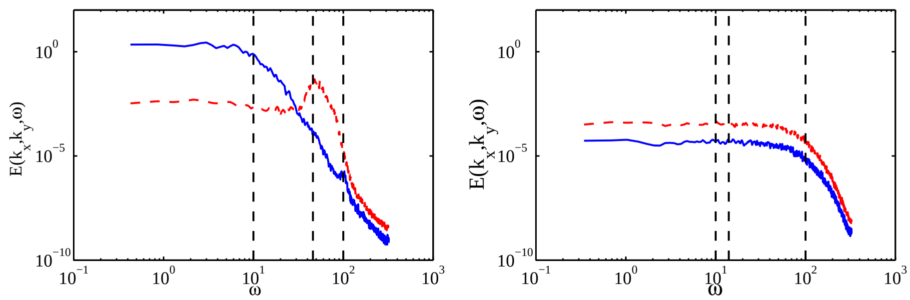

FIGURE 15. Examples of the time-frequency spectrum for (*left*) a large scales ($k_h = 10, k_v = 2$) and (*right*) a small scales ($k_h = 50, k_v = 50$) Fourier mode. —— geostrophic spectrum E_G; - - - ageostrophic spectrum E_A. Vertical helping dashed lines represent the inertial frequency f, the dispersion relation frequency ω_d and the Brunt-Väisälä frequency N (from left to right).

by changes in Fr. It is worth noticing that the region where wave motions are most important does not coincide with the forcing wavenumbers.

In figure 15 the frequency energy spectra for two particular modes, a large scale mode, $(k_h, k_z) = (10, 2)$, and a small scale mode, $(k_h, k_z) = (50, 50)$, are shown for $Ro = 0.1$ and $Fr = 0.01$. In the large scale mode, geostrophic energy dominates at low frequencies, attaining values that are about two orders of magnitude larger than the ageostrophic counterpart. At the inertial frequency, the geostrophic spectrum starts to decay, whereas the ageostrophic spectrum stays rather flat and peaks in a range between Ro^{-1} and Fr^{-1}. In this region, ageostrophic energy dominates. The distinct peak corresponds to motions with a particular frequency, *i.e.* waves, which closely match with the frequency ω_d of the dispersion relation (12). When we turn to the small-scale mode, we note that no distinct peak can be observed and both the geostrophic and the ageostrophic spectra show a rather flat behaviour with comparable magnitude.

According to equation (12), the dispersion frequency ω_d is constant along straight lines in a $k_h - k_z$ plane. In order to investigate whether waves with a particular frequency can be observed, the geostrophic energy spectrum, $E_G(k_h, k_z, \omega)$, and the ageostrophic energy spectrum, $E_A(k_h, k_z, \omega)$, have been averaged over modes that have similar ω_d. Seven frequency bands were chosen, centred around ω_d and logarithmically ranging from Ro^{-1} up to Fr^{-1}. In order to separate contributions from large scales and small scales motions, the averaged spectra were divided into large scales spectra, with $k = \sqrt{k_h^2 + k_z^2} < 10$, and small scales spectra, with $k > 10$. In figure 16 the averaged spectra are shown. The large scales geostrophic part shows a rather flat behaviour at high frequencies. This is clearly due to the forcing that is prescribed to be

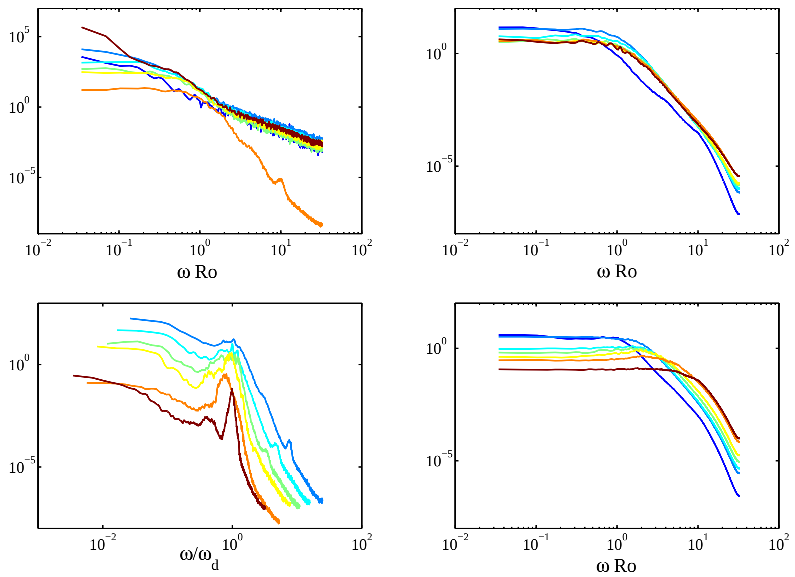

FIGURE 16. Averaged time frequency geostrophic (*top*) and ageostrophic (*bottom*) power energy spectra. The *left* figures refers to the large scales modes, whereas the *right* figures refers to the small scales modes. Note that for the figure on the top left, the frequency axis has been rescaled with the dispersion relation frequency ω_d, which differs from curve to curve, in order to highlight the peaks due to wave motions.

white noise in time, *i.e.* all the frequencies are excited. Notwithstanding, the small scales geostrophic spectra (shown in the top right plot of figure 16) do not conserve the memory of the forcing and large decaying rates are found at high frequencies, with $E_G(\omega) \approx \omega^{-4}$. The cut-off frequency at which the small scale spectrum starts to decay is of the order of the rotation rate f, showing that most of the energy is concentrated at frequencies smaller or comparable to f.

In the bottom left panel of figure 16, the large scales ageostrophic frequency spectra are plotted. The distinct peaks at $\omega = \omega_d$ show that wave activity is important in this range of wavenumbers. Note that both the geostrophic and ageostrophic large scales spectra show a small but distinct peak at $\omega_d = Fr^{-1}$. This is a spurious effect of an accumulation of energy in the barotropic mode, $k_z = 0$, which leads to the formations of a strong wave signature at $\omega_d\,(k_z = 0) = Fr^{-1}$, contaminating all modes through non linear interactions, both in the geostrophic and ageostrophic part. Nevertheless, for the collected modes, the amount of energy around $\omega = Fr^{-1}$ is very small, around 10^{-6} times smaller than the total. We therefore conclude that these motions are not

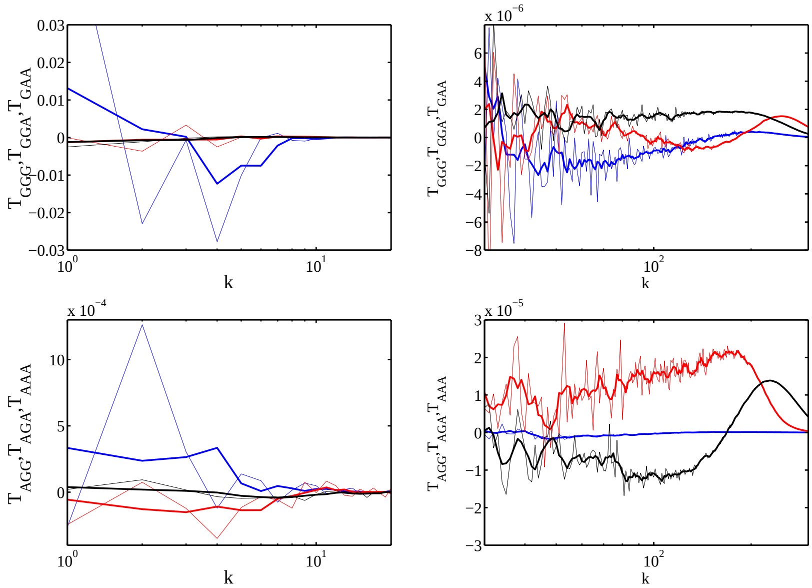

FIGURE 17. *(top)* Transfer of energy into the geostrophic modes at large scales (*left*) and small scales (*right*). $T_{GGG}(\mathbf{k})$ (*blue*); $T_{GGA}(\mathbf{k})$ (*red*); $T_{GAA}(\mathbf{k})$ (*black*). *(bottom)* Transfer of energy into the ageostrophic modes at large scales (*left*) and small scales (*right*). (*blue*) $T_{AGG}(\mathbf{k})$; (*red*) $\mathrm{T}_{AGA}(\mathbf{k})$; (*black*) $T_{AAA}(\mathbf{k})$. Thick lines represent low-pass filtered counterparts.

dynamically important. When we turn to the small-scale ageostrophic spectra in the bottom right plot of figure 16, distinct peaks cannot be observed. Instead, spectra show a rather flat behaviour on a relatively large range of frequencies. Our general conclusion is thus that wave activity is important at large scales, corresponding to wave numbers close to the forcing scale, but is negligible at the small scale.

7. Triad interactions

We start by analysing the exchange of energy between geostrophic and ageostrophic modes. The quantities in the following were computed from individual flow fields and then averaged using six realizations of the run aBQ1. In the top plots of figure 17, the transfer into geostrophic energy separated in its three different contributions, as given by equation (19), is shown. Despite the averaging, curves still show a somewhat spiky behaviour. Low-pass filtered counterparts characterized by smoother trends are also shown in thicker lines. At large scales, the contribution from T_{GGG} dominates, leading to an upscale cascade of energy. At smaller scales, the three parts attain comparable

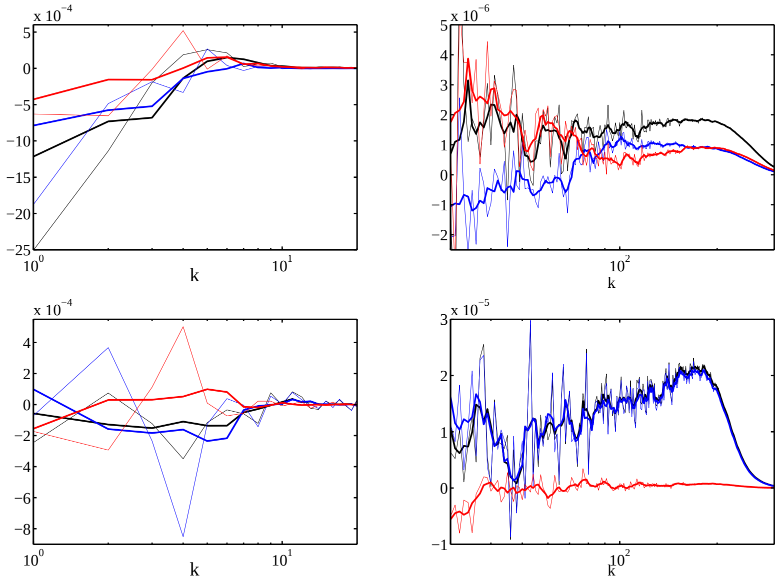

FIGURE 18. Transfer of energy into the geostrophic modes (*top*) and into the ageostrophic modes (*bottom*) due to the interaction between one geostrophic mode and two ageostrophic modes. (*Left*) figures pertain to the large scales and (*right*) figures pertain to the small scales. Total interaction $T_{GAA}(\mathbf{k})$ and $T_{AGA}(\mathbf{k})$ *black*; interaction within the same class $T_{G\pm\pm}(\mathbf{k})$ and $T_{\pm G\pm}(\mathbf{k})$ (*blue*); interaction between the different class $T_{G\pm\mp}(\mathbf{k})$ and $T_{\pm G\mp}(\mathbf{k})$ (*red*). Thick lines represent low-pass filtered counterparts.

magnitudes with T_{GGG} being preferentially negative and T_{GAA} preferentially positive.

On the other hand, the large-scale transfer of energy into ageostrophic energy is mainly due to positive contributions of T_{AGG}. This result is consistent with the statistical mechanical analysis of Bartello (1995), suggesting that this term is mainly responsible for the transfer of energy from geostrophic motions to ageostrophic motions in the so-called process of "geostrophic adjustment". Nevertheless, our analysis also shows that there is another term of comparable magnitude, namely T_{AGA}. It attains negative values, removing energy from the large scales and producing a downscale transfer of energy. Note that if potential vorticity were a conserved quantity, the interaction term T_{AGA} would only allow energy exchange between two ageostrophic modes, leaving the geostrophic mode unchanged, and the corresponding interaction term T_{GAA} would therefore be zero. This is not the case in our simulations, as can be seen in the top plot of figure 17. However, T_{GAA} is one order of magnitude smaller than T_{AGA}, consistent with the analysis of Bartello (1995).

The total energy transfer at small scales is dominated by two contributions, T_{AGA} and T_{AAA}. It should be noted that the scales in the top right and bottom right plots of fig 17 are different. The magnitude of the ageostrophic energy transfer terms at small scales is one order of magnitude larger than their geostrophic counterparts. Both T_{AGA} and T_{AAA} presents the possibility of involving resonant wave interactions. With respect to the term T_{AGA}, if resonance were to happen, the interaction would have to involve two waves with equal but opposite frequencies. As shown in Appendix B, wave motions can be classified according to the two eigenmodes of the linear part of (6b) and (6c). Resonance must occur between one wave of the first class (pertaining to the first eigenmodes) and one of the second class of waves (pertaining to the second eigenmodes). In the bottom panels of figure 18, the term T_{AGA} has been further decomposed into the terms pertaining to the interaction $T_{\pm G\pm}$ within the same class and the terms pertaining to the interaction $T_{\pm G\mp}$ between the two different classes. Resonant wave interactions can only make contributions to $T_{\pm G\mp}$ and not to $T_{\pm G\pm}$. The interaction within the same class accounts for almost the whole T_{AGA} term, with $T_{\pm G\mp}$ being two orders of magnitude smaller than $T_{\pm G\pm}$. This clearly shows that resonant wave-wave interactions cannot explain the downscale transfer of energy. At large scales, the interactions within the same class and the interaction between the classes show comparable magnitude, with the former being preferentially negative and the latter being preferentially positive. An analogous decomposition of T_{GAA} is also shown in the top plots of figure 18. Interactions within and between classes show similar behaviour with comparable magnitude over the whole range of scales, suggesting that there is no preferable type of interaction.

In order to further study how energy is exchanged among wavenumbers as well as the locality of the energy transfer in wavenumber space, we consider the triad energy transfer integrated over spherical shells in wavenumber space, $T(k,p,q)$. Roughly one hundred shells were chosen, logarithmically spanning the interval $[1,300]$. In figure 19, $T_{AGA}(k,p,q)$ is shown in a $p-q$ plane at $k = 110$, *i.e.* within the turbulent cascade. At this location, the effect of viscosity is negligible and the term T_{AGA} constitutes the largest contribution, as shown in figure 17. As in turbulent flows, the energy transfer term T_{AGA} in a $p-q$ plane concentrates in two regions, corresponding to one wavenumber of comparable magnitude respect to k and the other wavenumber being very small, *i.e.* strongly non-local triads. In agreement with the results of Ohkitani & Kida (1992) and Maltrud & Vallis (1993), the transfer of energy, however, is between the two comparable wavenumbers, whereas the small wavenumber does not exchange energy within the triad but rather acts as a catalyser. It is worth pointing out that such triads may satisfy the resonant condition. Simple geometrical considerations reveal that the three wavenumbers involved in such triads lay along the same line in wavenumber space. From the dispersion

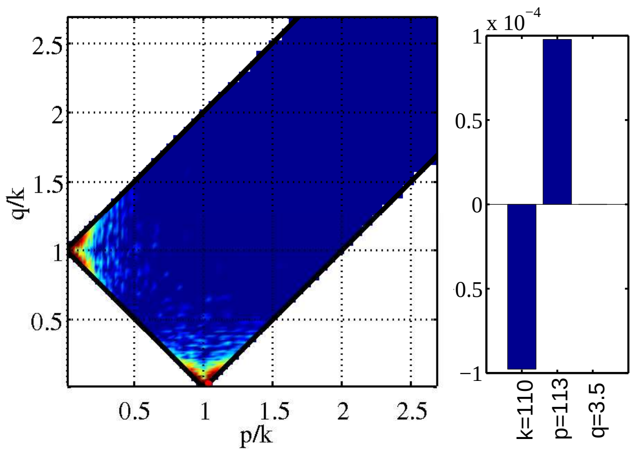

Figure 19. (*left*) Absolute value of the energy transfer function $T_{AGA}(k,p,q)$ in a $p-q$ plane at $k=110$. Note that p and q are rescaled with k. The colour axis has a logarithmic scale. (*right*) example of a dominant triad interaction, corresponding to the red spot in the left figure.

relation (12), it is therefore evident that waves in these modes possess the same frequencies. However, Lelong & Riley (1991) showed that the transfer of energy in a vortex-wave-wave interaction between the two waves tends to zero when the horizontal projection of the wave wavenumbers are parallel to each other, as in this case. Thus, also the spectral transfer of energy strongly supports the conjecture that transfer of energy between scales is a result of turbulent dynamics.

We now turn to the transfer of energy at small scales among ageostrophic modes represented by T_{AAA}. Despite being smaller in magnitude, this term is of leading order at very small scales, as shown by figure 17. According to (21), such a term is conservative and thus only moves energy among scales. Its role mainly consists in extracting energy from the middle range of wavenumbers to feed the dissipation range, in agreement with the finding of Waite & Bartello (2004). In order to obtain some insight in the dynamics of such a process, we investigate the quantity $T_{AAA}(k,p,q)$ in figure 20. As before, the $p-q$ plane at $k=110$ is displayed. Triad interactions show a somewhat more sparse behaviour as compared to figure 19. Also in this case, regions pertaining to one large wavenumber (comparable to k) and one small wavenumber show intense transfer which is local and mainly between the two large wavenumbers of the triad. Such transfer is downscale and consistent with a turbulent dynamics. Besides, large energy transfers are also obtained in regions corresponding to interactions with wavenumbers larger than k, which lead to the net transfer of energy towards large wavenumber seen in figure 17. Interestingly, most of the energy transfers is found in regions for which $p \approx k+q$ or $q \approx k+p$, *i.e.* nearly

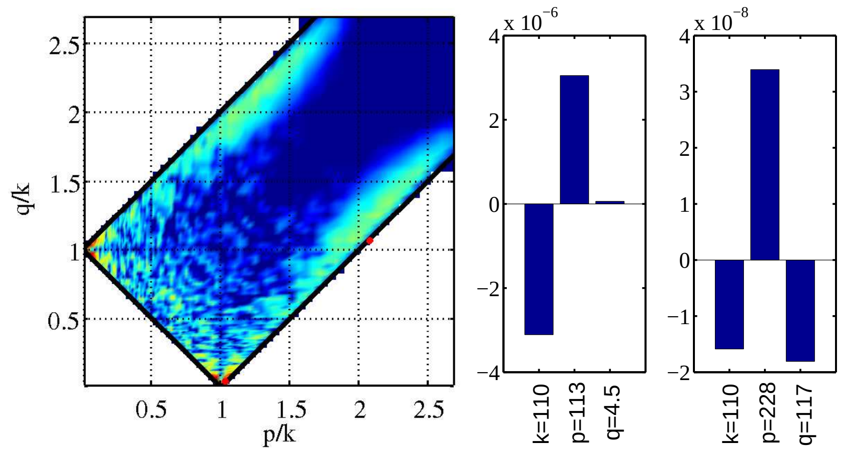

FIGURE 20. (*left*) Absolute value of the energy transfer function $T_{AAA}(k,p,q)$ in a $p-q$ plane at $k=110$. Note that p and q are rescaled with k. The colour axis has a logarithmic scale. (*centre*) and (*right*) examples of two dominant triad interactions corresponding to the red spots in the left figure.

parallel vectors in a wavenumber space. Figure 20 shows the transfer of energy in such a triad. As opposed to a typical turbulent cascade, transfer of energy is highly non-local, with energy flowing out of the two smaller wavenumbers and into the largest wavenumber. Since the wavenumber vectors are aligned, waves possess all similar frequencies. Resonance condition is therefore hardly satisfied, suggesting that wave-wave-wave resonant interactions are of minor importance also in this type of energy transfer.

8. Conclusions

We have studied the route to dissipation in strongly stratified and rotating flows, covering a range of values of Ro and Fr, representative for large scale atmospheric flows. In agreement with the simulations of Vallgren *et al.* (2011), finite rotation rates led to departures from the quasi-geostrophic dynamics. As Ro is increased, the amount of energy cascading up-scale decreases and a fraction of the injected energy starts to cascade downscale. Thus, a finite Rossby number may reconcile the apparent paradox that energy dissipation should be absent in flows conforming to QG dynamics to lowest order. Interestingly, the forward energy cascade towards small scales leads to a shallowing of the energy spectra, from $\sim k_h^{-3}$ to $\sim k_h^{-5/3}$, in agreement with the observations of Nastrom & Gage (1985). At large scales, the rotational spectrum scales as $\sim k_h^{-3}$, in agreement with QG dynamics, whereas the divergent spectrum is several orders of magnitude smaller and is somewhat more shallow than $k_h^{-5/3}$. At the wave number where the magnitudes of the rotational and divergent spectra become comparable, the rotational spectrum shallows and both spectra approximately scale as $k_h^{-5/3}$.

Spectral fluxes indicate the existence of an inertial range of scale where the energy is inviscidly transferred from the large scales to the very smallest scales. The amount of energy cascading downscale strongly increases with Ro and weakly decreases with Fr. This is consistent with the hypothesis that strong rotation leads to an inverse energy cascade, whereas strong stratification favours a forward energy cascade. The primitive equation set therefore represents the limiting case for strongly stratified flows, for which the related small-scale dissipation is the upper limit. The separate kinetic and potential energy fluxes show that there is a transfer of energy from potential to kinetic energy at large scales and a kinetic to potential energy transfer at smaller scales where the energy cascade is dominant.

Despite the fact that potential enstrophy is not a conserved quantity in PE and BQ, intermediate Rossby number simulations show a range of scales in which both the enstrophy and the energy flux are constant. A forward cascade of energy and potential enstrophy coexist. For $Ro = 0.05$ and $Fr = 0.01$, such a range extends over a decade. Enstrophy cascades downscale by triad interactions involving three geostrophic modes while energy is cascading downscale by interactions involving at least one ageostrophic mode, with a dominant contribution from interactions involving two ageostrophic and one geostrophic mode.

Structures characteristic of QG dynamics as filamentation and large-scale baroclinic vortices are observed in the flow. However, small-scale turbulent patches can also be found where the dissipation of energy is particularly intense. The local Froude number in the turbulent patches is of the order of unity, suggesting that KH instability is a potentially important mechanism supporting a direct energy cascade.

The role of internal gravity waves was investigated through time frequency analyses of time series from single Fourier modes. Frequency spectra from low wave number modes, $k < 10$, of ageostrophic motions show distinct peaks at the characteristic wave frequency. At higher wave numbers, $k > 10$, no such peaks could be observed, indicating that waves become less important at scales where the energy cascade becomes dominant. That the downscale energy cascade is dominated by turbulent motions rather than waves is also confirmed by the investigation of triad interactions. Energy is mainly transferred by interactions between two ageostrophic and one geostrophic mode. If these interactions had been the result of resonant wave interactions the two ageostrophic modes would correspond to two waves with frequencies of equal magnitude but opposite signs. Our analysis clearly shows that this cannot be the case. The contribution to the energy transfer from interactions involving such motions is at least two orders of magnitude smaller that the total transfer. We therefore conclude that the motions of the downscale energy cascade in strongly stratified and rotating systems are genuinely turbulent.

The authors wish to thank Dr. Pierre Augier for valuable comments on the manuscript. Computer time provided by SNIC (Swedish National Infrastructure for Computing) is gratefully acknowledged.

Appendix A.

According to (14), the energy content in spectral space can be written in the quadratic form

$$E(\mathbf{k}) = \left\{ \begin{array}{c} \hat{u}(\mathbf{k}) \\ \hat{v}(\mathbf{k}) \\ \hat{w}(\mathbf{k}) \\ \hat{b}(\mathbf{k}) \end{array} \right\}^H \begin{bmatrix} 1 & 0 & 0 & 0 \\ 0 & 1 & 0 & 0 \\ 0 & 0 & Fr^2 & 0 \\ 0 & 0 & 0 & 1 \end{bmatrix} \left\{ \begin{array}{c} \hat{u}(\mathbf{k}) \\ \hat{v}(\mathbf{k}) \\ \hat{w}(\mathbf{k}) \\ \hat{b}(\mathbf{k}) \end{array} \right\}. \tag{34}$$

Here, the superscript $\cdot^H$ refers to the Hermitian transpose. Using the inversion relations (26), we can express the primitive variable $\hat{u}(\mathbf{k})$, $\hat{v}(\mathbf{k})$, $\hat{w}(\mathbf{k})$ and $\hat{b}(\mathbf{k})$ from the prognostic variable $\hat{q}(\mathbf{k})$,$\hat{a}_1(\mathbf{k})$ and $\hat{a}_2(\mathbf{k})$ as

$$\left\{ \begin{array}{c} \hat{u}(\mathbf{k}) \\ \hat{v}(\mathbf{k}) \\ \hat{w}(\mathbf{k}) \\ \hat{b}(\mathbf{k}) \end{array} \right\} = \begin{bmatrix} \frac{ik_y}{k^2} & \frac{iRo\, k_x k_y}{k^2 k_z} & \frac{-iRo\left({k_x}^2+{k_z}^2\right)}{k^2 k_z} \\ \frac{-ik_x}{k^2} & \frac{iRo\left({k_y}^2+{k_z}^2\right)}{k^2 k_z} & \frac{-iRo\, k_x k_y}{k^2 k_z} \\ 0 & -\frac{ik_y}{k_z^2} & \frac{ik_x}{k_z^2} \\ \frac{k_z}{k^2} & Ro\,\frac{k_x}{k^2} & Ro\,\frac{k_y}{k^2} \end{bmatrix} \left\{ \begin{array}{c} \hat{q}(\mathbf{k}) \\ \hat{a}_1(\mathbf{k}) \\ \hat{a}_2(\mathbf{k}) \end{array} \right\}. \tag{35}$$

Energy can therefore be written as

$$E(\mathbf{k}) = \tilde{\mathbf{u}}^H \mathsf{E} \tilde{\mathbf{u}} \tag{36}$$

where $\tilde{\mathbf{u}} = \{\hat{q}\,, \hat{a}_1\,, \hat{a}_2\}$ and

$$\frac{1}{2} \left[\begin{array}{cc} k^{-2} & 0 \\ 0 & \frac{Ro^2 k_z^2\left(k_x^2 k_y^2 + k_x^2 k_z^2 + k_y^4 + 2k_y^2 k_z^2 + k_z^4\right) + Fr^2 k^4 k_y^2}{k^4 k_z^4} \\ 0 & -\frac{k_x k_y\left(Ro^2 k_z^2 + Fr^2 k^2\right)}{k_z^4 k^2} \end{array} \right. \tag{37}$$

$$\left. \begin{array}{c} 0 \\ -\frac{k_x k_y\left(Ro^2 k_z^2 + Fr^2 k^2\right)}{k_z^4 k^2} \\ \frac{Ro^2 k_z^2\left(k_x^2 k_y^2 + k_y^2 k_z^2 + k_x^4 + 2k_x^2 k_z^2 + k_z^4\right) + Fr^2 k^4 k_x^2}{k_z^4 k^4} \end{array} \right], \tag{38}$$

showing the decoupling between geostrophic and ageostrophic mode.

Appendix B.

By retaining only the linear part, equations (6b) and (6c) can be written as

$$\begin{bmatrix} k_z^2 + k_y^2 \frac{Fr^2}{Ro^2} & -\frac{Fr^2}{Ro^2} k_x k_y \\ -\frac{Fr^2}{Ro^2} k_x k_y & k_z^2 + k_x^2 \frac{Fr^2}{Ro^2} \end{bmatrix} \frac{\partial}{\partial t} \left\{ \begin{array}{c} \hat{a}_1 \\ \hat{a}_2 \end{array} \right\} = \tag{39}$$

$$\frac{1}{Ro} \begin{bmatrix} -k_x k_y & k_z^2 + k_x^2 \\ -k_z^2 - k_y^2 & +k_x k_y \end{bmatrix} \left\{ \begin{array}{c} \hat{a}_1 \\ \hat{a}_2 \end{array} \right\}, \tag{40}$$

which can be recast in an eigenvalue problem for the complex frequency λ

$$(\mathsf{B} - \lambda \mathsf{A})\,\mathbf{a} = 0. \tag{41}$$

where $\mathbf{a} = [\hat{a}_1\,,\,\hat{a}_2\,]^T$. The discriminant of (41) gives the dispersion relation (12), *i.e.* $\lambda_{1,2} = \pm i\omega_d$. The matrix M whose columns are the eigenvectors of (39) is a linear operator which allows to project $\mathbf{a}$ on the eigenvector basis

$$\mathbf{a} = \mathsf{M}\mathbf{e} \qquad\qquad \mathbf{e} = \mathsf{M}^{-1}\mathbf{a} \tag{42}$$

where $\mathbf{e}$ is the projection of $\mathbf{a}$ in the eigenvector basis. The first component of $\mathbf{e}$ pertains to waves with positive frequency whereas the second component of $\mathbf{e}$ pertains to waves with negative frequencies. We divide the transfer term T_{AGA} into two parts, $T_{\pm G\pm}$ and $T_{\pm G\mp}$, where the first part contains contributions involving the same eigenvectors and the second part contains contributions involving two different eigenvectors. To calculate these two parts we need to separate the ageostrophic fields into two fields associated with each of the eigenvectors. This can easily be done by projecting a_1 and a_2 on the eigenvector basis, setting either the first class or the second class of modes to zero and finally transforming back to the normal basis which the inversion relations (26) can be applied to.

References

Augier, P., Chomaz, J.-M. & Billant, P. 2012 Spectral analysis of the transition to turbulence from a dipole in stratified fluids. *submitted to J. Fluid Mech.* (-), –.

Bartello, P. 1995 Geostrophic Adjustment and Inverse Cascades in Rotating Stratified Turbulence. *J. Atmos. Sci.* **52**, 4410–4428.

Bellet, F., Godeferd, F. S., Scott, J. F. & Cambon, C. 2006 Wave turbulence in rapidly rotating flows. *J. Fluid Mech.* **562**, 83–121.

Billant, P. & Chomaz, J.-M. 2001 Self-similarity of strongly stratified inviscid flows. *Physics of Fluids* **13** (6), 1645–1651.

Boer, G. J. & Shepherd, T. G. 1983 Large-Scale Two-Dimensional Turbulence in the Atmosphere. *J. Atmos. Sci.* **40**, 164–184.

Boffetta, G. & Musacchio, S. 2010 Evidence for the double cascade scenario in two-dimensional turbulence. *Phys. Rev. E* **82**, 016307.

Brethouwer, G., Billant, P., Lindborg, E. & Chomaz, J.-M. 2007 Scaling analysis and simulation of strongly stratified turbulent flows. *J. Fluid Mech.* **585**, 343–368.

Cambon, C., Mansour, N. N. & Godeferd, F. S. 1997 Energy transfer in rotating turbulence. *J. Fluid Mech.* **337**, 303–332.

Canuto, C., Hussaini, M. Y., Quarteroni, A. & Zang, T. A. 1988 *Spectral methods in Fluid Dynamics*. Springer-Verlag.

Charney, Jule G. 1971 Geostrophic turbulence. *J. Atmos. Sci.* **28** (6), 1087–1094.

Cho, J. Y. N. & Lindborg, E. 2001 Horizontal velocity structure functions in the upper troposphere and lower stratosphere 1. observations. *J. Geophys. Res.* **106** (D10), 10223–10232.

Garrett, C. & Munk, W. 1979 Internal Waves in the Ocean. *Annual Review of Fluid Mechanics* **11**, 339–369.

Gill, A. E. 1982 *Atmosphere-ocean dynamics*. Academic Press, New York.

Godeferd, F. S. & Cambon, C. 1994 Detailed investigation of energy transfers in homogeneous stratified turbulence. *Physics of Fluids* **6** (6), 2084–2100.

Hamilton, K., Takahashi, Y. O. & Ohfuchi, W. 2008 Mesoscale spectrum of atmospheric motions investigated in a very fine resolution global general circulation model. *J. Geophys. Res.* **113** (18).

Kitamura, Y. & Matsuda, Y. 2006 The k_H^{-3} and $k_H^{-5/3}$ energy spectra in stratified turbulence. *Geophys. Res. Lett.* **33**, L05809.

Kraichnan, R. H. 1967 Inertial ranges in two-dimensional turbulence. *Physics of Fluids* **10** (7), 1417–1423.

Leith, C. E. & Kraichnan, R. H. 1972 Predictability of Turbulent Flows. *J. Atmos. Sci.* **29**, 1041–1058.

Lelong, M.-P. & Riley, J. J. 1991 Internal wave-vortical mode interactions in strongly stratified flows. *J. Fluid Mech.* **232**, 1–19.

Lilly, D. K. 1983 Stratified turbulence and the mesoscale variability of the atmosphere. *J. Atmos. Sci.* **40** (3), 749–761.

Lindborg, E. 2006 The energy cascade in a strongly stratified fluid. *J. Fluid Mech.* **550**, 207–242.

Lindborg, E. 2007 Horizontal Wavenumber Spectra of Vertical Vorticity and Horizontal Divergence in the Upper Troposphere and Lower Stratosphere. *J. Atmos. Sci.* **64**, 1017.

Lindborg, E. & Brethouwer, G. 2007 Stratified turbulence forced in rotational and divergent modes. *J. Fluid Mech.* **586**, 83–108.

Maltrud, M. E. & Vallis, G. K. 1993 Energy and enstrophy transfer in numerical simulations of two-dimensional turbulence. *Physics of Fluids* **5**, 1760–1775.

Ménesguen, C., Hua, B. L., Papenberg, C., Klaeschen, D., Géli, L. & Hobbs, R. 2009 Effect of bandwidth on seismic imaging of rotating stratified turbulence surrounding an anticyclonic eddy from field data and numerical simulations. *Geophys. Res. Lett.* **360**.

Molemaker, M. J. & McWilliams, J. C. 2010 Local balance and cross-scale flux of available potential energy. *J. Fluid Mech.* **645**, 295–314.

Molemaker, M. J., McWilliams, J. C. & Capet, X. 2010 Balanced and unbalanced routes to dissipation in an equilibrated Eady flow. *J. Fluid Mech.* **654**, 35–63.

Molemaker, M. J., McWilliams, J. C. & Yavneh, I. 2005 Baroclinic instability and loss of balance. *J. Phys. Ocean.* **35**, 1505–1517.

Muller, P., McWilliams, J. C. & Molemaker, M. J. 2005 Routes to dissipation in the ocean: the 2d/3d turbulence conundrum. In *Marine Turbulence: Theories, Observations, and Models* (ed. H.Z. Baumert, J. Simpson & J. Sündermann), pp. 397–405. Cambridge University Press.

Munk, W. 1981 Internal waves and small-scale processes. *Evolution of Physical Oceanography* pp. 264–291.

Nastrom, G. D. & Gage, K. S. 1985 A climatology of atmospheric wavenumber spectra of wind and temperature observed by commercial aircraft. *J. Atmos. Sci.* **42**, 950–960.

Ohkitani, K. 1990 Nonlocality in a forced two-dimensional turbulence. *Physics of Fluids A: Fluid Dynamics* **2** (9), 1529–1531.

Ohkitani, K. & Kida, S. 1992 Triad interactions in a forced turbulence. *Physics of Fluids A: Fluid Dynamics* **4** (4), 794–802.

Pedlosky, J. 1987 *Geophysical fluid dynamics*. Springer.

Phillips, O. M. 1981 Wave interactions - the evolution of an idea. *J. Fluid Mech.* **106**, 215–227.

Riley, J. J. & deBruynKops, S. M. 2003 Dynamics of turbulence strongly influenced by buoyancy. *Physics of Fluids* **15** (7), 2047–2059.

Scott, R. K. 2007 Nonrobustness of the two-dimensional turbulent inverse cascade. *Phys. Rev. E* **75**, 046301.

Skamarock, W. C. 2004 Evaluating mesoscale nwp models using kinetic energy spectra. *Monthly Weather Review* **132** (12), 3019–3032.

Staquet, C. & Sommeria, J. 2002 Internal gravity waves: from instabilities to turbulence. *Annual Review of Fluid Mechanics* **34**, 559–593.

Takahashi, Y. O., Hamilton, K. & Ohfuchi, W. 2006 Explicit global simulation of the mesoscale spectrum of atmospheric motions. *Geophys. Res. Lett.* **33**, L12812.

Vallgren, A. 2011 Infrared reynolds number dependency of the two-dimensional inverse energy cascade. *J. Fluid Mech.* **667**, 463–473.

Vallgren, A., Deusebio, E. & Lindborg, E. 2011 A possible explanation of the atmospheric kinetic and potential energy spectra. *Phys. Rev. Lett.* **99**, 99–101.

Vallgren, A. & Lindborg, E. 2010 Charney isotropy and equipartition in quasi-geostrophic turbulence. *J. Fluid Mech.* **656**, 448–457.

Vallgren, A. & Lindborg, E. 2011 The enstrophy cascade in forced two-dimensional turbulence. *J. Fluid Mech.* **671**, 168–183.

Vallis, G. K. 2006 *Atmospheric and Oceanic Fluid Dynamics: Fundamentals and Large-scale Circulation; electronic version*. Leiden: Cambridge Univ. Press.

Viúdez, Á. & Dritschel, D. G. 2006 Spontaneous generation of inertia-gravity wave packets by balanced geophysical flows. *J. Fluid Mech.* **553**, 107–117.

Waite, M. L. & Bartello, P. 2004 Stratified turbulence dominated by vortical motion. *J. Fluid Mech.* **517**, 281–308.

Waite, M. L. & Bartello, P. 2006 The transition from geostrophic to stratified turbulence. *J. Fluid Mech.* **568**, 89–108.

Waite, M. L. & Snyder, C. 2009 The Mesoscale Kinetic Energy Spectrum of a Baroclinic Life Cycle. *J. Atmos. Sci.* **66**, 883.

Paper 3

3

Direct numerical simulations of stratified open channel flows

By Enrico Deusebio, Philipp Schlatter, Geert Brethouwer & Erik Lindborg

Linné Flow Centre, KTH Mechanics
SE-100 44 Stockholm, Sweden

J. Phys., Conf. Ser., 318, 022009, 2011

We carry out numerical simulations of wall-bounded stably stratified flows. We mainly focus on how stratification affects the near-wall turbulence at moderate Reynolds numbers, *i.e.* $Re_\tau = 360$. A set of fully-resolved open channel flow simulations is performed, where a stable stratification has been introduced through a negative heat flux at the lower wall. In agreement with previous studies, it is found that turbulence cannot be sustained for h/L values higher than 1.2, where L is the so-called Monin-Obukhov length and h is the height of the open channel. For smaller values, buoyancy does not re-laminarize the flow, but nevertheless affects the wall turbulence. Near-wall streaks are weakly affected by stratification, whereas the outer modes are increasingly damped as we move away from the wall. A decomposition of the wall-normal velocity is proposed in order to separate the gravity wave and turbulent flow fields. This method has been tested both for open channel and full channel flows. Gravity waves are likely to develop and to dominate close to the upper boundary (centreline for full channel). However, their intensity is weaker in the open channel, possibly due to the upper boundary condition. Moreover, the presence of internal gravity waves can also be deduced from a correlation analysis, which reveals (together with spanwise spectra) a narrowing of the outer structures as the stratification is increased.

1. Introduction

Stably stratified boundary layers have been studied for a long time and are still subject of current research (Nieuwstadt 2005; Flores & Riley 2010; García-Villalba & del Álamo 2011). In order to understand how heat, momentum, moisture and pollutants are exchanged with the earth surface, the study of the atmospheric boundary layers is crucial. An important property of such a flow is its stability: buoyancy forces, due both to humidity and temperature, are present and they actively interact with the flow. During daytime, positive heat fluxes develop at the ground and lead to convective motions. On the other hand, during night time and/or in polar regions, negative fluxes (cooling) are prevalent, and the flow is usually stably stratified. How turbulence is affected by a stable stratification, its suppression for very high stability as well as the influence of internal gravity waves and their interaction with the underlying turbulence, are not fully resolved issues. Nieuwstadt (2005) and Flores & Riley (2010) carried out Direct Numerical Simulations (DNSs) in order to study the turbulence collapse in open-channel cases when a constant heat-flux is forced at the lower wall. Armenio & Sarkar (2002) considered Large-Eddy Simulations (LESs) of a full channel at very high stability, where the stratification was imposed by a constant temperature difference in the vertical direction. The authors found that turbulence remains very active close to the wall, even for very strong stratification, whereas in the centre of the channel wave motions were dominating. Similar results were also recently obtained by García-Villalba & del Álamo (2011), who addressed the problem through DNSs of full channels. Nevertheless, they could not reach continuously turbulent states at such strong stratification as studied by Armenio & Sarkar (2002). As they point out, the turbulence collapse is highly dependent on box sizes, and further investigations on this subject would need boxes large enough to fit both laminar and turbulent patches. Which parameter should be used to determine whether turbulence is suppressed by stable stratification is still disputed: Nieuwstadt (2005) uses the gradient Richardson number provided by the stability analysis $Ri < 0.25$, Flores & Riley (2010) suggest $L/l^+ \approx 10^2$ as a criterion, whereas García-Villalba & del Álamo (2011) quantifies how close the flow is to re-laminarization through the Nusselt number Nu. García-Villalba & del Álamo (2011) also investigated the structures which develop in statistically quasi-stationary limits, finding an intermediate region where the Monin-Obukhov theory seems to apply well. On the other hand, near-wall structures were found to rather scale in viscous units and to be weakly affected by the stable stratification.

In this work, we extend some of these studies, mainly focusing on the statistically steady regimes. We address them through a set of both fully-resolved open channel DNSs and full channel LESs, where a stable stratification is introduced through either a cooling at the lower wall or a constant temperature difference between the upper and the lower walls. Flow structures are studied using correlations analysis, both in the horizontal plane and along the vertical direction. Moreover, in order to better quantify and characterize the gravity wave activity, a new decomposition able to separate the background turbulence from the wave part is developed.

2. Numerical Scheme

The governing equations of the system are the incompressible Navier-Stokes equation within the Boussinesq approximation. Including also the terms related to sub-grid stress modelling, the mathematical model reads

$$\frac{\partial u_i}{\partial t} + u_j \frac{\partial u_i}{\partial x_j} = -\frac{\partial p}{\partial x_i} + \frac{1}{Re}\nabla^2 u_i + Ri\theta\delta_{i2} + \frac{\partial \tau_{ij}^{LES}}{\partial x_j}, \tag{1}$$

$$\frac{\partial u_i}{\partial x_i} = 0, \tag{2}$$

where the temperature θ satisfies an advection-diffusion equation:

$$\frac{\partial \theta_i}{\partial t} + u_j \frac{\partial \theta_i}{\partial x_j} = \frac{1}{RePr}\nabla^2 \theta_i + \frac{\partial q_j^{LES}}{\partial x_j}. \tag{3}$$

Here, u,v and w are the velocity along the streamwise, wall-normal and spanwise directions, respectively. Note that when LES is considered, the physical quantities u,v,w and θ must be regarded as the filtered counterparts. The Reynolds number, Richardson number and Prandtl number are here defined as:

$$Re = \frac{u_\tau L}{\nu}, \qquad Ri_\tau = \frac{g\alpha\theta_{ref} h}{u_\tau^2}, \qquad Pr = \frac{\nu}{\kappa}, \tag{4}$$

where ν and κ are the momentum and thermal diffusivity respectively, g is the acceleration due to gravity and α is the thermal expansion coefficient. The reference temperature θ_{ref} is chosen to be the temperature difference between the upper and lower walls. These equations are discretized using a pseudo-spectral method, assuming periodicity and Fourier expansions in the wall-parallel plane, whereas Chebyshev polynomials are used in the wall-normal direction (Chevalier *et al.* 2007). For the open channel, the upper boundary condition, namely $v = \partial u/\partial y = \partial w/\partial y = 0$, allows us to use half the number of Chebyshev polynomials, either the symmetric or anti-symmetric ones. This method yields a better distribution of the collocation points which avoids the clustering at the free-slip surface, reducing the wall-normal resolution as well as the computational time (Deusebio 2010).

When LES is considered, the dynamic Smagorinsky model (Germano *et al.* 1991) has been used in order to estimate the deviatoric part of τ_{ij}^{LES}, as in the simulation of Armenio & Sarkar (2002). The sub-grid heat fluxes were similarly modelled using an eddy-diffusivity which was deduced from the eddy-viscosity by applying a constant turbulent Prandtl number $Pr_t = 0.6$. The deviatoric part of the SGS terms and the sub-grid scalar fluxes are therefore assumed to be aligned to the strain rate and to the mean scalar gradient, respectively.

In table 1, the different simulation cases are summarized. Slightly different setups were adopted in order to meet the reference cases: while the stratification was introduced through a negative heat-flux at the wall in the open channel simulations, a constant temperature difference between the lower and the upper wall was prescribed in the full channel. Moreover, whereas all the open channel simulations were always started from a neutral flow, in the full channel cases the stratification was progressively increased among the runs, as done by Armenio & Sarkar (2002) and García-Villalba & del Álamo (2011). In order to compare with the works by Nieuwstadt (2005) and Flores & Riley (2010), the stratification in the open channel flows is quantified by the non-dimensional inverse of the Monin-Obukhov scale:

$$\frac{h}{L} = -\frac{hg\alpha q_0}{u_\tau^3}. \tag{5}$$

Case	SGS model	Resolution	Box Size	Re_τ	Ri	h/L
OCH0	No	768 x 129 x 768	$8\pi h$ x h x $4\pi h$	360	0	0
OCH1	No	768 x 129 x 768	$8\pi h$ x h x $4\pi h$	360	55	0.71
OCH2	No	768 x 129 x 768	$8\pi h$ x h x $4\pi h$	360	113	1.2
OCH3	No	768 x 129 x 768	$8\pi h$ x h x $4\pi h$	360	167	1.5
CH0	Smag.	64 x 97 x 64	$4\pi h$ x $2h$ x $2\pi h$	180	0	0
CH1	Smag.	64 x 97 x 64	$4\pi h$ x $2h$ x $2\pi h$	180	44	0.85
CH2	Smag.	64 x 97 x 64	$4\pi h$ x $2h$ x $2\pi h$	180	87	1.44

TABLE 1. Summary of the simulations.

All the simulations have been run for a sufficiently long time for the flow to reach an almost statistically stationary state. Whereas the velocity field adjusts relatively quickly when stratification is introduced, the temperature field converges extremely slowly and long times are therefore required to achieve the same heat flux at the upper and lower walls.

3. Results

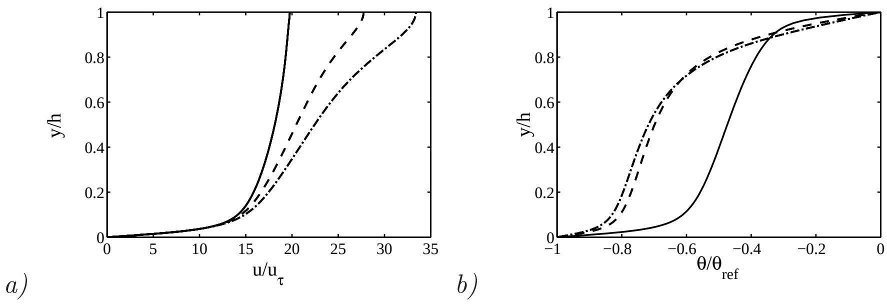

FIGURE 1. Mean profiles. *a)* streamwise velocity; *b)* temperature. ——— baseflow; ········ $h/L = 0.71$; –·– $h/L = 1.20$.

The collapse of turbulence in ground-cooled open channel flows is first investigated. Results are in agreement with the finding by Nieuwstadt (2005) and Flores & Riley (2010). The temporal evolution of the turbulent kinetic energy shows that turbulence is completely suppressed by the stable stratification for h/L values higher than 1.2, and the flow relaminarizes. On the other hand, values lower than 1.2 allow for a continuously turbulent state which is, however, affected by buoyancy. In the latter case, the turbulent kinetic energy first decreases, due to a temporary collapse of turbulence at the wall, and then increases to a value which is the same as for the unstratified case.

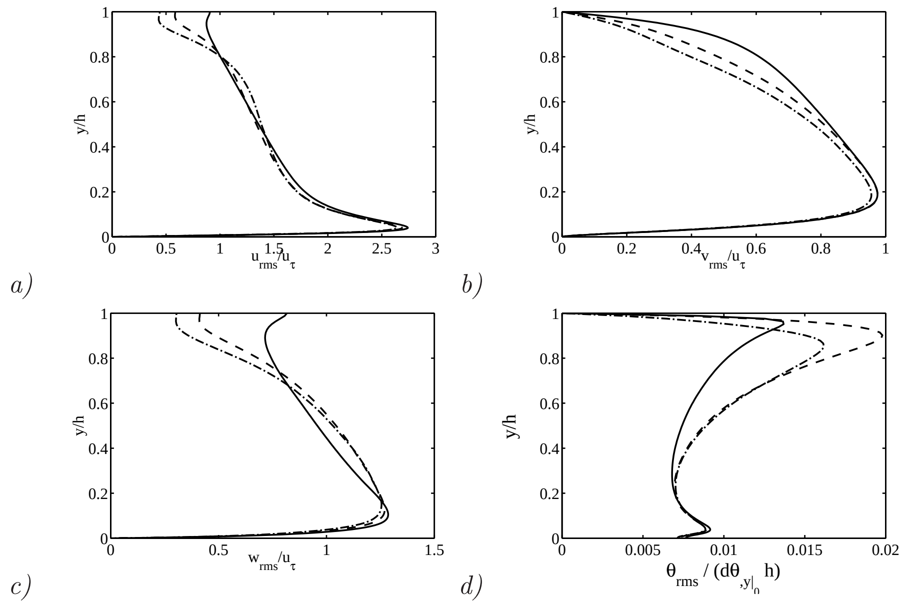

FIGURE 2. Root mean square profiles. *a)* streamwise velocity; *b)* wall-normal velocity; *c)* spanwise velocity; *d)* temperature. ——— baseflow; ········ $h/L = 0.71$; −·− $h/L = 1.20$.

In Fig. 1, the mean velocity profile and the mean temperature profile are shown for unstratified and stratified cases. Close to the wall the mean velocity is not affected by the stratification. This is not surprising, reflecting the fact that the pressure gradient, and therefore the wall-shear stress, is the same in the two cases. In the outer region, however significant differences can be observed. As the stratification is increased, the velocity profile steepens progressively and, especially very close to the upper boundary, attains a parabolic (laminar) shape. This is related to the fact that the turbulent wall-normal momentum transport, $\overline{u'v'}$, becomes less efficient due to reduced vertical motions. A similar conclusion can also be drawn from the temperature profile, which approaches a linear dependence, *i.e.* the one found in the laminar case. Also one point statistics (Fig. 2) fall on top of each other in the near-wall region, departing more and more as we move far from the wall: significant decreases of the fluctuations are observed close to the upper boundary for all the three velocity components. Interestingly, close to the upper boundary temperature fluctuations show non-monotonic behaviour with increasing stratification, due to the combined effect of turbulence reduction and of the consequent increase of temperature gradients.

3.1. *Two point lateral spectra*

In Fig. 3 the lateral (spanwise) pre-multiplied spectra are shown, defined as

$$\phi_{ii}(k_z, y) = E_{ii}(k_z) \cdot k_z, \tag{6}$$

where E_{ii} is the Fourier transform of the auto-correlation $B_{ii}(y, r) = \langle u_i(x, y, z) u_i(x, y, z + r)\rangle_x / u^2_{i,rms}(y)$. The spectra in Fig. 3 are plotted as functions of y^+ and λ_z^+. In the unstratified case, the footprint of near-wall streaks, which scales in viscous units, can be recognized as well as the outer structures which scale in outer units. The streak spacing in the B_{uu} spectra appears to be roughly $\lambda^+ = 120$, which agrees with previous simulations and experiments of wall-bounded flows (Jiménez 1998). Moreover, it can be noted that the spacing deduced by the B_{vv} spectra is roughly half of the one found in B_{uu}, as it has already been observed by Kim *et al.* (1987) and Jiménez (1998). When we turn

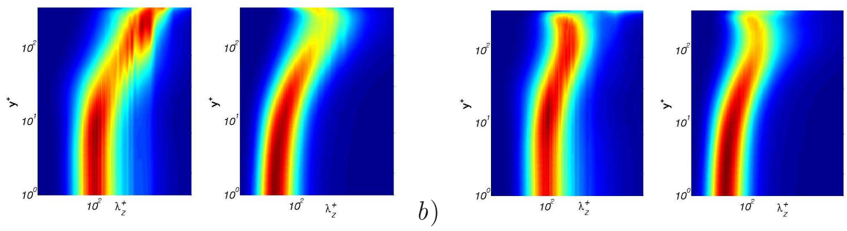

FIGURE 3. Lateral pre-multiplied spectra (normalized by the local root mean squared) for the streamwise uu (*left*) and wall-normal vv (*right*) fluctuations; *a)* unstratified and *b)* stratified cases.

to the stratified lateral pre-multiplied spectra some important observations can be made. First of all, the structures very close to the wall seem to be only slightly influenced by stratification. In spite of the fact that the stratification is largest there (where the temperature gradient is largest), the shape of the spectra close to the wall does not change significantly when compared to the unstratified case. This is true both for the uu and vv spectra. However, significant differences arise in the outer region where it is found that structures become significantly narrower as the stratification is introduced. This is particularly evident in the spanwise spectra uu where the energy maximum, corresponding to the outer structures, goes from $\lambda^+ \approx 750$ down to $\lambda^+ \approx 280$. Note that the normalized spectra do not tell us whether the peak-shift is due to a damping of the largest structures or to an intensification of the narrower structures. However, the non-normalized counterpart of Fig. 3 shows that energy concentrates more and more towards smaller scales when compared to the unstratified cases. Large structures are damped and the smaller ones enhanced. The inhibition of vertical motion not only favours thinner structures in the vertical direction, but also narrower structures in the spanwise direction. On the other hand, it can be noted from the longitudinal spectra (not shown) that the length scales in the streamwise direction do not seem to be affected by stratification.

Similar conclusions can also be drawn from flow visualizations. In Fig. 4, the streamwise velocity field in a $y-z$ plane is shown both for a stratified and an unstratified case. Buoyancy forces and stable stratification mainly affect the outer region, where they damp structures that would extend throughout the whole domain otherwise. These structures penetrate the buffer region from well above and they correspond to the so-called global modes identified in several works, *e.g.* García-Villalba & del Álamo (2011), Hoyas & Jiménez (2006) and Örlü & Schlatter (2011). In Fig. 5, the wall-normal velocity integral length

a)

b)

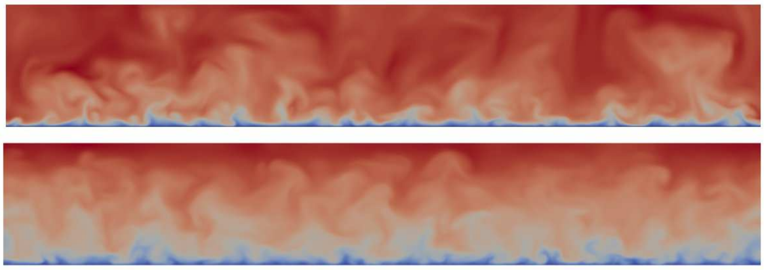

FIGURE 4. Instantaneous streamwise velocity u field in a $y-z$ plane $(L_y, L_z) = (h, 4\pi h)$ for an *a)* unstratified and *b)* stratified case with $h/L = 1.2$.

scale in spectral space, defined as:

$$\overline{L_y}(k_x, k_z) = \int_0^h \int_0^h \frac{\mathrm{Re}\left(\hat{v}(k_x, k_z, y)\hat{v}(k_x, k_z, \tilde{y})\right)}{v_{rms}(y)v_{rms}(\tilde{y})} \mathrm{d}\tilde{y}\mathrm{d}y \qquad (7)$$

is displayed. Flores & Jiménez (2006) used this quantity in order to characterize structures well correlated in the wall-normal direction for smooth and rough walled unstratified flows. This measure was computed for several open channel flow fields, averaged and then, due to the rather noisy behaviour, top-hat filtered. In Fig. 5, both stratified ($h/L = 1.2$) and unstratified cases are shown. First, it can be noted that the magnitude of L_y decreases as the stratification is increased, due to the inhibition of the wall-normal motions. For the unstratified cases the most correlated modes are rather elongated structures in the streamwise direction, *i.e.* modes with k_x small. These structures can still be seen when stratification is introduced, however they tend to move to higher k_z, corresponding to the fact that they become narrower, as also shown in Fig. 3. More interestingly, a new peak also appears which is located at a rather small k_z. It is likely that this peak is associated with gravity waves, *i.e.* motions which are expected to have a higher degree of coherence in the wall-normal direction. The streamwise wave length of these modes, $\lambda_x \approx 2$, agrees with the finding of García-Villalba & del Álamo (2011).

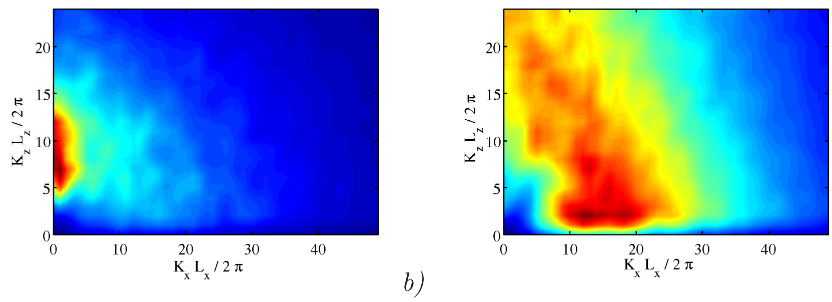

a) b)

FIGURE 5. Color plot of the magnitude of the wall-normal velocity integral length scale $\overline{L_y}(k_x, k_z)$ for *a)* unstratified (OCH0) and *b)* stratified (OCH2) open channel flows.

3.2. *Gravity waves*

In order to detect gravity wave activity, time series of individual Fourier coefficients were collected. We here propose and apply a decomposition of the flow field which is able to separate the turbulent part from the wave part, allowing for a characterization of the different contributions separately. With the aim of testing the novel procedure, LES of channel flows were therefore carried out with conditions similar to the ones used by Armenio & Sarkar (2002) and García-Villalba & del Álamo (2011) (Table 1), who observed strong gravity wave activity in the central region of a full channel.

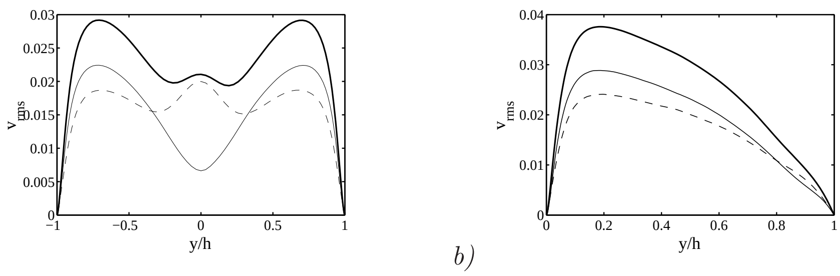

a) b)

FIGURE 6. *In* and *out*-phase components of the wall-normal velocity with respect to the temperature for *a)* full channel flows (CH2) and *b)* open channel flows (OCH2). ——— total; ——— in-phase component; – – – out-phase component.

For any given Fourier mode, it is in general possible to decompose the wall-normal velocity in a *in-* and *out-* phase component with respect to the temperature. For small amplitude gravity waves, a linear analysis predicts a 90-degree phase-shift between the wall-normal velocity and the active scalar (temperature) and therefore a solely *out*-phase component should be expected.

Using complex operators, the in-phase and out-phase components can be defined as:

$$\begin{aligned} v_{IP}(k_x, k_z, y, t) &= \mathrm{Re}(\hat{v}(k_x, k_z, y, t)\hat{\theta 1}^*(k_x, k_z, y, t)), \\ v_{OP}(k_x, k_z, y, t) &= \mathrm{Re}(\hat{v}(k_x, k_z, y, t) i\hat{\theta 1}^*(k_x, k_z, y, t)), \end{aligned} \tag{8}$$

where $(\cdot)^*$ stands for the complex conjugate. The second order momentum v^2_{rms} can be obtained through Parceval's relation equally in spectral space or in physical space, and, using the fact that *in*- and *out*-phase components are perpendicular to each other, it can be split in the two contributions:

$$\begin{aligned} v^2_{rms} = &\iint \overline{v_{IP}(k_x, k_z, y) v^*_{IP}(k_x, k_z, y)} \mathrm{d}k_x \mathrm{d}k_z + \\ &\iint \overline{v_{OP}(k_x, k_z, y) v^*_{OP}(k_x, k_z, y)} \mathrm{d}k_x \mathrm{d}k_z \end{aligned} \tag{9}$$

In Fig. 6, the different contributions are plotted for a stratified full and open channel case. Unstratified cases (not shown) reveal a very similar behaviour to Fig. 6 close to the wall. However, in the central region significant differences arise. The peak of v_{rms} in fig 6*a)* at the centreline was already found both by Armenio & Sarkar (2002) and García-Villalba & del Álamo (2011) who related it to gravity wave activity. The proposed decomposition provides support for this hypothesis, showing that the main contribution comes from the *out* of phase component, *e.g.* the one where gravity waves should be found. Nevertheless, it turns out that in this central region turbulence is weaker but still active, accounting for 10% of the magnitude of v_{rms}. Note that in the outer regions of unstratified cases, the two components contribute with the same amount to the total variance, showing significant differences with Fig. 6. When we turn to open channel cases, an increase of the relative contribution of the *out*-phase component can clearly be seen close to the upper boundary. However, the difference is not as large as in the case of full channel flows, possibly due to the boundary condition which forces both v and θ to zero. A similar conclusion can also be drawn from the probability density function of the angle between the wall-normal velocity and the temperature, which is shown in Fig. 7. Interestingly, the flow can be divided into three regions: close to the wall and at the upper boundary (centreline for the full channel cases) the phase-shift approaches roughly $\pi/2$, whereas in between these two regions a broader peak is attained around $-\pi$, consistent with Komori *et al.* (1983) and McBean & Miyake (1972). Note that the peak in the outer region attains a value of 0.26 for the full channel and around 0.14 for the open channel, indicating that there is a reduced gravity wave activity in the open channel as compared to the full channel.

4. Conclusions

DNSs and LESs of wall-bounded turbulent flows at high stratification have been carried out for both open channel and full channel flows at moderate $Re_\tau = 180, 360$. Following previous studies (Nieuwstadt 2005; Flores & Riley

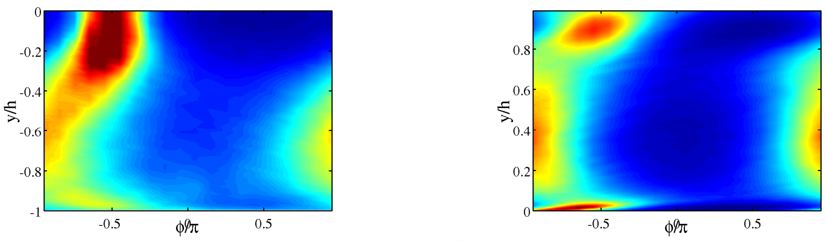

a) *b)*

FIGURE 7. Magnitude-weighted PDFs of the phase shift between the Fourier coefficients of temperature and wall-normal velocity. *a)* full channel flows (CH2); *b)* open channel flows (OCH2). Colour from 0 (*blue*) to 0.14 (*red*)

2010), such flows can be regarded as a model for the atmospheric boundary layer. First of all, the turbulence collapse has been analysed. In agreement with previous works (Nieuwstadt 2005; Flores & Riley 2010), for the considered Re_τ re-laminarization of the flow occurs when the ratio of the channel height with the Monin-Obukhov length is around 1.2. However, as pointed out by Flores & Riley (2010), the ratio at which re-laminarization is observed depends on the Reynold number and the condition cannot be used as a general criterion for the turbulence collapse.

We have analysed the structures that develop in this stably stratified regime. The structures close to the wall seem to be unaffected by the presence of the stratification and near-wall structures for the unstratified and stratified cases fall on top of each other. As we move further from the wall, the stratification starts to play an important role and the flow structures significantly differ. Outer layer structures become narrower as the stratification increases and the comparison between the unstratified and the stratified case with $h/L = 1.2$ shows a ratio between their spanwise width of about 3. Nevertheless, their streamwise length is hardly changed.

In order to characterize wave-like structures, a decomposition able to separate turbulent and wave contribution has been proposed. In agreement with the findings of García-Villalba & del Álamo (2011), wave-like motions are mainly expected in the centre of the channel, and they localize in spectral space around wavelength $\lambda_x \approx 2-3$, $\lambda_z \approx \infty$, *i.e.* structures which are extremely long in the spanwise direction. Gravity waves were observed in open channel cases as well, however their magnitude attained smaller values, possibly due to the presence of the boundary condition. Wall-normal correlation analysis has been shown to be able to lead to similar results, showing both the appearance of gravity waves as well as the narrowing of the outer wall-normal-well-correlated structures as the stratification was increased.

Acknoledgments

Computer time provided by SNIC (Swedish National Infrastructure for Computing) is gratefully acknowledged.

References

Armenio, V. & Sarkar, S. 2002 An investigation of stably stratified turbulent channel flow using large-eddy simulation. *Journal of Fluid Mechanics* **459**, 1–42.

Chevalier, M., Schlatter, P., Lundbladh, A. & Henningson, D. S. 2007 simson - A Pseudo-Spectral Solver for Incompressible Boundary Layer Flows. *Tech. Rep.*. KTH Mechanics, Stockholm, Sweden, TRITA-MEK 2007:07.

Deusebio, E. 2010 An open channel version of simson. *Tech. Rep.*. KTH Mechanics, Stockholm, Sweden.

Flores, O. & Jiménez, J. 2006 Effect of wall-boundary disturbances on turbulent channel flows. *Journal of Fluid Mechanics* **566**, 357–376.

Flores, O. & Riley, J. J. 2010 Analysis of turbulence collapse in stably stratified surface layers using direct numerical simulation. *Boundary-Layer Meteorology* **129** (2), 241–259.

García-Villalba, M. & del Álamo, J. C. 2011 Turbulence modification by stable stratification in channel flow. *Physics of Fluids* **23** (4), 045104.

Germano, M., Piomelli, U., Moin, P. & Cabot, W. H. 1991 A dynamic subgrid-scale eddy viscosity model. *Physics of Fluids* **3** (7), 1760–1765.

Hoyas, S. & Jiménez, J. 2006 Scaling of the velocity fluctuations in turbulent channels up to $Re_\tau = 2003$. *Physics of Fluids* **18** (1), 011702.

Jiménez, J. 1998 The largest scales of turbulence. In *Annual Research Briefs*. Center for Turbulence Research, Standford.

Kim, J., Moin, P. & Moser, R. 1987 Turbulence statistics in fully developed channel flow at low Reynolds number. *Journal of Fluid Mechanics* **177**, 133–166.

Komori, S., Ueda, H., Ogino, F. & Mizushina, T. 1983 Turbulence structure in stably stratified open-channel flow. *Journal of Fluid Mechanics* **130**, 13–26.

McBean, G. A. & Miyake, M. 1972 Turbulent transfer mechanisms in the atmospheric surface layer. *Quarterly Journal of the Royal Meteorological Society* **98** (416), 383–398.

Nieuwstadt, F. T. M. 2005 Direct numerical simulation of stable channel flow at large stability. *Boundary-Layer Meteorology* **116**, 277–299.

Örlü, R. & Schlatter, P. 2011 On the fluctuating wall-shear stress in zero pressure-gradient turbulent boundary layer flows. *Physics of Fluids* **23** (2), 021704.

Paper 4

4

The open-channel version of SIMSON

By Enrico Deusebio

Linné Flow Centre, KTH Mechanics
SE-100 44 Stockholm, Sweden

Technical Report, 2010

In the following we present an improved modification of SIMSON (a pseudo-Spectral solver for IncoMpressible bOuNdary layer flows) for dealing with open-channel flows. For such class of flows, the Gauss-Lobatto grid in the wall-normal direction leads to a clustering of points at the free boundary. Apart from being superfluous, this clustering may also pose a stronger restriction to the CFL condition for a stable numerical scheme. Motivated by the fact that an open-channel flow corresponds to a full channel which is symmetric around the centreline, we modify the numerical scheme such that only one parity of the Chebyshev polynomials are used in the solution algorithm. Note that in such a way the clustering of points at the free surface (now the centreline) is avoided. For the streamwise and spanwise components only even Chebyshev polynomials are used, whereas for the wall-normal component and the additional scalars only odd Chebyshev polynomials are used. In order to guarantee the speed-up of the code, an alternative formulation of the Fast Fourier/Chebyshev transforms which accounts for the symmetry is presented. Since we aim at carrying out direct numerical simulations at reasonably large Reynolds numbers, the modifications have been implemented both in a one-dimensional and two-dimensional parallelization strategy. Using the improved discretization, we show that the wall-normal resolution can be reduced, leading to an overall speed-up of the code. Moreover, a new CFL condition which accounts for the presence of an active scalar as well as fringe regions which avoids spurious reflections of gravity waves have also been implemented.

---

1. Introduction

Open channel flow has been used as a model in order to understand and study turbulence in oceanic and atmospheric flows which are bounded by one solid wall (Nieuwstadt 2005; Handler *et al.* 1999). At the lower boundary, the no-slip condition $u = v = w = 0$ is imposed while at the upper boundary the open-channel condition ensures that the flow is shear free and no fluid leaves the domain, *i.e.* $v = \partial u/\partial y = \partial w/\partial y = 0$. Here, u,v and w are the streamwise, wall-normal and spanwise velocities, respectively. The flow is driven by a constant pressure gradient which is balanced by the viscous stress, τ_p, at the lower wall. The Poiseuille solution satisfies the open-channel condition at the centreline, and therefore for laminar cases the open channel flow resembles the half laminar channel flow. However, for turbulent flows this resemblance is lost and the open channel flow may rather be seen as one side of a channel which is symmetric around the centreline. Handler *et al.* (1999) have employed the open channel condition in order to study the behaviour of a passive scalar close to the free shear boundary, while Nieuwstadt (2005) has used it in direct numerical simulations of stable stratified turbulence.

The present report deals with the modifications that have been implemented on an existing Navier-Stokes solver, called SIMSON, in order to improve the numerical scheme for open-channel flow simulations. SIMSON is a very efficient pseudo-spectral code that has been developed and used over almost twenty years at KTH Mechanics, both for direct numerical simulations (DNS) and large-eddy simulations (LES). For further details we refer to Chevalier *et al.* (2007) and references therein.

The modifications mainly address two aspects of the code. First, the wall-normal discretization has been modified in order to avoid the clustering of points at the upper boundary. In fact, the code relies on a Gauss-Lobatto grid along y which is optimal for channels with solid walls at both boundaries but not for the open channel. Secondly, some features needed to handle and deal with stratified flows, namely a modified CFL condition and damping regions for internal waves, have also been developed and implemented.

The report is organized as follow: in section 2, the open-channel version of SIMSON is described. Validation and results are presented. In section 3, the features developed in the code for stratified flows are summarized.

2. The open-channel version of SIMSON

Although the open channel boundary condition is already present in SIMSON (Chevalier *et al.* 2007), its current implementation is not optimal. The code uses a Fourier decomposition along the streamsiwse coordinate x and the spanwise coordinate z, whereas Chebyshev polynomials are used along the wall-normal coordinate y. In order to efficiently implement a solver based on these methods, the y discretization requires a Gauss-Lobatto grid, *i.e.* points distributed as:

$$y_j/L = \cos\left(\pi\frac{j-1}{N-1}\right) \qquad\qquad j = 1, \cdots, N. \tag{1}$$

Such a grid leads to an accumulation of points close to the upper and lower boundaries and a coarser grid in the middle. Whereas the narrow spacing at the lower boundary is preferable due to the sharp velocity gradients at the wall, it is not needed at the free-shear boundary, where a smoother solution is attained. It is possible to distort such a grid through mapping transformations as described by Laurien & Kleiser (1989). However, this breaks the tridiagonal structure of the matrix which arises when solving Poisson equations in a Gauss-Lobatto grid, leading to significant reductions of the numerical efficiency.

In order to allow for coarser grid spacing at the upper boundary without any degradation of the performances, a different approach has been followed here. As noted above, the open channel with a stress free upper boundary can be regarded as a full symmetric channel flow, where we only retain the upper or lower part. As pointed out by Corral & Jiménez (1995), one can use only half of the Chebyshev collocation points

$$y_j/L = \cos\left(\frac{\pi}{2}\frac{j-1}{N-1}\right) \qquad j = 1, \cdots, N. \tag{2}$$

The equations can be solved just for the odd/even Chebyshev polynomials, depending on the parity of the considered variable. In such a way, a better distribution of grid points is achieved which is narrower at the wall and coarser in the free-stream. In order to resolve the turbulent structures close to the wall, ten points within the region $y < 10\nu/u_\tau$ are required. Here, u_τ represents the friction velocity defined as $u_\tau = \sqrt{\tau_w/\rho}$, with τ_w being the shear stress at the wall and ρ the density, and ν represents the kinematic viscosity. On the other hand, in the outer region a spacing of the order of the Kolmogorov length,

$$\eta = \left(\frac{\nu^3}{\varepsilon}\right)^{1/4}, \tag{3}$$

is required to resolve the outer turbulent structures. Here, ε refers to the kinetic energy dissipation.

The implementation of such an algorithm in SIMSON mainly involves the implementation of an efficient Fast Chebyshev Transform which relies just on half of the grid points[1], and the implementation of a solution algorithm which accounts for a particular symmetry.

In section 2.1, the symmetric formulation of the problem is summarized, while section 2.2 is devoted to the description of the symmetric fast Chebyshev transforms (and their antisymmetric counterpart). In section 2.3 the main modifications introduced in the code are discussed. Finally, the validation is presented in section 2.4.

2.1. *Symmetries*

Let x,y and z be the axes oriented towards the streamwise, wall-normal and spanwise direction respectively. The velocities u,v and w are defined accordingly. In the wall-normal direction, the computational domain including the full symmetric channel spans from $y = -h$ to $y = h$ with the symmetry plane at $y = 0$. Since we will study the stratified open channel flow we will include an active scalar equation. We consider the incompressible Navier-Stokes equations within the Boussinesq approximation, which can be written as

$$\frac{\partial u_i}{\partial t} = -\frac{\partial p}{\partial x_i} + \epsilon_{ijk} u_j \omega_k - \frac{\partial}{\partial x_i}\left(\frac{1}{2}u_j u_j\right) + \frac{1}{Re}\nabla^2 u_i + Ri\theta\delta_{i2} + F_i \tag{4}$$

[1] and a Fast Inverse Chebyshev Transform which relies just on half modes - the even or odd ones

$$\frac{\partial u_i}{\partial x_i} = 0, \tag{5}$$

where the active scalar θ is supposed to obey a diffusion equation

$$\frac{\partial \theta}{\partial t} + u_j \frac{\partial \theta}{\partial x_j} = \frac{1}{Pe} \nabla^2 \theta, \tag{6}$$

where ϵ_{ijk} is the alternating tensor and F_i is the generic volume force along the i-axis. The equations have been made dimensionless using the centreline velocity U_{cl}, the channel height h and the temperature difference $\Delta T = \theta_{upper} - \theta_{lower}$. The three dimensionless quantities that arise are the Reynolds number

$$Re = \frac{U_{cl} h}{\nu}, \tag{7}$$

the Richardson number

$$Ri = \frac{g \alpha \Delta T h}{U_{cl}^2} \tag{8}$$

and the Peclet number

$$Pe = \frac{U_{cl} h}{\kappa} = Re Pr, \tag{9}$$

where κ is the thermal diffusivity and $Pr = \nu/\kappa$ the Prandtl number, g the gravitational acceleration and α the (thermal) compressibility coefficient.

Following Chevalier *et al.* (2007), the momentum equation (4) can be reduced to a form where the only physical unknowns are the wall-normal velocity v and the wall-normal vorticity ω,

$$\left[\frac{\partial}{\partial t} - \frac{1}{Re}\nabla^2\right] \nabla^2 v = \left(\frac{\partial^2}{\partial x^2} + \frac{\partial^2}{\partial z^2}\right) H_2 - \frac{\partial}{\partial y}\left[\frac{\partial H_1}{\partial x} + \frac{\partial H_3}{\partial z}\right] \tag{10}$$

$$\left[\frac{\partial}{\partial t} - \frac{1}{Re}\nabla^2\right] \nabla^2 \omega_y = \frac{\partial H_1}{\partial z} - \frac{\partial H_3}{\partial x} \tag{11}$$

with the H_i vector is defined as

$$H_i = \epsilon_{ijk} \omega_j u_k + F_i + Ri \theta \delta_{i2}. \tag{12}$$

For a channel which is symmetric around the centreline, we can easily infer that the velocities u and w have to be even functions in y and their Chebyshev expansions contain only even polynomials. From eq. (5), it follows that the wall-normal velocity v has to be odd. The wall-normal vorticity

$$\omega_y = \frac{\partial u}{\partial z} - \frac{\partial w}{\partial x} \tag{13}$$

is even since derivation with respect to x or z does not change the symmetry. On the other hand, derivation in y inverts the parity. The ∇^2 operator does not change the symmetry. Streamwise and spanwise vorticities

$$\omega_x = \frac{\partial w}{\partial y} - \frac{\partial v}{\partial z}, \tag{14}$$

$$\omega_z = \frac{\partial v}{\partial x} - \frac{\partial u}{\partial y}, \tag{15}$$

are therefore odd functions, whereas the non-linear terms

$$H_1 = \omega_y w - \omega_z v, \qquad\qquad H_3 = \omega_x v - \omega_y u, \tag{16}$$

are even and

$$H_2 = \omega_z u - \omega_x w \tag{17}$$

is odd.

From these considerations it follows that the equation for v must be odd whereas the equation for ω_y must be even. Since the buoyancy term appears in the vertical momentum equation, the active scalar (*e.g.* temperature) must be an odd function.

The parity of the variables can be used in order to optimize the code. Since a large amount of the computational time is spent on transforming variables between physical and spectral space, improving the transform algorithms is of primary importance.

Modifications in physical space can be implemented quite easily by extending the computations to only one side of the channel. On the other hand, modifications in spectral space require a more careful analysis. This includes, for instance, the calculation of derivatives, which in the code is made in spectral space according to:

$$\hat{u}_m^{(1)} = \frac{2}{c_m} \sum_{\substack{p=m+1 \\ p+m \text{ odd}}}^{\infty} p\hat{u}_p. \tag{18}$$

where $\hat{u}_p$ and $\hat{u}_p^{(1)}$ represents the Chebyshev p-th coefficient of the variable and its first derivative, respectively. From the expression above it is easy to see that this operation changes the parity of the function: even derivative coefficients are linked to the odd ones and vice-versa. Similar considerations apply to the integration. A new implementation of these subroutines is therefore needed.

The main modification of the code has been made in the subroutine `linearbl` where the Poisson wall-normal equation for each mode is solved. Following the standard procedure outlined in Chevalier *et al.* (2007), the generic function can be decomposed in Fourier modes along x and y according to:

$$\phi(x, y, z, t) = \sum_{\alpha,\beta} \hat{\phi}(\alpha, \beta, y, t) e^{i(\alpha x + \beta z)}, \tag{19}$$

where α and β are the streamwise and spanwise wavenumber respectively. For sake of simplicity, the temperature equation is now dropped. The same considerations that follow can straightforwardly be applied to the scalar without any further complications. Both equations (10) and (11) can be written in a compact form,

$$\frac{\partial}{\partial t}\hat{\phi} = \frac{1}{Re}\left(D^2 - k^2\right)\hat{\phi} - \hat{h}, \tag{20}$$

where $k^2 = \alpha^2 + \beta^2$, $\hat{h}$ is the Fourier component of the nonlinear term. Equation (20) can either be odd or even depending on whether the wall-normal velocity or the wall-normal vorticity is considered. Time discretization of (20) through an explicit Runge-Kutta scheme for the nonlinear part and a Crank Nicolson scheme for the linear part leads to:

$$\left[1 - \frac{a_n + b_n}{2Re}\left(D^2 - k^2\right)\right]\hat{\phi}^{n+1} = \left[1 + \frac{a_n + b_n}{2Re}\left(D^2 - k^2\right)\right]\hat{\phi}^{n} + a_n h^n + b_n h^{n-1}, \tag{21}$$

which can be rewritten as a Poisson equation

$$\left[D^2 - \underbrace{\left(k^2 + \frac{2Re}{a_n + b_n}\right)}_{\lambda}\right]\hat{\phi}^{n+1} = f^n. \tag{22}$$

The structure of the matrix is particularly simple with only three non-zero diagonals when spectral methods based on Chebyshev expansion are applied to Gauss-Lobatto grids, allowing for very efficient algorithms. Depending on which variable is considered, $\hat{\phi}$ can be expressed with either odd Chebyshev polynomials

$$\hat{\phi} = \sum_{j=0}^{(N-1)/2} \hat{a}_{2k+1} T_{2k+1}, \tag{23}$$

or even Chebyshev polynomials

$$\hat{\phi} = \sum_{j=0}^{(N+1)/2} \hat{a}_{2k} T_{2k}. \tag{24}$$

The number of odd polynomial expansions is one less than the number of even ones, reflecting the fact that odd variable are zero at the centreline. Introducing the above *ansatz* and using the orthogonality of Chebyshev polynomials with respect to the inner product

$$\langle f\,,\, g\rangle = \int_{-1}^{1} f\, g\, \frac{1}{\sqrt{1-y^2}} \mathrm{d}y, \tag{25}$$

we arrive at the simple relation

$$\hat{a}_k^{(2)} - \lambda \hat{a}_k = \hat{f}_k, \tag{26}$$

where $\hat{a}_k^{(2)}$ is the Chebyshev coefficient of the second derivative of the function, *i.e.*

$$\phi'' = \sum \hat{a}_k T_k'' = \sum \hat{a}_k^{(2)} T_k. \tag{27}$$

It can be shown that $\hat{a}_k^{(2)}$ and $\hat{a}_k$ are related as (Canuto *et al.* 1988)

$$\hat{a}_k^{(2)} = \frac{1}{c_k} \sum_{\substack{p = k+2 \\ p+k \text{ even}}}^{\infty} p\left(p^2 - k^2\right)\hat{a}_p. \tag{28}$$

Eq.(28) shows that even (odd) coefficients of the second derivatives are determined only by even (odd) coefficients of the function itself. The systems for the odd and even Chebyshev coefficients decouple and if parity is considered only one system needs to be solved. Using the identity (28) and after making some rearrangements as outlined in Canuto *et al.* (1988), it is possible to reduce (26) to a tridiagonal system:

$$-\frac{c_{j-2}\nu}{4j\,(j-a)}\hat{a}_{j-2} + \left(1 + \frac{\nu\beta_j}{2\,(j^2-1)}\right)\hat{a}_j - \frac{\nu}{4j\,(j+1)}\hat{a}_{j+2}$$
$$= \frac{c_{j-2}}{4j\,(j-a)}\hat{f}_{j-2} - \frac{\beta_j}{2\,(j^2-1)}\hat{f}_j + \frac{\beta_{j+2}}{4j\,(j+1)}\hat{f}_{j+2}, \qquad j = 2, \ldots, N_y, \tag{29}$$

where

$$\beta_j = \begin{cases} 1, & 0 \le j \le N_y - 2 \\ 0, & j > N_y - 2 \end{cases} \qquad c_j = \begin{cases} 2, & j = 0 \\ 1, & j > 0 \end{cases}. \tag{30}$$

In order to solve eq. (11) and (10), appropriate boundary conditions have to be imposed. A few important modifications of the algorithm are introduced at this stage, reflecting the fact that when a given parity is considered, the freedom on choosing boundary conditions at both walls is obviously lost.

In the original version of SIMSON, the boundary conditions are imposed through a rather efficient and flexible algorithm, which relies on the solution of both homogeneous equations with inhomogeneous Dirichlet boundary conditions and inhomogeneous equations with homogeneous boundary conditions. Explicitly, for each symmetry, the following systems are solved for the wall-normal velocity:

$$\left(D^2 - \lambda^2\right)\phi_p^{n+1} = f^{n+1} \qquad \text{with } \phi_p(y_L) = 0 \tag{31a}$$
$$\left(D^2 - \lambda^2\right)v_p^{n+1} = \phi_p^{n+1} \qquad \text{with } v_p^{n+1}(y_L) = 0 \tag{31b}$$
$$\left(D^2 - \lambda^2\right)\phi_h^{n+1} = 0 \qquad \text{with } \phi_h(y_L) = 1 \tag{31c}$$
$$\left(D^2 - \lambda^2\right)v_{ha}^{n+1} = \phi_h^{n+1} \qquad \text{with } v_{ha}^{n+1}(y_L) = 0 \tag{31d}$$
$$\left(D^2 - \lambda^2\right)v_{hb}^{n+1} = 0 \qquad \text{with } v_{hb}^{n+1}(y_L) = 1 \tag{31e}$$

and for the wall-normal vorticity

$$\left(D^2 - \lambda^2\right)\omega_p^{n+1} = f_\omega^{n+1} \qquad \text{with } \omega_p(y_L) = 0 \tag{32a}$$
$$\left(D^2 - \lambda^2\right)\omega_h^{n+1} = 0 \qquad \text{with } \omega_h(y_L) = 1 \tag{32b}$$

For each symmetry, the solutions of the Dirichlet problems are then superimposed such that the conditions at the boundaries are satisfied. Note that even if the boundary conditions at the lower wall are homogeneous (no-slip condition), the partial symmetries could be inhomogeneous there and thus the functions v_{hb} and ω_h may be different from zero. However, when both symmetries are summed up, the homogeneity is recovered. More details can be found in Chevalier *et al.* (2007).

When symmetric problems are considered, some operations can be avoided, leading to an increase of the speed of the code. For a given variable, we can avoid to compute a certain symmetry and also skip some of the equations. When a symmetry is considered and homogeneous conditions are applied at the lower boundary (no-slip condition), the solution cannot contain functions such v_{hb} and ω_h since this would lead to inhomogeneity at the walls. In fact, v_{hb} and ω_h do not sum with the other parity. For these reason, we can avoid to compute them. The solution of the system for v and ω_y, can then be simply written as:

$$\hat{v} = \hat{v_p} + C_1 \hat{v_{ha}} \tag{33}$$

$$\hat{\omega_y} = \hat{\omega_{y_p}} \tag{34}$$

where the constant C_1 has to be determined in order to satisfy the continuity at the boundary $\partial v/\partial y = 0$.

Particular attention is needed for the wavenumber ($\alpha = 0$, $\beta = 0$) for which the equations for u and w cannot be inverted. In this case, u and w are directly obtained as the solutions of four Dirichlet problems, as equations (32). However, also in this case, one does not need to solve for the homogeneous equations with inhomogeneous boundary conditions.

2.1.1. *The pressure*

It is worth noticing that the solution procedure which relies on equations (10) and (11) does not require the pressure to be computed. However, the pressure can still be found through the solution of an elliptic Poisson equation

$$\nabla^2 (p + E) = \frac{\partial H_i}{\partial x_i} \tag{35}$$

where E is the total kinetic energy $\left(u^2 + v^2 + w^2\right)/2$ (see Chevalier *et al.* 2007). Computation of the pressure is sometimes desirable, for example when one would like to compute energy fluxes.

An adopted solution algorithm for the pressure which accounts for the symmetries along the wall-normal direction has also been implemented. Considering the parities of the variable discussed above, it follows that the elliptic equation (35) is symmetric around the centreline. Therefore, the pressure has to be even. The boundary conditions at the upper and lower walls can be derived from the momentum equation along y:

$$\frac{\partial p}{\partial y} = -\frac{\partial v}{\partial t} + \frac{1}{Re}\frac{\partial^2 v}{\partial x_j \partial x_j} - u_j \frac{\partial v}{\partial x_j} + Ri\theta + F_2 \tag{36}$$

The Neumann boundary condition leads to a system which is slightly different from the ones considered when Dirichlet boundary conditions are applied and therefore different subroutines are called in the code. At the lower boundary (36) reduces to:

$$\frac{\partial p}{\partial y} = Ri\theta + F_2. \tag{37}$$

At the centreline equation (37) vanishes because of the symmetry. This can be seen in (36) by rewriting the non linear term as:

$$u_j \frac{\partial v}{\partial x_j} = u\omega_z - w\omega_x + \frac{\partial E}{\partial y} \tag{38}$$

and noting that all the terms vanish because of symmetry (ω_x, ω_z and v are odd whereas E is even).

2.2. *The fast symmetric Chebyshev transform*

Pseudo-spectral codes need to continually switch from spectral to physical space which covers a substantial part of the total computational time. Therefore, a fast and efficient Chebyshev transform has to be implemented which makes use of only one half of points.

To implement the Chebyshev transform for symmetric series one needs to consider the odd and even cases separately. Whereas the even transform can easily be reduced to a normal Chebyshev transform on half of the domain, the odd one requires a more careful analysis.

2.2.1. *The forward symmetrical transform*

The Chebyshev transform of a series $u(x)$ is commonly defined as

$$a_k = \langle u\,,\,T_k\rangle = \int_{-1}^{1} u(x)T_k(x)\frac{1}{\sqrt{1-x^2}}\mathrm{d}x \tag{39}$$

where $T_k(x)$ is the k-th Chebyshev polynomial

$$T_k(x) = \cos\left(k\arccos x\right) \qquad\qquad \text{with } -1 \le x \le 1. \tag{40}$$

Through the mapping $\theta = \arccos(x) - \pi/2$, eq. (39) can be reduced to

$$a_k = \int_{-\pi/2}^{\pi/2} \tilde{u}(\theta)\cos\left(k\left(\theta + \pi/2\right)\right)\mathrm{d}\theta, \tag{41}$$

showing the similarity with the Fourier transform which would be recovered when the limits of the integral are replaced by $[-\pi, \pi]$. If Gauss-Lobatto grids are used, the similarity extends also to the discrete form and efficient algorithms for computing the DFT can directly be applied. If u is symmetric (antisymmetric) around $x = 0$, also the function $\tilde{u}(\theta) = u(x) = u(\cos(\theta - \pi/2))$ is symmetric (antisymmetric) around $\theta = 0$. The following expressions can be derived for an even or an odd k

$$a_k = (-1)^{\frac{k}{2}} \int_{-\pi/2}^{\pi/2} \tilde{u}(\theta)\cos\left(k\theta\right)\mathrm{d}\theta \qquad\qquad \text{for k even,} \tag{42}$$

$$a_k = (-1)^{\frac{k+1}{2}} \int_{-\pi/2}^{\pi/2} \tilde{u}(\theta)\sin\left(k\theta\right)\mathrm{d}\theta \qquad\qquad \text{for k odd.} \tag{43}$$

If u is symmetric, just even modes are non-zero, whereas antisymmetric u have only non-zero odd modes.

Let us first consider the symmetric case. Putting $k = 2\tilde{k}$, with $\tilde{k} = 0, \dots,$ $N/2+1$ in (39) and mapping with the transformation $\theta = \arccos(x)$, we obtain

$$\begin{aligned} a_{\tilde{k}} &= \int_0^{\pi} \tilde{u}(\theta) \cos\left(2\tilde{k}\theta\right) \mathrm{d}\theta = \\ &= 2\int_0^{\pi/2} \tilde{u}(\theta) \cos\left(2\tilde{k}\theta\right) \mathrm{d}\theta = \\ &= \int_0^{\pi} \tilde{u}(\tilde{\theta}) \cos\left(\tilde{k}\tilde{\theta}\right) \mathrm{d}\tilde{\theta} \end{aligned} \tag{44}$$

where $\tilde{\theta} = 2\theta$, have been used. The even transform can thus be reduced to a Chebyshev transform on half of the domain, using just half of the points.

However, for odd modes the integral cannot be reduced to a Chebyshev transform as straightforwardly. Even Chebyshev polynomials are, in fact, “conventional“ Chebyshev polynomials when mapped on half of the domain. Unfortunately, this correspondence does not hold for the odd ones. In this case, however, we can use the recurrence relationship between Chebyshev polynomials

$$T_{k+1} = 2xT_k - T_{k-1} \tag{45}$$

in order to get an expression which involves just even modes. Using (45) the k-th coefficient, given by (39), can be rewritten as:

$$\begin{aligned} a_{k+1} &= \int_{-1}^{1} u(x) T_{k+1} \frac{1}{\sqrt{1-x^2}} dx \\ &= \int_{-1}^{1} u(x) \left(2xT_k - T_{k-1}\right) \frac{1}{\sqrt{1-x^2}} \mathrm{d}x \\ &= 2\int_{-1}^{1} u(x) x T_k \frac{1}{\sqrt{1-x^2}} \mathrm{d}x - \int_{-1}^{1} u(x) T_{k-1} \frac{1}{\sqrt{1-x^2}} \mathrm{d}x \\ &= 2\int_{-1}^{1} u(x) x T_k \frac{1}{\sqrt{1-x^2}} \mathrm{d}x - a_{k-1} \end{aligned} \tag{46}$$

Relation (46) gives a recurrence relationship for the coefficients of the expansion. Note that if the function $u(x)$ is odd, the function $u(x)x$ is even and (44) can be used in order to efficiently computed a_{k+1}. The first mode needs particular attention:

$$a_1 = \int_{-1}^{1} u(x) x \frac{1}{\sqrt{1-x^2}} dx = \frac{1}{2}\int_{-1}^{1} 2u(x) x \frac{1}{\sqrt{1-x^2}} dx \tag{47}$$

and can thus be reduced to the expression (46) by putting $a_{k-1} = 0$ and normalizing by 2.

2.2.2. *The inverse symmetric transform*

The inverse transform is obtained through the expansion formula

$$u(x) = \sum_{0}^{N_y} a_k T_k = \sum_{0}^{N_y} a_k \cos\left(k \arccos(x)\right) \tag{48}$$

Assuming a Gauss-Lobatto grid and using the fact that just the even coefficients are non-zero, the expression (48) can be rewritten as:

$$\begin{aligned} u(x_j) &= \sum_{0}^{N_y} a_k \cos\left(k \arccos(x_j)\right) \\ &= \sum_{0}^{N_y/2} a_{\tilde{k}} \cos\left(2\tilde{k} \arccos(x_j)\right) \\ &= \sum_{0}^{N_y/2} a_{\tilde{k}} \cos\left(2\tilde{k} \frac{j\pi}{N_y}\right) \\ &= \sum_{0}^{N^*} a_{\tilde{k}} \cos\left(2\tilde{k} \frac{j\pi}{N^*}\right). \end{aligned} \tag{49}$$

Once again, we note that this expression has exactly the same form of (48), where N_y is replaced by $N^* = N_y/2$.

To derive the odd inverse Chebyshev transform we start from (48) with only non-zero odd coefficients:

$$\begin{aligned} u(x_j) &= \sum_{k=0}^{N_y/2-1} a_{2\tilde{k}+1} T_{2\tilde{k}+1} = \\ &= \sum_{k=0}^{N_y/2-1} a_{2\tilde{k}+1} \left(T_{2\tilde{k}} + T_{2\tilde{k}+2}\right) \frac{1}{2x}, \end{aligned} \tag{50}$$

where the recurrence relation (45) has been used. This can be shortly rewritten as

$$u(x_j) = \left[\sum_{k=0}^{N_y/2} c_{2k} T_{2k}\right] \frac{1}{2x} \tag{51}$$

where the coefficient c_{2k} is defined as:

$$c_{2k} = \begin{cases} a_1 & k = 0 \\ a_{2k+1} + a_{2k-1} & k = 1, \cdots, N_y/2 - 1 \\ a_{(N_y-1)/2} & k = N_y/2 \end{cases} \tag{52}$$

Note that the expression above has the same form as the symmetric inverse Chebyshev transform, eq. (49), and can be easily computed.

2.2.3. *Speed-up*

Since the procedures outlined in subsection 2.2.1 and in subsection 2.2.2 make use of remapped full Chebyshev transform, very efficient FFT packages can be used, as for instance `FFTw` or `VECFFT`. Even transforms do not require any pre/post processing and therefore the speed-up scales as $2\log N/\log N/2$ when compared to full transforms. Odd transforms require some pre- and post-processing, both in the forward and backward transforms.

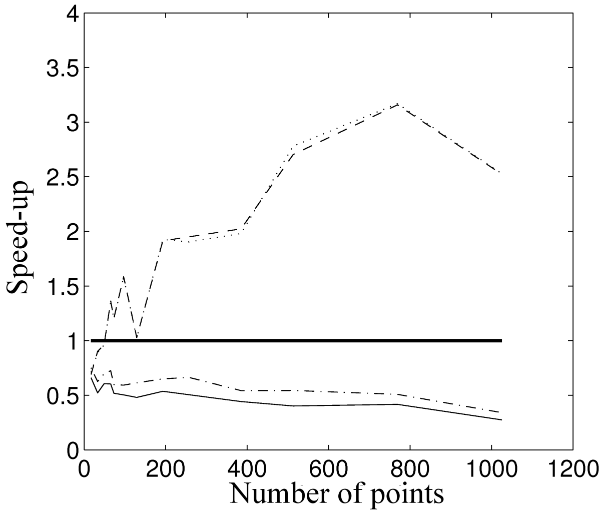

FIGURE 1. Speed-up achieved using symmetrical and anti-symmetrical transforms, compared with the full Fast Chebyshev Transform (from VECFFT). The curves are normalized with the time required by the full Fast Chebyshev Transform. ——— Full Fast Chebyshev Transform; ——— Symmetric Fast Chebyshev Transform (even); –·– Symmetric Fast Chebyshev Transform (odd); - - - Matrix Symmetric Chebyshev Transfrom (even); ········ Matrix Symmetric Chebyshev Transfrom (odd)

In order to test the new implementations, symmetric and antisymmetric series have been transformed back and forth with both the new algorithm and the full one. A comparison of the time spent on the transforms is shown in figure 1 for different number of points. The direct transform computed through an highly optimized matrix-matrix product (using the **BLAS** package) is also shown. In the latter case, the operations are performed more efficiently, optimizing the cache memory management, and, for low numbers of points, such a strategy can actually be faster than FFT algorithms. However, as figure 1 shows, this is true for very small number of points. On the other hand, the symmetric Chebyshev transform becomes faster as the number of points increases. As expected, the anti-symmetric transform is slightly slower since pre- and post- processing are required. A rough estimate of the number of operations can be obtained, both for even and odd symmetries:

$$\mathrm{it}_{sym} \sim \frac{N}{2} \log \frac{N}{2}, \tag{53}$$

$$\mathrm{it}_{asym} \sim \frac{N}{2} \left(2 + \log \frac{N}{2} \right). \tag{54}$$

Note that the curves in figure 1 are not monotonic since the `VECFFT` factorization can involve subsequence of 2,3 or 5 elements and depending on the number of points slightly different results can be obtained.

2.3. *Changes in SIMSON*

The code has been optimized in order to handle symmetric channel flow efficiently, reducing both computational and storage costs. While the computational cost can be reduced by modifying the incompressible solver, namely `bla`, a reduction of the storage costs also requires modifications of programs for pre- and post- processing. In order to modify the existing codes as less as possible, the data processing is done in the usual way on the full symmetric channel and the main modifications occurs just for the I/O operations where the lower part of the channel is either mapped back or eliminated.

In `bls` (the code which generates the initial velocity fields), a new feature has been added which enforces symmetries around the centreline within the flow. The half channel is then stored. The program which allow visualizations of the flowfield, `rit` , has also been modified in order to handle symmetric flow fields. It is worth mentioning that the flow fields carry information about the y symmetry, and they are therefore not fully compatible with the previous version of `SIMSON`. Nevertheless, compatibility of the current version with the previous ones has been assessed, *i.e.* `rit` can still read old version files.

The main modifications occur in the solver `bla`. As shown by Li (2009), the time step is mainly spent in two subroutines: `nonlinbl` and `linearbl`. The former calculates the nonlinear term in physical space for a y-constant plane $(x - z)$: a `do` cycle then iterates it over the whole channel. This structure leads to straightforward modifications of the code. The upper limit of the `do` cycle is chosen such that only half of the channel is computed. The upper limit `nypp` is therefore replaced by the following expression

$$\frac{N_y}{(1 + nfysym)xnproc} + \min(nproc, 2) - 1 + nfysym, \tag{55}$$

where parallel communication protocols, for shared memory parallel machines (OpenMP) and distributed memory parallel machines (MPI), can be either used. Statistics are computed in physical space in a similar manner as in `nonlinbl`, and can therefore be optimized in the same way.

On the other hand, `linearbl` requires a more careful analysis. Each call of this subroutine solves the wall-normal Poisson equation for the Fourier modes with a constant β. A `do` cycle then iterates over the spanwise wave-numbers. In the original code, even though odd and even modes are decoupled, as (29) shows, the even and odd systems are built (with `setmatchr`) and solved (with `trid`) together. However, if an overall speed-up is to be obtained, a new subroutine which solve each parity separately is to be written. Note that such an implementation can still be used when symmetric cases are not considered. In this case, the Poisson solver restricted to only one parity needs to be called twice, once for the even coefficients and once for the odd coefficients.

The computation of the solution of the homogeneous equations with inhomogeneous boundary conditions, not needed in symmetric cases, can be easily avoided.

2.3.1. *Parallelization*

`SIMSON` currently supports parallel algorithms which use protocols both for shared (OpenMP) and distributed (MPI) memory. The main subroutines that have been parallelized are the ones where most of the computational time is spent: `nonlinbl` and `linearbl`. When distributed memory are considered, the Fourier modes on x and z are distributed among the different processors. Thus, data repartition takes place on x and z but not on y; *i.e.* each mode is completely stored in a given processor. However, communication is needed whenever transforms to/from physical and spectral space are computed, *i.e.* in `nonlinbl`, since they require for a given y location the whole $x - z$ plane.

Depending on the size of the problem two different strategies are possible: the so-called 1D and 2D parallelization. The former splits the data in stripes along x, each stripe for each processor. However, if the number of processors is larger than the modes along z, such a partition cannot be used and a better strategy is to divide the $x - z$ plane into squares; *i.e.* the 2D parallelization. Note that whereas the former requires communication only along z, the latter requires communication along both x and z. For further details on the parallelization, please refer to Li (2009).

Since the open-channel code aims at fully-resolved numerical simulations of turbulent stratified flows, parallelization is crucial and the open-channel code can support both 1D and 2D parallelization for distributed memory machines as well as the OpenMP protocol for shared memory machines. Parallel tests have been made on massively parallel machines such as the SNIC systems Neolith and Lucidor. Binary agreement, with and without parallelization, confirms the assessed reliability.

2.4. *Validation*

2.4.1. *Orr-Sommerfeld modes*

In order to validate the code, the temporal evolution of modal perturbations is analysed. Both two- and three-dimensional eigenfunctions of the Orr-Sommerfeld operator are introduced as initial conditions. Their amplification or decay rate is then computed and compared with the solution of the linear eigenvalue problem. It is worth noticing that for the Reynolds number under consideration, $Re = 6000$, the most unstable mode, the so-called Tollmien-Schlichting waves (TS), is anti-symmetric in y with respect to the wall-normal direction and they are therefore not suitable for our test. For the two-dimensional case, the Orr-Sommerfeld system with $\alpha = 1$ and $\beta = 0$ was solved and the least stable even mode was selected. For the three-dimensional case, we considered $\alpha = 1$ and $\beta = 2$. The shape of the eigenfunctions is shown in figure 2*a)* and 2*b)* for the two- and three-dimensional case, respectively. The linear calculation were made with an Orr-Sommerfel solver developed by Philipp Schlatter, at the Institute of Fluid Dynamics, ETH Zurich and the imaginary part of the respective eigenvalues describing the temporal growth/decay can be found in table 2.4.1.

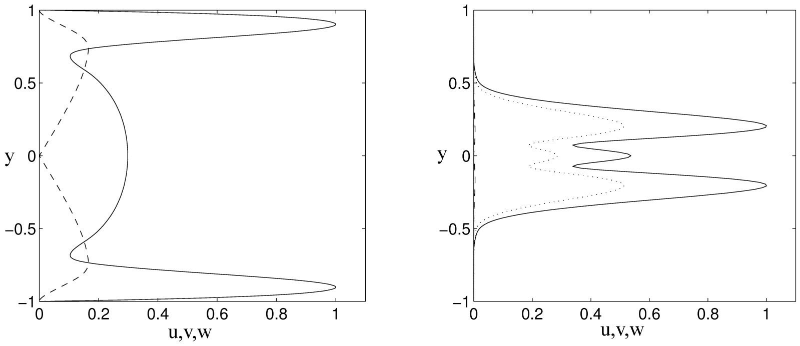

FIGURE 2. Shape of the eigenfunction as function of y, both for the two-dimensional case ($\alpha = 1,\beta = 0$) and three-dimensional one ($\alpha = 1,\beta = 2$). ——— streamwise component u; - - - wall-normal component v; ········ spanwise component w.

The initial conditions were then obtained by superimposing the selected modes to the parabolic profile. The amplitude of the eigenmodes A_e was chosen as small as $A_e = 0.001U_{cl}$, in order to make non-linear interactions negligible and allow the comparison with the linear analysis. The simulations were then run for 100 time units $\tau = h/U$.

Figure 3 shows the evolution of the disturbance in time. The straight line in the logarithmic plot clearly shows the exponentially-decaying behaviour

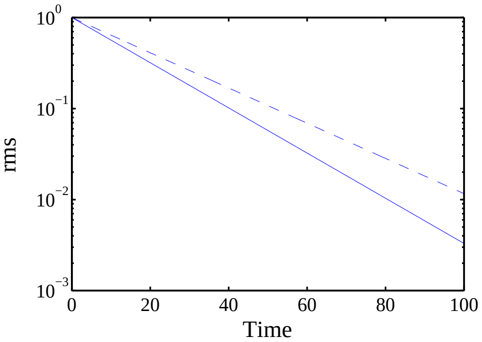

FIGURE 3. Evolution of the eigenfunction amplitudes. Note that a clear exponentially decaying behaviour can be seen throughout the all simulations. ——— Two-dimensional mode; - - - Three-dimensional mode.

Case	Linear calculations	Simulation
2D	$-0.571481510 \cdot 10^{-1}$	$-0.57145599768035 \cdot 10^{-1}$
3D	$-0.445527027 \cdot 10^{-1}$	$-0.44555041095550 \cdot 10^{-1}$

TABLE 1. Decaying rate for the most unstable two and three-dimensional odd (respect to v) eigenfunction at $Re = 6000$. 2-dimensional with ($\alpha = 1$,$\beta = 0$); 3-dimensional with ($\alpha = 1$,$\beta = 2$)

throughout the whole simulation as expected, both for the two- and the three-dimensional cases. The slope of the line corresponds to the imaginary part of the temporal eigenvalue. The values extracted from the simulations, which can be found in tab. 2.4.1 show good agreement with the linear analysis up to the 4-*th* significant digit.

2.4.2. *Turbulent open channel flow at* $Re_\tau = 180$

In order to test the code for turbulent cases, we performed fully-resolved turbulent open-channel simulations, comparing the results to a published reference case. Handler *et al.* (1999) studied the effect of isothermal and constant heat boundary condition at the free-surface of open-channel flows at $Re_\tau = 180$, high enough for turbulence to be sustained. Initial conditions with randomly distributed noise around the Poiseuille profile led to continuously turbulent states. The box size including only one-half of the symmetric channel was chosen to $(L_x, L_y, L_z) = (4h, h, 3/2h)$. In order to fully resolve all the scales, the resolution 128 x 129 x 128 was applied. Note that the resolution is the same as used by Handler *et al.* (1999), but the grid collocation is now narrower close to the wall and coarser in the free-stream. Simulations have been run for 1500 τ and statistics were computed from $t = 500\tau$. τ represents the time unit h/U. Another simulation has also been run where the number of points in the region close to the wall was matched with the reference case, *i.e.* the resolution was decreased to 128 x 97 x 128. Figure 4 shows the profile of the mean streamwise velocity (*left*) and of the velocity variances (*right*). A very good agreement is obtained between the curves from Handler *et al.* (1999) and the curves from both the high resolution as well as the low resolution runs.

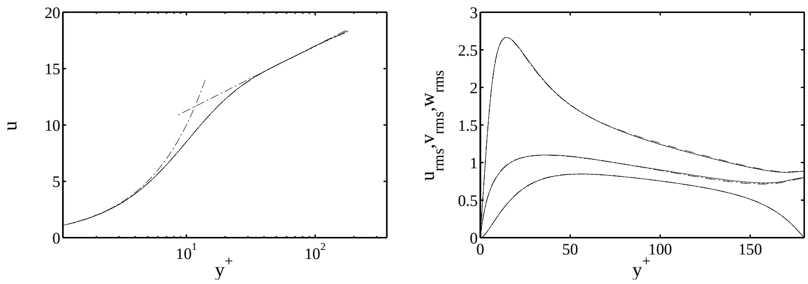

FIGURE 4. Comparison of statistical quantity with the reference case (Handler *et al.* 1999). ——— Current simulation (res. 128 x 129 x 128); ········ Handler *et al.* (1999) (res. 128 x 129 x 128); – – – decreased resolution (res. 128 x 97 x 128)

Note that if we were to use the *old* version of Simson, we would not be able to decrease the resolution. If we compare the time needed for each full 4-stage iteration (the code was run on 32 processors), the following values are obtained: 1.1 seconds for the old version; 0.7 seconds and 0.5 seconds for the symmetric versions with 129 and 97 grid points in y, respectively. Therefore, a gain on the order of 50% has been achieved for the time needed for each full step. In addition, whenever the CFL condition is restricted by the resolution in y, a further gain might be obtained. In fact, at the upper boundary velocities do not vanish as they do at the lower wall and - for full Gauss-Lobatto grids - the CFL condition is indeed more severe at the upper boundary. Therefore, avoiding the clustering of points at the shear-free surface can significantly improve the stability condition and allow for a larger time step.

3. Stratified flows

Open channel flow simulations with stable stratification have recently been used in order to understand atmospheric turbulence close to the Earth's surface (Nieuwstadt 2005). In the following, we will describe two main modifications introduced into the code in order to handle stratification: a new CFL restriction of the time step which accounts also for the effect of stratification and the implementation of a fringe region at the top of the domain which is intended to prevent spurious reflections of internal gravity waves at the upper boundary.

3.1. *New CFL condition*

The CFL condition currently implemented in SIMSON is not accounting for the effect of buoyancy forces when active scalars are considered. This effect can be rather important, especially for unstable stratifications when density gradients actually drive the flow and produce turbulent kinetic energy. Following the procedure outlined by Chevalier *et al.* (2007), the Boussinesq equations can be linearized around a baseflow as

$$\frac{\partial u_i}{\partial t} + u_{0j}\frac{\partial u_i}{\partial x_j} = -\frac{\partial p}{\partial x_i} + \frac{1}{Re}\frac{\partial^2 u_i}{\partial x_j \partial x_j} + Ri\theta\delta_{i2}, \tag{56}$$

$$\frac{\partial \theta}{\partial t} + u_{0j}\frac{\partial \theta}{\partial x_j} + u_2\frac{d\theta_0}{dx_2} = \frac{1}{Pe}\frac{\partial^2 \theta}{\partial x_j \partial x_j}, \tag{57}$$

where the subscript 0 stands for the mean flow quantities. Henceforth, for simplicity, we will restrict ourself to the two-dimensional case, where no spanwise variation is assumed. After same rearrangements, as in (2.1), the linear system can be rewritten in the matrix form as

$$\frac{\partial \tilde{u}}{\partial t} = L\tilde{u} + G\tilde{u}, \tag{58}$$

where

$$L = \begin{bmatrix} \frac{\nabla^2}{Re} & 0 \\ 0 & \frac{\nabla^2}{Pe} \end{bmatrix} \qquad G = \begin{bmatrix} -u_{0j}\frac{\partial}{\partial x_j} & Ri\nabla_H^2 \\ \frac{d\theta_0}{dy}\nabla^{-2} & -u_{0j}\frac{\partial}{\partial x_j} \end{bmatrix} \tag{59}$$

and

$$\tilde{u} = \begin{Bmatrix} \nabla^2 v \\ \theta \end{Bmatrix}. \tag{60}$$

Note that in eq. (58), the right hand side has been split in two contribution corresponding to the different time discretization which have been used: implicit Crank-Nicolson for the linear part (L) and explicit forth-order Runge-Kutta for the non-linear one (G). Assuming that Fourier modes are used in all three directions, the matrices L and G in (59) can be written as

$$\hat{L} = \begin{bmatrix} -\frac{\alpha^2+\gamma^2}{Re} & 0 \\ 0 & -\frac{\alpha^2+\gamma^2}{Pe} \end{bmatrix} \quad \text{and} \quad \hat{G} = \begin{bmatrix} -i(u_0\alpha + v_0\gamma) & -Ri\alpha^2 \\ -\frac{1}{\alpha^2+\gamma^2}\frac{d\theta_0}{dy} & -i(u_0\alpha + v_0\gamma) \end{bmatrix}, \tag{61}$$

where α and γ stand for the horizontal and vertical wavenumber respectively. Assuming that $Pr = 1$ (and therefore $Re = Pe$), the linear system (59) can be easily diagonalized and its eigenvalues are

$$\lambda_{1,2} = i\left(u_0\alpha + v_0\gamma \pm \sqrt{Ri\frac{\alpha^2}{\alpha^2+\gamma^2}\frac{d\theta_0}{dy}}\right). \tag{62}$$

Comparing this expression with the one found by Chevalier *et al.* (2007), we note that an additional term is present, namely

$$\sqrt{Ri\frac{\alpha^2}{\alpha^2+\gamma^2}\frac{d\theta_0}{dy}}, \tag{63}$$

which accounts for the contributions of an active scalar. Note that the factor which depends on the spatial wavenumber

$$\frac{\alpha^2}{\alpha^2+\gamma^2}=\frac{1}{1+\frac{\gamma^2}{\alpha^2}}$$

is always positive and smaller or equal to 1. An upper bound for the additional term in (63) can therefore be set to

$$\sqrt{Ri\frac{d\theta_0}{dy}}. \tag{64}$$

This condition is implemented in the code and leads to stable integration in buoyancy driven flows, *e.g.* Rayleigh-Bernard convection.

3.2. *Internal waves and the fringe region*

In stable stratified flows internal gravity waves can develop and travel throughout the whole domain. Such waves may interact with the underlying turbulence and may affect the energy transfer from one region to another, especially in the vertical direction. The symmetric condition at the upper boundary, which enforces the wall normal velocity to vanish there, may lead to spurious reflections of incoming internal waves.

Indeed, gravity waves are seen in nature as well. They can either be produced by turbulence, as described Taylor & Sarkar (2007), or by topography, *e.g.* mountain waves (as in Klemp & Lilly 1978). In these cases, however, energy is mainly transferred towards the upper atmosphere and just a negligible amount goes back towards the ground. Simulations that aim at reproducing geophysical wall bounded flows should therefore avoid spurious reflection at the upper boundary.

A number of studies have been devoted to non-reflective boundaries which may be required when wave propagation is involved. Israeli & Orszag (1981) give a good survey of different strategies that one can use in numerical simulations in order to prevent spurious reflections. The most elegant one is to enforce boundary conditions which let waves propagate through the boundary. However, this usually requires knowledge either of the time-history of the flow at the boundary (Bennett 1976) or some guesses on the wave phase velocity itself (Givoli & Neta 2003). For stratified flows, Klemp & Durran (1983) derived an elegant condition not relying on any knowledge of the time evolution but on the correlation between the pressure and the vertical velocity at the upper boundary. However, such a condition was derived within some approximations (*e.g.* the Brunt-Väisälä frequency N^2 being constant) which may not be satisfied in open channel simulations.

Other possible strategies which aim at reducing the effect of the wave reflection rely on damping regions placed at the top of the domain which are able to smoothly reduce upward travelling internal waves. The damping effect can either be obtained by an increased fictitious viscosity (*e.g.* Rayleigh-damping regions as in Klemp & Lilly 1978) or by forcing terms proportional to the velocity fluctuations around a mean value (*e.g.* sponge regions as in Clark 1977). Whereas the former method behaves as a filter which damps short waves, the latter method does not discriminate different wavelengths. Moreover, since the extra-forcing terms are explicitly discretized in time, Rayleigh regions pose rather severe time step restriction. For these reason, we use sponge regions. Nevertheless, it is necessary to point out that both methods, Rayleigh and sponge regions, are non-physical and caution is needed when using them.

The forcing term has therefore been chosen proportional to the velocity fluctuation

$$F_i = -f(y)\left(u - \bar{U}\right) \tag{65}$$

where $\bar{U}$ is the velocity averaged over a x-z plane. The damping strength has a finite positive value within the damping region and vanishes outside. Therefore, it must be y dependent. In order to allow for exponential convergence, infinitely differentiable C^∞ functions must be employed. The following smooth step function has been chosen:

$$f(y) = \begin{cases} 0, & y \le y_s \\ F_0/\left(1 + \exp\left(1/(x-1) + 1/x\right)\right), & y_s < y < h \end{cases} \tag{66}$$

which smoothly increase from 0, at the beginning of the sponge, to F_0 at the upper boundary.

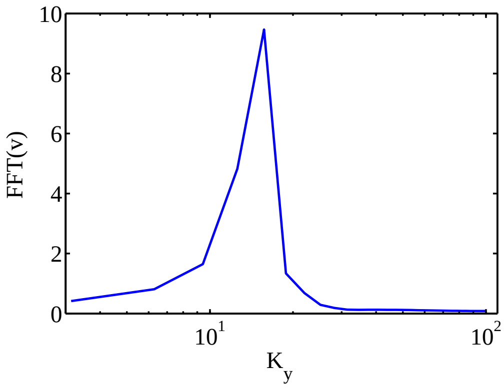

FIGURE 5. Fourier transform with respect to y of the wall-normal velocity v

In order to assess this method, a continuous small-amplitude periodic forcing is introduced close to the lower wall in a stable stratified quiescent flow. Internal gravity waves are therefore generated. $Ri = 40$ was prescribed, giving a dimensionless Brunt-Väisäla frequency of

$$N = \sqrt{Ri} \approx 6.32 \tag{67}$$

In order to obtain internal gravity waves that propagate upward, forcing frequencies lower than N have to be used. Higher values give exponential decay in the vertical direction. Thus, we generate waves with $\omega_{gw} = 5$ and with a streamwise wavenumber initially chosen to $\alpha = 3\frac{2\pi}{h}$. For a constant temperature gradient and small-amplitude waves, an analytical expression for the vertical wavenumber which involves α and ω can be found

$$\omega = N\frac{\alpha}{\sqrt{\alpha^2+\gamma^2}} = N\frac{1}{\sqrt{1+\frac{\gamma^2}{\alpha^2}}}, \tag{68}$$

giving a wall-normal wavenumber $\gamma \approx 2.32\frac{2\pi}{h} \approx 14.6h^{-1}$. Figure 5 shows the Fourier transform with respect to y of the wall-normal velocity. Since y is an inhomogeneous direction, a Blackman-Harris window was applied before calculating the Fourier Transform. As expected, a dominant wall-normal wavelength can be observed which corresponds to $k_y \approx 15.71$, matching quite closely with the one predicted by equation (68). Note that a perfect match is prevented by the fact that the height of the box is not an integer multiple of the theoretical wavelength $\lambda_y = 2\pi/k_y$.

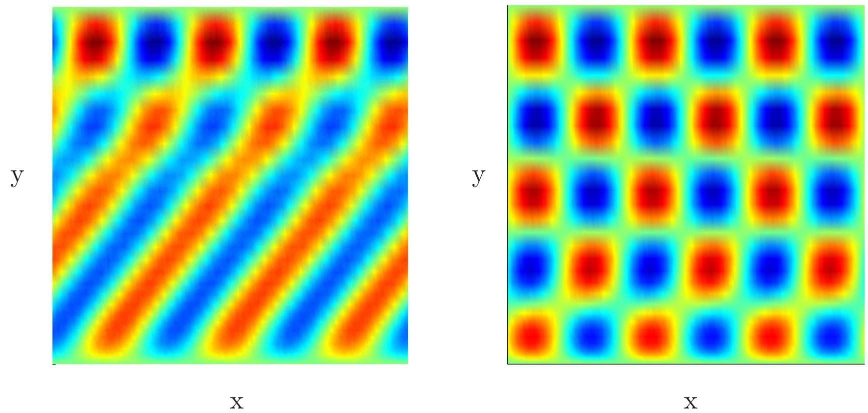

FIGURE 6. Vertical velocity v in a vertical plane $x - y$ at $t = 0.2\tau$ and $t = 18\tau$. Internal gravity waves are generated by the volume forcing applied close to the lower wall and propagate vertically.

Figure 6 shows the vertical velocity in a x-y plane for two different time units, to the left at an early stage and to the right at a sufficiently late time to allow the interaction of upward and reflected downward waves. As we can clearly see, a fairly large amount of energy is reflected back towards the ground: the oblique shape cannot be observed any longer, replaced by quasi-standing waves which arise from the interaction of upward and downward waves.

Figure 7 shows the flow fields where half of the domain along y is occupied by a sponge region, whose strength has been increased from left to right, $F_0 = 1, 10, 100$. For small values waves still reach the upper boundary and a consistent amount of energy is reflected. However, such a value is far

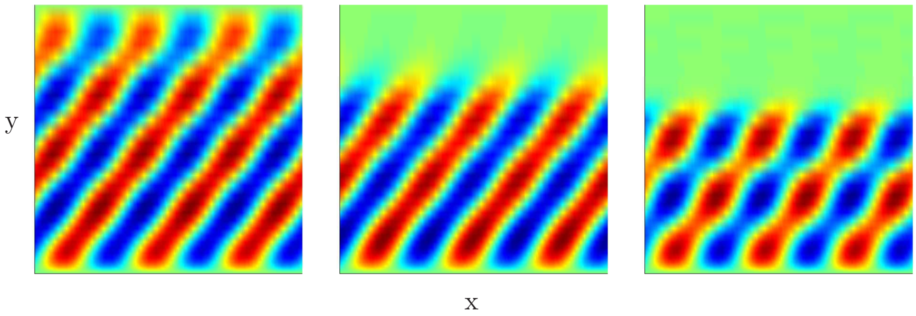

FIGURE 7. Vertical velocity v in a vertical plane $x - y$ after that a statistically steady state is achieved. Internal gravity waves are forced close to the lower wall. The strength of the fringe placed at the top of the domain increases from left to right: $F_0 = 1, 10, 100$

smaller than in the case where no damping region is present (figure 6), and oblique waves propagating along the wall-normal direction can now be recognized. As F_0 increases, the waves become more strongly damped and a very limited amount of energy is able to reach the upper boundary and reflect back. However, if F_0 is too large, a reflection starts to occur close to the fringe boundary itself. There is therefore an optimal value for which the damping is high enough to prevent the waves to reach the upper boundary, but, on the other hand, not strong enough to generate reflection at the fringe boundary.

The optimal strength is a function of the internal gravity wave wavenumber. In the simulations described above just one particular wavenumber in the streamwise direction, namely $\alpha = 6\pi$, was considered. In order to study how the performance of the sponge region changes with the streamwise wavenumber, a parametric study has been carried out. Instead of continuously introducing internal gravity waves, the periodic forcing is applied only for very short time, leading to the development of a wave packet which propagates upward. In this way, we can easily find the amount of energy reflected back towards the ground as:

$$E_{reflected} = \min_{y=y_s} \langle p'v' \rangle \tag{69}$$

where y_s is the location where the sponge region starts. In the ideal case, this quantity should be equal to zero.

Figure 8 shows the ratio between the reflected energy for various damping strength and for $\alpha = (1, 2, 3, 4) \cdot 2\pi$. A clear trend can be seen in figure 8: the higher the wavenumber, the smaller the optimal strength. In fact, due to the effect of the viscosity, high wavenumber waves are naturally damped and cannot reach the upper wall. Strong sponge regions move the reflection point towards the lower wall and lead to higher downward energy flux at $y = y_s$. As the wavelength increases, viscosity cannot efficiently damp the waves and due

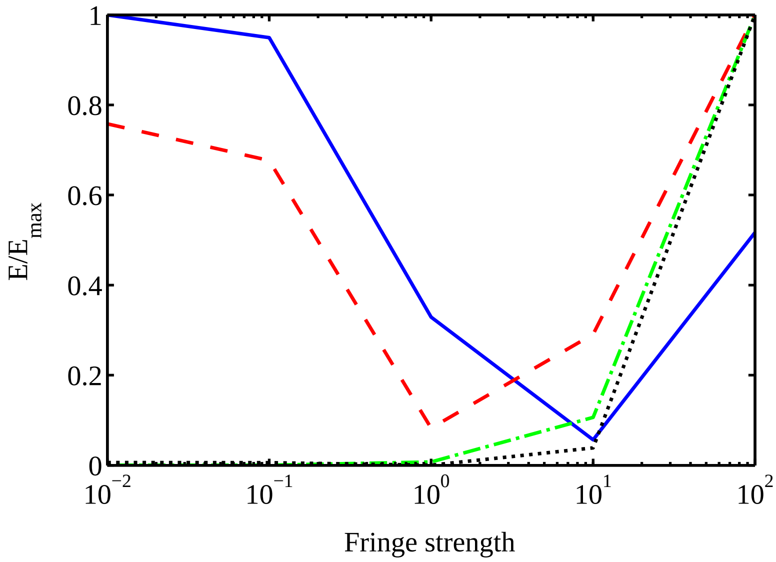

FIGURE 8. Reflected energy function of the fringe strength for different value of the streamwise wavenumber. For each wavenumber the curve are normalized with the maximum for that particular α. ——— $\alpha = 2\pi$; - - - $\alpha = 4\pi$; −·− $\alpha = 6\pi$; ········ $\alpha = 8\pi$.

to the symmetric condition, a considerable amount of energy is reflected back. Fairly strong sponge regions are therefore required.

Even though sponge regions can effectively reduce the amount of reflected energy, they cannot completely nullify it. The minimum downward energy flux at the fringe boundary can be reduce by increasing the height of the damping region, but, since there are no free lunches, at the price of an increased computational cost.

Acknowledgments

Computer time provided by SNIC (Swedish National Infrastructure for Computing) is gratefully acknowledged.

References

Bennett, A. F. 1976 Open boundary conditions for dispersive waves. *J. Atmos. Sci.* **33**, 176–182.

Canuto, C., Hussaini, M. Y., Quarteroni, A. & Zang, T. A. 1988 *Spectral methods in Fluid Dynamics*. Springer-Verlag.

Chevalier, M., Schlatter, P., Lundbladh, A. & Henningson, D. S. 2007 simson - A Pseudo-Spectral Solver for Incompressible Boundary Layer Flows. *Tech. Rep.* KTH Mechanics, Stockholm, Sweden, TRITA-MEK 2007:07.

Clark, T. L. 1977 A small-scale dynamic model using a terrain-following coordinate transformation. *Journal of Computational Physics* **24** (2), 186 – 215.

Corral, R. & Jiménez, J. 1995 Fourier/chebyshev methods for the incompressible navier-stokes equations in infinite domains. *Journal of Computational Physics* **121** (2), 261 – 270.

Givoli, D. & Neta, B. 2003 High-order non-reflecting boundary scheme for time-dependent waves. *Journal of Computational Physics* **186** (1), 24 – 46.

Handler, R. A., Saylor, J. R., Leighton, R. I. & Rovelstad, A. L. 1999 Transport of a passive scalar at a shear-free boundary in fully developed turbulent open channel flow. *Physics of Fluids* **11(9)**, 2607–2625.

Israeli, M. & Orszag, S. A. 1981 Approximation of radiation boundary conditions. *Journal of Computational Physics* **41** (1), 115 – 135.

Klemp, J. B. & Durran, D. R. 1983 An Upper Boundary Condition Permitting Internal Gravity Wave Radiation in Numerical Mesoscale Models. *Monthly Weather Review* **111**, 430.

Klemp, J. B. & Lilly, D. K. 1978 Numerical Simulation of Hydrostatic Mountain Waves. *Journal of Atmospheric Sciences* **35**, 78–107.

Laurien, E. & Kleiser, L. 1989 Numerical simulation of boundary-layer transition and transition control. *Journal of Fluid Mechanics* **199**, 403–440.

Li, Q. 2009 Simulations of turbulent boundary layers with heat transfer. PhD thesis, KTH, Department of Mechanics.

Nieuwstadt, F. T. M. 2005 Direct numerical simulation of stable channel flow at large stability. *Boundary-Layer Meteorology* **116**, 277–299.

Taylor, J. R. & Sarkar, S. 2007 Internal gravity waves generated by a turbulent bottom Ekman layer. *Journal of Fluid Mechanics* **590**, 331–354.